Impact of Blade Sweep on Aerodynamic and Aeroacoustic Performance Optimization of Isolated Propellers

Master Thesis

W. de Haan

Technische Universiteit Delft

TU Delft

Cover image source: M. Schwarzenberger, 2015, https://pixabay.com/nl/users/blickpixel-52945/

Impact of Blade Sweep on Aerodynamic and Aeroacoustic Performance Optimization of Isolated Propellers

by

W. de Haan

to obtain the degree of Master of Science
at the Delft University of Technology,
to be defended publicly on Wednesday August 25, 2021 at 14:00.

Student number:	4296982	
Thesis committee:	Dr. ir. T. Sinnige,	TU Delft, daily supervisor
	Prof. dr. ing. G. Eitelberg,	TU Delft, chair and supervisor
	Dr. Ir. D. Ragni,	TU Delft

An electronic version of this thesis is available at `http://repository.tudelft.nl/`.

TU Delft

Preface

This master thesis report is written to meet the graduation requirements of my Master of Science degree in Flight Performance & Propulsion, with a specialisation in Flight Performance, at the faculty of Aerospace Engineering at the Delft University of Technology. A year of hard work resulted in this document, which also marks the end of my time as an Aerospace Engineering student in Delft. I am looking back with great joy at the numerous memories of adventures, challenges and experiences I had as a student. Being at the end of this adventure, I would like to express my gratitude towards a number of people for the continuous support and guidance throughout this project and my time as a student in general.

I would like to thank my supervisors Tomas Sinnige and Georg Eitelberg for their guidance throughout the entire project. Although the majority of the progress meetings we did were virtual, I feel your passion and in-depth knowledge inspired me to successfully complete this thesis. I feel privileged to have been supervised by you both. A special thanks also to Jatinder Goyal, who helped me in the verification process of my noise model implementation. I really appreciated your time.

Also, I would like to thank my friends and former roommates. For my roommates, during the lockdowns, you were like fellow students during the day and good friends in the evening. Last but not least, I also would like to thank my parents Adrie, Evert and my girlfriend Rosalie for the endless love and support throughout this project and my studies in general. You cheered me up when I felt down and you celebrated with me when I had success.

W. de Haan
Delft, August 2021

Summary

In the last decades, the increment of oil prices and the growth of environmental awareness raised the desire for more fuel efficient aircraft engines. As a consequence, there is renewed interest in the field of propeller propulsion systems. Due to the higher potential propulsive efficiency of a propeller compared to a turbofan, propellers can provide a significant reduction in energy consumption for future aircraft, including hybrid-electric and all-electric aircraft. However, since there is no casing around a propeller, noise emissions for propeller engines are significantly higher compared to the emissions for turbofans. As noise emissions around airports have a significant negative impact on residents living near those airports, a requisite for realizing the potential of propellers is to reduce noise emissions by propeller blade design and propeller operation. Research focused on blade design showed that application of blade sweep can lead to significant noise reduction while only mildly affecting the aerodynamic performance.

This thesis aims to quantify the impact of blade sweep on the trade-off for aerodynamic and aeroacoustic performance characteristics of an isolated propeller by means of an optimization study. Therefore, only aeroacoustic and aerodynamic performance are considered in this study and structural and aeroelastic modelling is not performed. In order to meet the research objective, both an aerodynamic and aeroacoustic analysis model are used to obtain the key performance indicators for propeller efficiency and noise, respectively.

The aerodynamic analysis model used to calculate thrust coefficient, power coefficient and propeller efficiency is a classic BEM-model implementation with a capability of modelling blade sweep. The effect of this blade sweep on aerodynamic performance in the model is included by a correction of lift and drag coefficients. Since the Blade Element Momentum(BEM)-model is a low-order numerical model, a computationally cheap analysis is realized. Validation of this model indicated that evaluating propellers with highly swept blades and high blade solidity resulted in inaccurate findings, indicating that these propeller blade types should be avoided in this analysis. However, for propellers with a low sweep and low blade solidity the BEM-model showed accurate results. Verification of this model was performed using a second BEM-model with a different approach of modelling blade sweep. This verification showed that the implementation used in this thesis is more accurate when operating at low thrust coefficients. The aeroacoustic analysis model used for the calculation of propeller noise emissions is the frequency-domain method by Hanson. This model was verified by comparing it to another independent model implementation with equal inputs. Validation of this model was not performed, since it has extensively been validated by others.

To keep the process computationally cheap, the size of the design vector was deliberately limited by representing the blade sweep distribution with a Bézier-curve defined by four control points. Using this relatively small design vector, the propeller blade geometry could still be represented with a high level of accuracy. The optimization study was performed using a 6-bladed propeller with a diameter of 0.4m (XPROP) as a baseline propeller. For this baseline propeller, the operational variables - advance ratio and pitch - were changed to obtain an optimum aerodynamic or aeroacoustic performance. Additionally, the blade sweep angle was added to the design vector, which allowed for assessment of blade sweep on noise reduction. Throughout the optimization study, an equal thrust coefficient T_C of 0.15 was maintained. In this thesis, the thrust coefficient is defined with respect to the dynamic pressure of the freestream velocity experienced by the aircraft. For multi-objective optimization, a weighting factor was used to include multiple objectives into the objective function. An alternative approach was to use a minimum value for propeller efficiency and optimize the design variables. Both methods were applied. Furthermore, the optimization algorithm was a gradient based method, which allows for fast convergence.

Optimization results were generated for a thrust coefficient $T_C = T/\rho_\infty V_\infty^2 D_p^2$ of 0.15, a freestream velocity of 60 m/s and a corresponding freestream Mach number of 0.17. For a design vector containing advance ratio and pitch, the difference in results between optimizing for pure aerodynamic and pure aeroacoustic performance were 11dB in propeller noise and 5% in propeller efficiency. High aeroacoustic performance was obtained by operating at high pitch and high advance ratio, since the resulting low Mach numbers at the blade sections led to reduced noise emissions. On the contrary, high aerodynamic performance was obtained by operating at lower advance ratio and pitch, to obtain an optimum overall thrust-to-torque ratio. An error-type function fit through the optimization results enabled additional quantification of results. The gradient of the fit showed that a larger penalty in terms of propeller efficiency led to larger noise reductions, whereas the sensitivity of noise

reduction decreased as the maximum allowed propeller efficiency penalty increased. For the design point for minimum noise, a gradient of 0.31dB for each percent efficiency was found, whereas at the point for maximum propeller efficiency, this gradient was found to be 9.4dB for each percent efficiency.

The impact of blade sweep application on aeroacoustic and aerodynamic performance yielded a 0.5dB noise reduction for the generated swept-bladed design with respect to the straight-bladed design considering pure aeroacoustic optimization. The shape of the blade featured a gradual increase of forward sweep from root to tip and a large backward sweep near the tip. Analysis showed that the main noise reduction mechanism was the shift of blade loading to smaller radii due to the application of blade sweep, since loading noise is dominant at low flight Mach numbers. Due to the small noise reduction, the sensitivity of the phase cancellation effect due to blade sweep on noise reduction was assessed. It was presumed that the phase lag caused by blade sweep is proportional to the MCA-to-λ ratio. To assess if the increase of the MCA-to-λ ratio led to a noise reduction by phase cancellation, this ratio was increased by application of a larger blade sweep MCA. To solely assess the effect of phase cancellation on noise reduction, only the effect on thickness noise was assessed. An increment of the application of blade sweep led to a reduction in thickness noise, which proved that noise reduction was indeed caused by an increase of the MCA-to-λ ratio. For the initial climb phase, the effect of blade sweep application to reduce noise remained small due to the low freestream Mach number. However, within the optimization space, other variables such as the blade number, chord and twist were ignored, which could be used in future studies to enhance the effect of blade sweep application in order to further reduce thrust specific noise.

The results presented in this thesis emphasize the sensitivity of aerodynamic and aeroacoustic performance of propellers to the application of blade sweep. It was shown that the achievable noise reduction is proportional to the applied blade sweep in relation to the wavelength of sound, which can be increased either through increasing the freestream Mach number, increasing the blade count or increasing blade sweep application. In addition, this thesis showed that a significant noise reduction in the initial climb phase can be achieved by optimizing the operational variables for high aeroacoustic performance compared to high aerodynamic performance. The knowledge gained from this thesis can be used to benefit the design of future low noise propellers.

Contents

Nomenclature

Variables

α	angle of attack, rad
$\bar{x}$	design vector
β	blade pitch angle, rad
β	blade twist angle, rad
ΔV	velocity change, m/s
$\dot{m}$	mass flow, kg/s
η	JC_T/C_P, propeller efficiency
η_p	$2/(2 + \Delta \text{ V } / \ V_\infty)$, propulsive efficiency
η_{min}	minimum allowed propeller efficiency
γ	Induced angle due to lift, rad
γ	climb angle, rad
γ	heat capacity ratio
Λ	blade sweep angle, rad
λ	wavelength of sound, m
μ	dynamic viscosity, kg/(ms)
Ω	propeller rotational speed, rad/s
ϕ_o	phase delay contribution due to lean
ϕ_s	phase delay contribution due to sweep
Ψ	lean angle, rad
Ψ_D	Fourier source transform of loading noise due to drag
Ψ_L	Fourier source transform of loading noise due to lift
Ψ_V	Fourier source transform of thickness noise
ρ_0	ambient density, kg/m^3
σ	blade solidity
θ	retarded radiation angle from propeller to observer point, rad
θ_1	visual radiation angle from propeller to observer point, rad
φ	inflow angle, rad
φ'	induced angle due to induction, rad
φ_0	inflow angle without induction, rad
A	area of actuator disk, m^2
a	speed of sound, m/s
a_a	axial induction factor
a_t	tangential induction factor
a_t	tangential induction factor
B_D	chord-to-diameter ratio
BPF	nN_b, blade-passage frequency, Hz
c	chord length, m
c_0	ambient speed of sound, m/s
C_D	sectional drag coefficient
C_L	sectional lift coefficient
C_P	$P/\rho_\infty n^3 D_p^5$, propeller power coefficient (defined wrt tip speed)
C_p	Pressure coefficient
C_Q	$Q/\rho_\infty n^2 D_p^5$, propeller torque coefficient (defined wrt tip speed)
C_T	$T/\rho_\infty n^2 D_p^4$, propeller thrust coefficient (defined wrt tip speed)
CP	control point
D	drag, N
D_p	propeller diameter, m

dr	segment length on a blade, m
F	torque, Nm
f	prandtl correction factor
$f_D(X)$	drag shape function
$f_L(X)$	lift shape function
f_{hub}	prandtl hub correction factor
f_{tip}	prandtl tip correction factor
FA	Face Alignment, m
h	height, m
$H(X)$	thickness shape function
J	advance ratio
J_{mB}	bessel's function of order mB
k	optimization weighting variable
k_x	dimensionless chord-wise wave number
k_y	dimensionless chord-wise wave number
L	lift, N
M	Mach number
m	harmonic of blade passing frequency
M_r	sectional relative Mach number
M_t	tip rotational Mach number
M_x	free stream Mach number
MCA	mid-chord alignment, m
n	mB, harmonic of shaft frequency
n	degree of Bézier curve
n	propeller rotational speed, Hz
N_b,B	propeller blade count
N_{crit}	critical amplification factor
p	acoustic pressure, Pa
p_∞	ambient pressure, Pa
P_{Dm}	loading components of complex Fourier coefficient of acoustic pressure at m^{th} harmonic
P_{Lm}	loading components of complex Fourier coefficient of acoustic pressure at m^{th} harmonic
P_{mB}	complex Fourier coefficient of acoustic pressure at m^{th} harmonic
p_{ref}	reference acoustic pressure, Pa
p_{rms}	acoustic pressure in root-mean-squared form, Pa
P_{Vm}	volume components of complex Fourier coefficient of acoustic pressure at m^{th} harmonic
R	Propeller radius, m
R	gas constant, J/(kg K)
r	radial coordinate, m
Re	Reynolds number
SPL	sound-pressure level, dB
T	temperature of air, K
T	thrust, N
t	observer time, s
t	time, s
t_b	maximum thickness-to-chord ratio
T_C	$T/\rho_\infty V_\infty^2 D_p^2$, propeller thrust coefficient (defined wrt freestream velocity)
$TSSP$	thrust specific sound-pressure, dB
$TSSP_{mean}$	average of thrust specific sound pressure, dB
V	velocity, m/s
V_0	axial velocity, m/s
V_∞	freestream velocity, m/s
v_a	induced axial velocity, m/s
V_s	velocity along swept blade section, m/s
V_t	tangential velocity, m/s
v_t	induced tangential velocity, m/s
v_{climb}	climb velocity, m/s

V_{eff}	effective velocity, m/s
W	weight, N
x	design variable
x_{CP_i}	y-coordinate of the ith control point
y	observer distance from propeller axis
y_{CP_i}	y-coordinate of the ith control point
z	normalised radial location

Sub- and superscripts

∞	freestream
0	initial optimization point
0.7R	radial station at 70% of the blade
amb	ambient
b	blade
des	design
eff	effective velocity in the rotational frame
loading	contribution due to loading
max	maximum
min	minimum
opt	optimum
rms	root mean squared
t	tip
thickness	contribution due to thickness
x	in axial direction

Abbreviations

APIAN	Advanced Propulsion Integration Aerodynamics and Noise
BEMT	Blade Element and Momentum Theory
CFD	Computational Fluid Dynamics
HST	Helicoidal Surface Theory
KKT	Karush–Kuhn–Tucker
NURBS	Non-Uniform Rational B-Splines
OASPL	Overall Sound Pressure Level
RANS	Reynolds-Averaged Navier-Stokes
SQP	sequential quadratic programming

List of Figures

List of Tables

I

Background

1 Introduction

1.1. Propeller Research Motivation

The first successful powered flight by a heavier-than-air aircraft from the the Wright brothers in 1903 was powered by a propeller. In the four decades that followed, propellers were the main propulsive device to power aircraft. At the end of the Second World War, the turbojet and subsequently the turbofan made their entrance. Since jet-engines can cover a larger speed-range, this has been the choice of aircraft propulsion type for most passenger aircrafts to date. However, in the last few decades, the increment of oil prices and the growth of environmental awareness have raised the desire for engines that are more fuel efficient. As a result, there is a renewed interest in the field of propeller propulsion systems, due to their high potential propulsive efficiency. The reason for this higher propulsive efficiency can be displayed with two simple equations:

$$T = \dot{m}\Delta V \tag{1.1}$$

$$\eta_p = \frac{2}{2 + \Delta V / V_\infty} \tag{1.2}$$

Equation 1.1 approximates that a thrust force T is solely the result of a change in momentum, therefore ignoring the pressure difference contribution. Equation 1.2 states that a resulting propulsive efficiency η_p is highest when there is little velocity increment of accelerated flow. Thus, a high propulsive efficiency exists when thrust is produced by means of a high mass flow instead of a high velocity increment. In general, a large propeller leads to a large mass flow, subsequently leading to a high propulsive efficiency. This principle is illustrated in figure 1.1, where it becomes clear that the propulsive efficiency of a turboprop is higher compared to the propulsive efficiency of a turbofan, due to the potential higher mass flow rate. As a result of their higher potential propulsive efficiency, there has been a renewed rise in the use of turboprops in aviation[1].

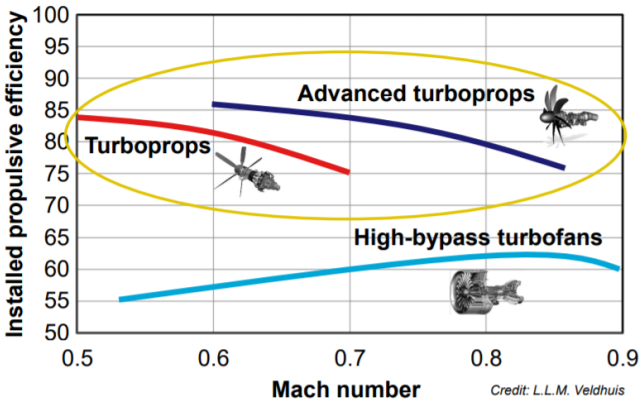

Figure 1.1: Approximate propulsive efficiency for different forms of aircraft propulsion in installed conditions[2]

Besides its propulsive efficiency characteristics, a propeller has the advantageous characteristic that it is a propulsive device which can easily be scaled to be coupled to multiple electric motors on an aircraft. Therefore, the propeller is capable of powering any all-electric and hybrid-electric aircraft, such as a small passenger aircraft, a drone or an unmanned aerial vehicle (UAV). There are numerous examples of novel electric aircraft concepts available, ranging from distributed propulsion to a single propeller configuration. An example all-electric single propeller aircraft is the Pipistrel Velis Electro, which is the first EASA-type certified electric aircraft[3] (figure 1.2).

Figure 1.2: Pipistrel Velis Electro, the first EASA-type certified electric aircraft[3]

For a turbofan engine, the casing and nacelle reduce the axial Mach number at the rotor allowing a high flight velocity. Additionally, noise emissions generated by the whole propulsor are partially contained by the casing. As propellers are not surrounded by a casing, propellers are exposed to the freestream velocity which can ultimately lead to a limitation in the flight velocity and extensive noise emissions. The limitation of flight speed is caused by high Mach numbers at the propeller blade tip, which leads to a large amount of drag at high Mach numbers. Additionally, high tip Mach numbers can also lead to extensive noise generation by the propeller. The absence of the casing leads to a direct emission of noise to the observer. Studies have been performed to assess the effect of aircraft noise on passenger comfort and on the health of those living near airports[4, 5]. Sleep disturbance and psychological effects are examples of the effects experienced by a large group of people.

Due to fuel-saving possibilities of propeller use in aircraft propulsion, research is conducted to mitigate both the limitation of cruise speed and the extensive noise emissions. Both these limitations can be mitigated to a certain extent by carefully designing the propeller blades. The focus of this thesis will be on reducing propeller noise emissions, while also maximizing propeller aerodynamic performance. Reducing noise emissions of a propeller could lead to more widespread use of the propeller, which ultimately has the potential to reduce the environmental impact. A reduction of noise emissions can be achieved by using advanced blade design methods. Typically, a certain amount of variable blade sweep is incorporated in advanced propeller blade designs, which is both beneficial for reducing noise emissions and for increasing the speed limit of propeller aircraft. An example of a propeller with swept blades is the propeller used by the Airbus A400m, shown in figure 1.3.

The propeller geometry is highly dependent on the design goal to be achieved. The application of sweep to the blade is less favorable if a low speed propeller is purely designed for high propulsor efficiency for example. If, however, the propeller is designed for multiple objectives, certain compromises have to be made in the design thus making the design process an optimization study. In this thesis, the focus is on optimum propeller geometries for a maximum propulsor efficiency and minimum noise emissions for an isolated propeller. This means the propeller plane is not subjected to nonuniform inflow caused by an upstream wing or the fuselage for example. The choice of the aerodynamic and aeroacoustic numerical model influences the proximity of the obtained optimum to the real optimum. Therefore, both aerodynamic and aeroacoustic performance models are a topic of extensive research, as well as research in propeller optimization between aerodynamic and aeroacoustic performance.

Figure 1.3: Airbus A400m propellers shown at the 2009 Paris airshow [6]

Previous optimization studies have been performed with varying objectives, constraints and different aerodynamic/aeroacoustic models. For each of these optimization studies, an isolated propeller was assumed. In these studies, the resulting blade geometries have been different in shape, caused by these differences in approach thus underlining the importance of accurate numerical models and a well-defined optimization framework. Marinus et al.[7] presented a method in which multiple objective functions were chosen and the aerodynamic performance was calculated using a Reynolds-Averaged Navier-Stokes (RANS) to create a surrogate model. On the contrary, Gur et al. [8] relied solely on the BEM-model as their aerodynamic model, while Pagano et al.[9] used the BEM-model in conjunction with a more advanced CFD-model. These examples of optimization studies illustrate the numerous approaches in both numerical model and optimization setup which can be taken to obtain an optimum propeller geometry. However, all of these studies resulted in propeller designs which showed that the use of a blade sweep angle is beneficial in reduction of noise emissions. A depiction of a blade generated by Pagano et al. is shown in figure 1.4 [9].

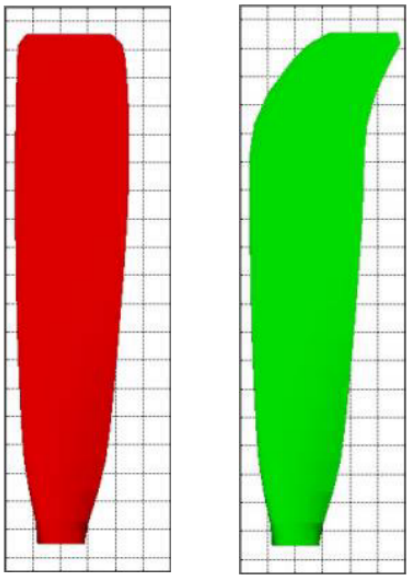

Figure 1.4: Comparison of a baseline (left) and an optimum blade (right) design by Pagano et al.[9]

Throughout this optimization study, a search for optimum propeller designs for maximum aeroacoustic and aerodynamic performance is conducted. As discussed, the choice of aerodynamic and aeroacoustic model is of great importance. Higher-fidelity models catch the attention due to their accuracy of computing results. However, often the use of higher-fidelity models in propeller optimization often results in excessive computational times. Therefore, surrogate models are introduced, which are built upon the results of CFD-simulations.

However, the performance of these surrogate models is not always satisfactory, as encountered by Marinus[7]. Therefore, in this study, low order numerical models are used to generate results. Using low-order methods requires a thorough verification procedure to build confidence in these models, especially in the method of modelling blade sweep. By a comparison to existing CFD- and experimental results an assessment can be made if these low-order numerical tools are suitable for the use in propeller optimization studies. If low-order numerical tools can be accurately used in optimization studies, this may lead to new knowledge of improving propeller blade design for both aeroacoustic and aerodynamic objectives. Subsequently, the improvements in design can make the propeller more attractive as a choice for a propulsion device, either for an all-electric aircraft, a drone or a turboprop.

1.2. Thesis Aim and Objectives

As discussed, the application of blade sweep seems to be a promising design step to reduce propeller noise emissions. However, there is little knowledge of the impact of blade sweep on the trade-off between aeroacoustic and aerodynamic performance of a propeller. Therefore, the main objective of this thesis is formulated as follows:

> "To quantify the impact of blade sweep on the trade-off for aerodynamic and aeroacoustic performance of an isolated propeller by means of an optimization study."

In order to reach this objective, the following research questions are defined:

1. Which fast and accurate aerodynamic and aeroacoustic performance models for an isolated propeller derived from literature are suitable to be applied in an optimization framework?
2. Which suitable optimization method should be selected such that an adequate optimization is performed?
3. How to quantify the trade-off between aerodynamic and aeroacoustic performance for an isolated propeller only considering pitch and advance ratio as design variables?
4. What is the influence of blade sweep, pitch angle and advance ratio on aerodynamic and aeroacoustic characteristics of a propeller in isolated conditions?

A vital part in answering these research questions and reaching the research objective is the choice of numerical model and the method of modelling blade sweep. These models are subjected to a validation & verification process in order to build confidence in the generated results. Besides, a suitable optimization framework should be defined which allows for an assessment of the effect of blade sweep. Additionally, it should be noted that this study is only focused on the aerodynamic and aeroacoustic performance of a propeller. This means aeroelasticity or structural constraints are not included in this study. Therefore, the optimization setup is defined such that infeasible blade designs are avoided.

1.3. Thesis Outline

The body of this thesis is divided into four different parts, as visualized in figure 1.5. Part I contains background information about propeller performance and propeller design. Chapter 2 includes the basic principles of propeller aerodynamic and propeller aeroacoustic performance, which is followed by a discussion of propeller design considerations in chapter 3. This part is largely based upon the performed literature study in preparation for this thesis[10].

Subsequently, part II consists of a discussion of the research tools used to generate optimization results. The foundation of this research is the method of geometry parametrisation, which is discussed in chapter 4. The aerodynamic and aeroacoustic performance models which are used to calculate key performance indicators for the optimization are discussed in chapter 5 and chapter 6, respectively. Additionally, in chapter 7 the entire optimization setup is documented.

Thereafter, in part III, the optimization results and model validation & verification are elaborated. The purpose of this part is to give an overview of the generated results and to assess these results using a proper model verification & validation. Chapter 8 gives an overview of the verification & validation steps for both the aerodynamic and aeroacoustic model, while chapter 9 gives an overview and an assessment of the optimization results. In part IV, this thesis is concluded by chapter 10, in which the conclusions and recommendations are stated.

Additionally, experimental work was performed, which eventually did not contribute to the research objective of this thesis. However, it could be used as a reference for future work. Therefore, the setup of the experimental work is included in the appendix (appendix B).

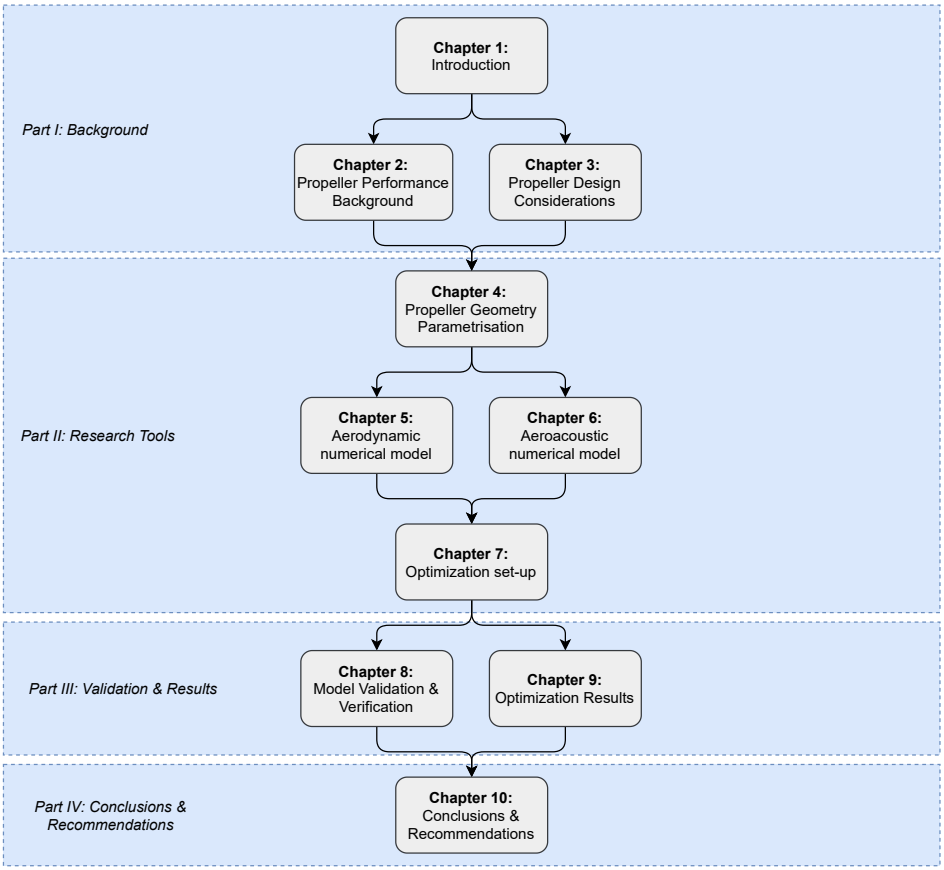

Figure 1.5: Research outline

2

Propeller Aerodynamic and Aeroacoustic Performance

This chapter provides a background on aerodynamic and aeroacoustic propeller performance for isolated propellers. The provided discussion serves as a basis for the numerical models discussed in chapter 5 and 6. Extensive research is available on both aerodynamic[11, 12] and aeroacoustic performance [13, 14] of an isolated propeller, which is concisely reviewed in this chapter. Propeller aerodynamic performance and propeller aeroacoustic performance are discussed in section 2.1 and section 2.2, respectively.

2.1. Aerodynamic Performance

The main goal of a propeller is to provide a force, which can be thrust to fly an aircraft or lift to operate a drone for example. Preferably, a propeller should be able to produce the highest amount of force using the least amount of power, that is to operate at the highest propulsor efficiency. In this section, the mechanisms for generating propulsive or lifting force and key performance indicators of propellers are discussed.

Propeller blade loading

Thrust is generated by a set of blades, which can each be considered as an individual lifting surface. In figure 2.1, a 2D blade section at radial position r of such a lifting surface is depicted (based on Geng et al.[15]. The thrust and torque of the propeller are the result of lift and drag-forces generated by lifting surfaces (blades), of which a cross section is shown in figure 2.1. The propeller blades experience a certain angle of attack α, which is the consequence of the rotation and translation of the propeller and ultimately causes the propeller to generate a force.

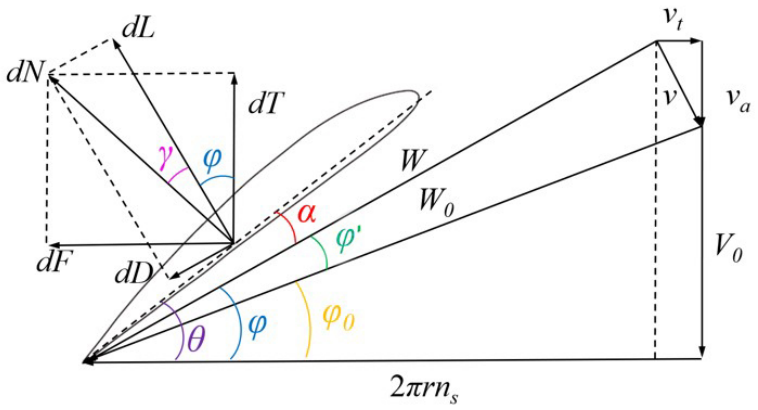

Figure 2.1: Propeller blade section at radial position r including a velocity diagram and resulting force components[15]

In figure 2.1, a velocity diagram is given and the resulting force components on the blade are displayed. The total velocity is caused by a number of velocity components: translational (V_0), rotational (V_t) and induced velocity components (v_a, v_t)[16]. The angle between the effective and the rotational velocity vector is called the inflow angle, denoted as φ. The difference between the pitch of the blade β and the inflow angle φ is called the angle of attack α. The velocity diagram in figure 2.1 results in a set of 2D force components: the lift (dL) and the drag (dD). These force components are decomposed into thrust (dT) and torque (dF).

In a 3D-representation of the blade, the loading of the entire blade along the radius is considered. Due to the rotational character of the blade, the local rotational velocity component increases with the radial coordinate. Therefore, blade velocity and blade loading tend to increase when increasing the radius. Typically, the point of maximum loading of a propeller blade is at around 70% of the radius, dependent on the operating conditions and propeller geometry. Due to propeller tip losses, the blade loading will return to zero at the tips of the blade.

Aerodynamic Performance indicators

Key aerodynamic performance indicators for a propeller are the propulsive power, the shaft power and the propeller efficiency. These performance indicators are considered as output, input and efficiency between the output and input. The blade pitch setting β together with the operating conditions of the propeller dictate the performance indicators. A propeller with a diameter D_p rotating at an angular frequency n in freestream velocity V_∞ is described by its advance ratio:

$$J = \frac{V_\infty}{nD_p} \tag{2.1}$$

For a given blade pitch setting β, the advance ratio is a scalable variable for which the propeller performance indicators can be defined: the propulsive power, the shaft power and the propeller efficiency. These key performance indicators are often expressed in a non-dimensional form, which are shown in the equations below. In these equations, the thrust and power coefficients are non-dimensionalized with respect to the dynamic pressure relative to the tip-speed of the propeller, excluding a factor π.

$$C_T = \frac{T}{\rho_\infty n^2 D_p^4} \tag{2.2}$$

$$C_Q = \frac{Q}{\rho_\infty n^2 D_p^5} \tag{2.3}$$

$$C_P = 2\pi n C_Q \tag{2.4}$$

$$\eta = J\frac{C_T}{C_P} \tag{2.5}$$

However, for optimization purposes, thrust is often non-dimensionalized with respect to the freestream dynamic pressure relative of the aircraft T_C. In this optimization study, T_C is used, since this parameter provides a comparison between different propeller designs and operating conditions for a given disk loading. The expression is depicted below.

$$T_C = \frac{T}{\rho_\infty V_\infty^2 D_p^2} \tag{2.6}$$

The propeller propulsive performance is usually defined by the key performance indicators described in equation 2.1 to 2.6 and by the radial loading distribution of the blades. When assessing the performance of a propeller, two different types of propellers are generally distinguished: fixed pitch propellers and fixed speed propellers. For a fixed pitch propeller there is a constant pitch and a controllable rotational speed. This means the key performance indicators solely depend on the rotational speed of the propeller and flight velocity.

In figure 2.2 the relation between the advance ratio and the thrust and power coefficient is depicted for a fixed pitch propeller[12]. For an increment in advance ratio, an increment of the axial/tangential velocity-ratio exists. Since the inflow angle also scales with this ratio, the inflow angle increases as well. Given a constant blade pitch, this leads to a decrease in angle of attack experienced by the blade, which results in a reduction of thrust. Thus, for an increment in advance ratio, a decrease in thrust exists, which is illustrated in figure 2.2 as well. When the advance ratio becomes too small, the thrust and power curves starts to flatten due to nonlinearity in propeller induction with the advance ratio. Furthermore, boundary layer growth and eventually flow separation occur at high angle of attack.

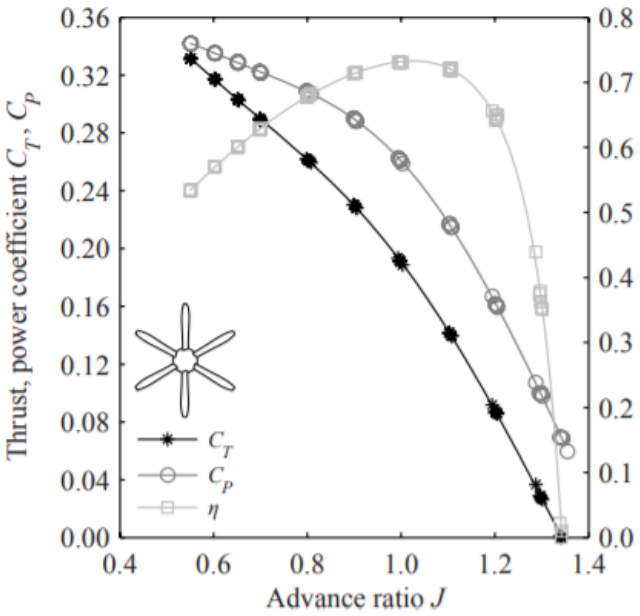

Figure 2.2: Example performance graph demonstrating the relation between advance ratio and key aerodynamic performance indicators. Results are obtained using a scaled model from a wind-tunnel, adapted from Sinnige [12]

For a fixed speed propeller, the rotational speed of the propeller is constant and the pitch can be controlled. The benefit of a fixed speed propeller is that the engine which drives the propeller can be optimized for a single operational condition. Additionally, the ability to change the pitch setting provides an opportunity to operate the propeller at maximum efficiency during the different phases of the mission. Therefore, the aerodynamic performance of the propeller is dependent on an extra variable: both the advance ratio and the pitch angle are able to be changed during the mission. Since the pitch angle and advance ratio can be changed, the thrust and power coefficients are a function of two variables and a single performance graph becomes a performance map. An example of a performance map is depicted in figure 2.3a. In this figure, the power coefficient is plotted as a function of thrust setting, advance ratio and pitch setting. Using this map, the propeller efficiency can be optimized by matching the right pitch setting to the flight conditions. In figure 2.3b, different pitch settings are shown to be optimum at different advance ratios, and thus thrust settings[17].

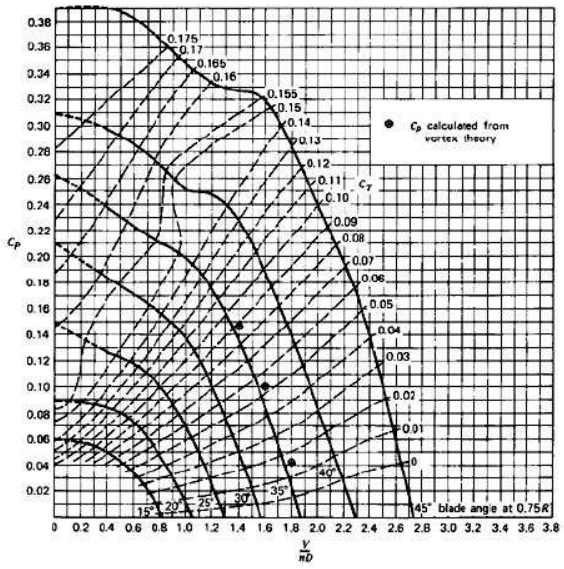

(a) Typical propeller power curves as a function of advance ratio J

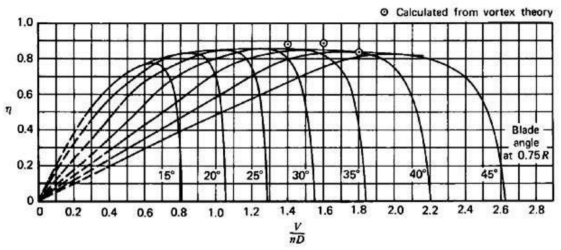

(b) Typical propeller efficiency curves as a function of the advance ratio J

Figure 2.3: Typical propeller power and efficiency curves as a function of the advance ratio[17]. Multiple curves are given for multiple pitch settings.

2.2. Aeroacoustic Performance

Next to aerodynamic performance of propellers, in this thesis the aeroacoustic performance of propellers is a main subject of research. In order to minimize the noise emissions, a proper understanding of various noise sources is required. Propeller overall noise can be subdivided into two categories: tonal noise and broadband noise. For a broad range of operating conditions, tonal noise is the dominant component of propeller noise emission[18]. Only at high frequencies, broadband noise is an important contributor to the total noise level, which occurs at high blade speeds and high blade numbers.

Each of the two noise components descend from different sources, which are discussed in this section by using extensive research of others[12, 19]. Important to note is that this section only covers noise which is emitted by the propeller itself. This means the noise by the (electric) motor which is powering the propeller is not included here.

Tonal noise sources

Tonal noise, also known as harmonic noise, is the periodic component over single frequency which remains when subtracting the broadband. In the time-domain, the tonal noise component is distinguished by a number of pulses repeated at a constant rate. In the frequency domain, a simple Dirac-delta function is present at the fundamental frequency or blade-passing frequency, which is the product of the number of blades and the rotational speed. The Dirac-delta function is also present at multiples of the fundamental frequency. An example of tonal noise both in frequency- and time-domain is illustrated in figure 2.4.

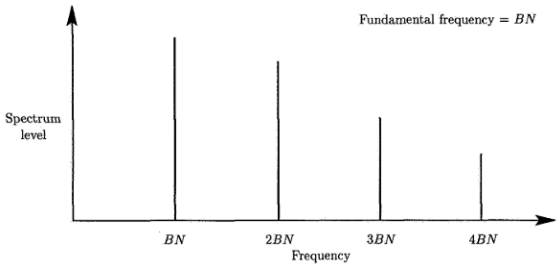

(a) Characteristic signal of propeller tonal noise in frequency-domain

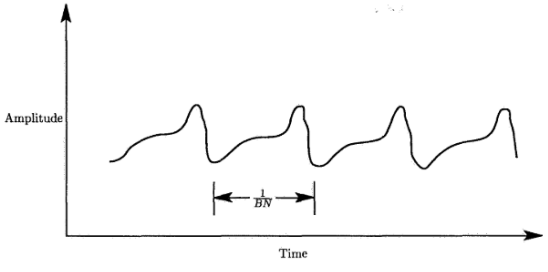

(b) Characteristic signal of propeller tonal noise in time-domain

Figure 2.4: Characteristic signals of propeller tonal noise[19]

There are four types of noise generating mechanisms for tonal noise: thickness noise, steady and unsteady loading noise and noise due to transonic effects.

- **Thickness noise** is the periodic effect of the volume of blades on displacement of the air. The amplitude of thickness noise depends on the volume of the propeller blade, and will increase for a blade with a larger volume. Thickness noise is especially relevant at high effective Mach numbers. In order to minimize the thickness noise at a given tip Mach number, thin and swept blade sections should be used.

- **Steady loading noise** sources exist due to thrust and torque generated by the propeller. These forces exist due to a pressure field surrounding the blades. These pressure disturbances move trough the medium and are propagated as noise. This is an important mechanism at low to moderate speeds.

- **Unsteady loading noise** sources exist when the blade loading is not constant in time. Unsteady loading noise occurs due to circumferential variations in inflow, e.g. due to angle of attack or airframe installation effects. This means there is a variation of blade loading around the azimuth. Both the gradient and the amplitude of the unsteady loading component are important factors, which determine if this noise source is dominant.

- **Quadrupole noise** sources exist when transonic, nonlinear effects exist, which are relevant for high Mach number, unswept propeller blades. These particular noise sources are relevant for all viscous and propagation effects, which are not covered by the thickness and loading sources.

Broadband noise sources

Broadband noise can be considered as a secondary contribution to propeller noise. According to Parry [18], the broadband noise sources are relatively unimportant at lower frequency, where the higher tonal noise sources are dominant. In general, the amplitude of the low-frequency tonal noise components of propeller noise are is higher. Therefore, the tonal noise sources are more important. At higher frequencies, the amplitude of broadband noise compares to the amplitude of tonal noise sources. For completeness, broadband noise sources are discussed, but these are not analysed in this thesis. Because of the random character of the sound-waves, the frequency domain can look continuous whereas the signal looks random in the time-domain, as displayed in figure 2.5.

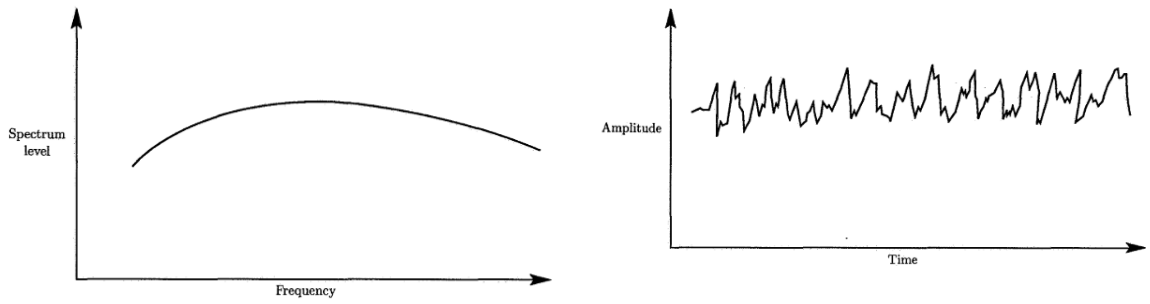

(a) Characteristic signal of propeller broadband noise in frequency-domain

(b) Characteristic signal of propeller broadband noise in time-domain

Figure 2.5: Characteristic signals of propeller broadband noise[19]

For propellers, the most important rotor-alone broadband-noise sources are:

- **Trailing edge noise:** Near the trailing edge of the blade, a turbulent boundary layer can develop. The interaction between the turbulent boundary layer and the trailing edge of the blade leads to pressure fluctuations. These pressure fluctuations are perceived by the observer as broadband noise.

- **Turbulence interaction noise:** When the free stream flow is experiencing high values of turbulence, the blades will emit a random noise. This type of noise is generated when inflow turbulence interacts with the leading edge of the blades. The corresponding broadband noise is only relevant for a propeller operating in a flow with high values of turbulence and insignificant compared to trailing edge noise.

Overall noise spectrum

The tonal noise and broadband noise together form the overall noise level perceived by the observer. In figure 2.6, noise spectra are given for different directivities of a propeller in the frequency domain: a forward directivity, near the plane of rotation and at an aft directivity. For each of the directivities, the same pattern can be observed in which the fundamental frequency and multiples of the fundamental frequency can be distinguished. In this figure, the sound pressure level is used as a performance indicator.

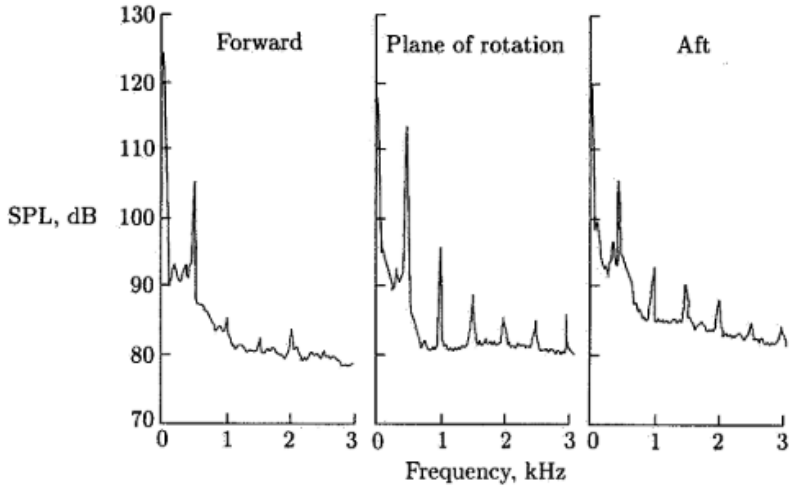

Figure 2.6: Isolated rotating propeller noise spectra, both for a forward directivity, at the plane of rotation and at an aft directivity [19]

The distinctive peaks in the spectra of the forward directivity and the plane of rotation are caused by harmonic noise sources, which produce noise at a very specific frequency. The remaining noise represented by the other frequencies in the frequency spectra, is attributed to broadband noise sources. In the noise spectra, harmonic noise sources produce sounds pressure levels which are significantly higher compared to broadband noise sources. Therefore, harmonic noise sources are usually dominant and thus this thesis focuses solely on tonal noise.

Aeroacoustic performance indicators

In order to obtain understanding of aeroacoustic performance of a propeller, a number of key performance indicators can be used. A way to express the acoustic performance of the propeller is by using the acoustic pressure at a certain position relative to the propeller p(t). The acoustic pressure is usually expressed in the root mean squared form p_{rms}:

$$p_{rms} = \sqrt{\frac{1}{T_2 - T_1} \int_{T_1}^{T_2} p(t)^2 dt} \tag{2.7}$$

This root mean squared form is generally expressed in terms of a dimensionless quantity. The T_1 and T_2 term are usually chosen in such a way that the overall time t represents one blade revolution. Often the sound pressure level (SPL) is used as a key performance indicator to represent sound pressure, which is a representation to describe the amplitude of acoustic waves. It is dimensionless since p_{rms} is divided by a reference pressure. This reference pressure p_{ref} is $20\mu Pa$, a value which is the average threshold of human hearing[19]. The sound pressure level (SPL) is defined as:

$$SPL = 20\log_{10}\left(\frac{p_{rms}}{p_{ref}}\right) \tag{2.8}$$

Although the SPL is often used to measure aeroacoustic performance of aircraft, the reference pressure is unrelated to the noise generating mechanism, making it not suitable for scaling rotor-alone noise. A more suitable approach is to compare the acoustic pressure to the thrust setting and the propeller diameter, as shown in equation 2.9. This allows for physics-based scaling between different propeller geometries, since the acoustic pressure is now related to the pressure jump over the propeller disk (T/D^2), which is a noise-generating mechanism. By including these parameters in the equation, a more legitimate comparison is guaranteed between

different propellers operating at different thrust-levels. In the work by Geng et al.[15], a detailed explanation about acoustic scaling is provided. By using this approach the thrust specific sound pressure (TSSP) is defined as[20]:

$$TSSP = 20\log_{10}\left(p_{rms} \cdot \frac{D_p^2}{T}\right) \tag{2.9}$$

Additionally to the sound pressure and adaptations of the sound pressure as a performance indicator, the blade passage frequency (BPF) is also a performance indicator. As shown in equation 2.10, the BPF is equal to the product of the propeller rotational speed and the number of blades. The frequency of sound is often normalised with the BPF. Since the tonal noise is a dominant noise source, the BPF and multiples of the BPF give the frequency at which a peak in the noise emissions occur.

$$BPF = nN_b \tag{2.10}$$

Furthermore, the tip Mach number is also an important performance indicator, since an increase in tip Mach number directly leads to an increase of the amplitude of sound waves emitted by the noise sources. The tip Mach number is defined as the tip speed of the propeller divided by the speed of sound including the vector addition of the freestream Mach number (equation 2.11) .

$$M_t^2 = \left(\frac{2\pi nr}{a}\right)^2 + M_x^2 \tag{2.11}$$

An interesting observation is the relation between the tip Mach number and advance ratio and freestream Mach number. As the advance ratio decreases for a constant freestream Mach number and diameter, the rotational speed of the propeller increases, which yields a higher tip Mach number. As shown, for an increase in freestream Mach number, the tip Mach number also increases, leading to an increment in noise emissions.

3

Propeller Design Considerations

In this chapter the general design considerations for a propeller designed for low noise emissions and high propulsor efficiency are discussed. In section 3.1 general design measures which can be taken in order to improve aerodynamic and/or aeroacoustic performance are discussed. For multiple objectives, the effect of these design measures is often assessed by an optimization study. As an introduction to different approaches in isolated propeller optimization, section 3.2 provides an overview of previously conducted optimization studies obtained from literature.

3.1. Multidisciplinary Propeller Design

Designing propellers for both high aerodynamic and aeroacoustic performance can be a challenge, since a change in design can e.g. lead to a decrease in noise emissions and also a decrease in propulsor efficiency. Therefore, in the search for an improved propeller design, the effect of a change in various design variables on aeroacoustic and aerodynamic performance needs to be assessed. The geometry parameters of a propeller are extensively discussed in chapter 4. However, since the main geometry parameters which define the design of the propeller are considered in this chapter as well, these are listed below:

- Diameter
- Blade number
- Blade thickness distribution
- Blade chord length distribution
- Blade twist distribution
- Blade sweep distribution
- Blade lean distribution
- Airfoil shape distribution
- Hub-to-tip ratio

It is desired to change a propeller design variable and improving one criterion, without negatively affecting the other criterion, therefore searching for a Pareto optimum. In order to achieve this desire, the influence of various design variables on aeroacoustic and aerodynamic performance is treated in this section.

In particular cases, it is important to note that an improvement in propeller design is not feasible due to e.g. structural, geometrical or other design constraints. Therefore, a number of the design parameters listed above are usually constrained, such as the diameter of the propeller. By increasing the diameter a signification increase in propeller efficiency can be obtained through a reduction in disk loading, which is limited by the tip Mach number, as discussed in the introduction of this thesis. However, due to ground clearance- and aircraft sizing constraints the diameter of the propeller is often specified in advance.

Design considerations for propulsor efficiency

Due to engineering requirements, the diameter and the hub-ratio are usually specified in advance. The propeller diameter is usually chosen to fulfill the aerodynamic and aeroacoustic objectives. However, also structural, weight and space allocation requirements must be met, for which the propeller diameter is specified in advance. For the blade number, it is beneficial to have a high blade count due to a propeller efficiency increase and a noise reduction. By using more blades tip losses are reduced, thereby increasing propeller efficiency. Noise emissions are decreased because noise is shifted to higher frequencies, thereby also imposing more phase cancellation. However, higher blade numbers include a penalty in terms of a complex hub-pitch change mechanism[21]. Therefore, the selection of blade count remains a compromise.

For a propeller operating at high propulsor efficiency, the individual blades of the propeller should operate at maximum thrust to torque ratio. This can be achieved by an optimum airfoil shape-, twist- and chord distribution of the blades, which ensures a maximum lift-to-drag ratio along the radius of the propeller blade. Additionally, the advance ratio and the pitch setting of the propeller blades are an important factor in obtaining maximum thrust-to-torque ratio as well. For an isolated case, there are multiple approaches to determine the chord length distribution and the twist distribution of a propeller blade with an ideal load distribution. These include either a direct design routine or an an optimization approach. There are multiple direct design routines, including a blade-element approach or a trailing vortex system-method [11, 22]. For example, the Betz-condition for minimum energy loss can be used[23]. This condition gives rise to the desired circulation at each radial positions of the blade, which can be used to obtain the desired twist and chord distribution of the blade. By using an optimization routine, the design is treated as a search problem in which the optimum geometry is found for a maximum propeller efficiency.

Design considerations for low noise

Extensive literature is available on the influence of propeller design parameters on aeroacoustic performance[14, 21, 22, 24, 25]. Noise mitigation by changing the design of a propeller can be achieved by two different mechanisms: i) phase cancellation and ii) noise source strength reductions[24]. Noise mitigation due to phase cancellation (i) can primarily be attained by adding blades or by applying blade sweep. A great noise reduction can be achieved for propellers by the addition of blades. An example of the effect of different propeller design parameters on propulsor efficiency and noise characteristics is illustrated in figure 3.1.

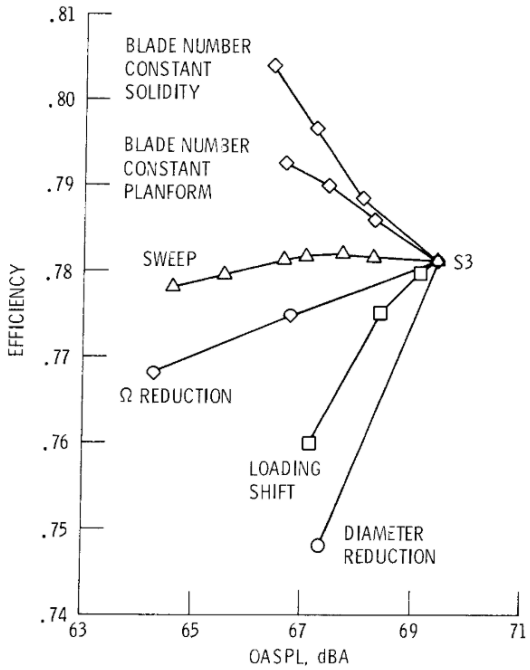

Figure 3.1: Optimized noise/propulsor efficiency trade-offs for a straight, three bladed baseline propeller configuration operating at a design point of J = 0.8 and a C_p = 0.154. The blade number increases from 3 to 6 with an increment of 1. The sweep angle is increased by increasing the sweep of the tip from 0° to 45° with unequal changes. The rotational speed is reduced with a 5% decrement, while the pressure coefficient is maintained by increasing blade loading. The shift in loading is done such that the peak in loading moved from 75% to 60%. The diameter is reduced by 5% [24].

The effect of the blade count is assessed by increasing the blade count from 3 to 6 in steps of 1 blade. As shown, for each of the increments the noise decreases and the propulsor efficiency increases. For the propulsor efficiency an increase occurs due to a reduction of blade loading, which subsequently leads to a reduction of tip and swirl losses. There is a difference between an increase of blade count with constant blade solidity and constant blade planform. An increment of the number of blades with a constant blade planform indicates that the geometry of the blade does not change when adding blades. An increment of the number of blades with a constant blade solidity means that the total blade area remains constant, which can be achieved by reducing the chord length along the radius of the propeller blades. The main reason of the occurrence of a noise reduction is a larger phase cancellation for certain harmonics, while the strength of the noise sources remain relatively constant.

Another noise reduction strategy due to phase cancellation includes the introduction of a sweep angle of the propeller blades. This mechanism is illustrated in figure 3.2. Sweeping back the blade causes a phase shift between the noise originating from different sections along the blade. The interference is illustrated by the vector addition of the amplitudes of the sound waves. For this type of blade, the vectors $A_1 ... A_N$ tend to induce a cancellation. Due to interference created by this phase difference caused by sweep, a significant noise reduction can be attained. The amount of noise reduction which can be attained is influenced by the propeller operating conditions, the observer location and the propeller geometry itself. As shown in figure 3.1, in this particular case a noise reduction of 5dB was achieved without the loss of propulsor efficiency. A drawback of the use of sweep to a propeller blade is that a large amount of sweep is needed when the tip Mach number is low, which can decrease the propulsor efficiency. The explanation for this statement relates to the effectiveness of the phase lag which is induces by the application of blade sweep. Since the phase lag is proportional to the ratio of MCA to the sound wavelength, a smaller sound wavelength is desired to increase effectiveness. A higher tip Mach number leads to a higher blade passage frequency, which reduced the sound wavelength. Therefore, high rotational Mach numbers are required for blade sweep to be effective.

An additional noise reduction strategy due to phase cancellation is to apply a lean angle to the blade, which is a displacement normal to the planform of the blade. However, according to Maggliozzi et al.[19], a small reduction of noise emissions can be expected by this design measure. Therefore, it is not considered in this thesis.

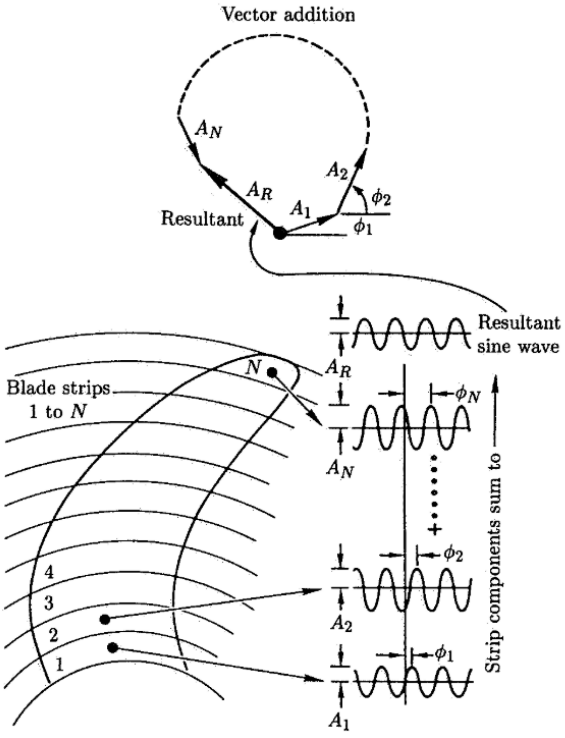

Figure 3.2: An illustration of the benefit of blade sweep back. Sweep causes signals from different radii to interfere, reducing the resulting signal strength[14]

Secondly, noise mitigation due to a reduction in noise source strength (ii) can be attained by reducing the rotational speed of the propeller. As a result, a higher pitch setting is required to maintain a similar thrust level, which leads to a higher angle of attack. A higher blade angle of attack leads to flow separation and thus, a higher required torque. On the contrary, the decrease in tip Mach number provides a decrease in noise source strength, leading to an improved aeroacoustic efficiency. As illustrated in figure 3.1, it is also possible to attain a noise reduction due to a shift in loading. However, the penalty in propulsor efficiency is significant due to a decrease of the effective propeller diameter. This noise mitigation measure reduces the strength of the high Mach number noise sources near the tip of the propeller. Additionally, Hanson [14] showed the effect of a uniform loading along the chord, contrary to a peaky loading distribution, results in a reduction of loading noise. This type of noise reduction relies on the noncompactness of the noise source. The noncompactness is the interference at the observer location of signals emitted from various noise source locations along the chord. If the chord is significantly large compared to the wavelength of the sound emissions, the noncompactness is large enough such that this type of noise reduction can be significant.

On the contrary, adverse effects could also occur when reducing the thickness, such as an increment in structural stresses and aeroelastic twist. Additionally, the reduction in thickness noise due to a modification in airfoil thickness distribution proves to be insignificant. Due to potential high noise reductions of the application of sweep to the blade design of a propeller, this measure is considered in this thesis.

3.2. Previous Optimization Studies

In this section the main findings of a selection of previous studies on multi-objective propeller optimization for a high propulsor efficiency and low noise are discussed. For this review, there is a focus on the optimization approach and the integration of various aerodynamic and aeroacoustic performance models. Besides, in each of these optimization studies a different set of design variables and constraints are selected, which have an impact on the generated results.

Miller et al.[24] created a preliminary design tool combining a vortex lattice aerodynamic analysis and a point source noise analysis to construct an optimization scheme using a conjugate direction method. In this optimization scheme, the result is called the index of performance (IP), which contains both aerodynamic and aeroacoustic performance. The index of performance was defined as the summation of an aerodynamic and an aeroacoustic objective, including a number of constraints:

$$IP = a(-C_T) + (1-a) \cdot bN + constraints \tag{3.1}$$

In which a represents the relative importance of each objective, C_T is the thrust coefficient, b is a normalisation for noise emissions and N is the overall sound pressure level in dB. In the constraints, the power coefficient is kept constant and a maximum sweep and circulation are induced. In the index of performance Miller was able to change the relative importance of each objective, which yielded different optimum propeller geometries. Using this method, design variables included the twist, chord and sweep distributions. The results of this optimization study led to the findings discussed in the previous section.

In 2008, Pagano et al.[9] presented an optimization scheme in which the aero-structural performance was included, next to the aeroacoustic and aerodynamic performance. The propeller aerodynamic analysis included a simple numerical tool based on blade element momentum-theory, in conjugation with a physics-based surrogate model. The baseline design and an optimum design are depicted in figure 3.3. A sweep angle is introduced near the tip of the blade in the optimum blade design, underlining the effect of blade sweep to mitigate noise. The sweep induced near the tip of the blade resulted in a decrease of 1.5 dB for a six-bladed propeller, while the propeller efficiency change for this planform has not been highlighted. Unfortunately, the generation of the surrogate model proved a challenge due to grid generation problems of the CFD-model and robustness problems arose when complex analysis was embedded into the optimization routine.

In 2011, Marinus [7] presented a multidisciplinary design optimization, in which aeroacoustic, aerodynamic and aeroelastic effects are included. The aerodynamic performance is calculated by a Reynolds-Averaged Navier-Stokes (RANS) implementation, which is used to generate a surrogate model. Subsequently, the surrogate model was used in the optimization framework, since this is faster compared to using the complete RANS-model. Due to the higher fidelity of the tool, more accurate results were expected. However, convergence and mesh failures led to a significant failure rate. Despite the convergence issues, valuable results were extracted. This study included a significant amount of design variables including the twist-, thickness-, sweep- and chord distribution in addition to certain airfoil properties. These distributions were modelled by a b-spline interpolation which were defined by a number of control points, allowing a reasonably small amount of design variables.

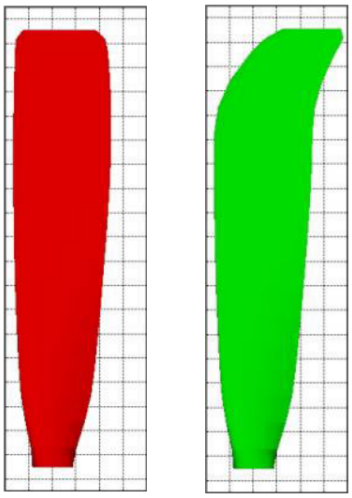

Figure 3.3: Comparison of a baseline (left) and an optimum blade design (right) by Pagano et al.[9]

The use of control points to define radial distributions leads to a computationally efficient optimization process due to the low amount of design variables. This procedure is used in this thesis as well, as discussed in chapter 4.

The objective functions for which the design variables were optimized included an aggregate of three key performance indicators at cruise- and take-off/landing conditions. Three objective functions were defined, which were all included in the optimization by a multi-point and multidisciplinary optimization. The key performance indicators included both propeller power and the sound pressure level at different locations. The resulting blade geometries are depicted in figure 3.4. These blade geometries extracted from the optimization routine proved to have low values for three different objective functions. As illustrated, the results show that blade sweep is present especially near the tip of the blade for the optimum blades c and d. These blades are selected from 28 individual solutions, which all satisfy the constraints and have the lowest objective values. Research by Pagano et al.[9] and Marinus[7] both proved that the use of a CFD-model and the derived surrogate model to determine aerodynamic performance in an optimization scheme can be a challenge due to meshing errors and convergence issues. Due to these challenges associated with higher-order numerical tools, these models are not used in this thesis. Therefore, low-order numerical tools are used to determine aerodynamic and aeroacoustic performance. These tools have the advantageous characteristic that a low computational time can be expected, while a proper verification process should be performed to ensure accurate results.

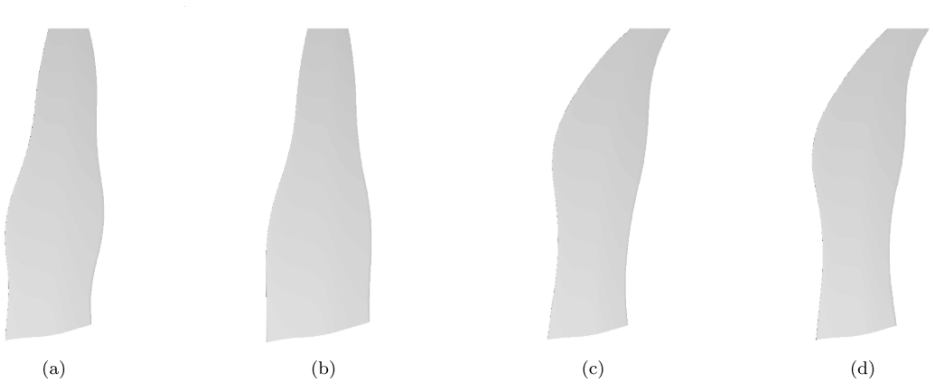

Figure 3.4: Comparison of benchmark (a), central (b) and optimum (c,d) blade designs by Marinus et al.[7]

Gur&Rosen[8] also presented an optimization study to design quiet and efficient propeller blades. This work is similar to the study by Pagano[9]. However, no investigation into the application of blade sweep on aerodynamic and aeroacoustic results is performed. A BEM method is used to calculate the aerodynamic performance, without the use of a higher fidelity surrogate model. As discussed by Gur, the BEM-model is an efficient and accurate model which is suitable for an application in an optimization framework. Additionally, the optimization scheme which is used includes a mixed strategy approach, combining several optimization methods. In this study, the effect of structural and additional constraints, such as a power constraints and performance constraints, on the optimum propeller geometry are shown. Due to the structural constraint a thickening of the propeller blades is induced, which lead to a noise increase of 2dB. The effect of structural and side constraints will not be included in this thesis for simplicity. Instead, the bounds on the design variables will be defined such that a feasible design can be expected. Additionally, an important conclusion which is reviewed in this thesis is that the main mechanism to reduce propeller noise for a given amount of blades involves a reduction of the propeller rotational speed.

A recent study by Geng et al.[15] used a simple BEM-model as an aerodynamic model and Hanson's Helicoidal surface theory as a noise model. An objective function was used which optimized the propeller for a low thrust specific noise, with a constraining propulsor efficiency and a constraining thrust coefficient C_T. Similar to this thesis, the primary design variable which was investigated is blade sweep, while the blade twist and chord length distribution along the radial direction remained unchanged. The resulting blade planform is shown in figure 3.5, which is complemented by the radial sweep distribution shown in figure 3.6. The propeller including the optimized blades provided a 2.9dB reduction in TSSP over a range of directivities with respect to the propeller including the baseline blades, without a reduction in thrust coefficient and propeller efficiency. As a result, an overall reduction in acoustic emissions was achieved by this optimum blade planform.

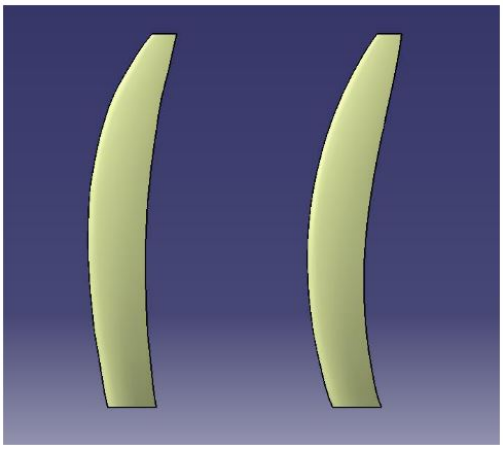

Figure 3.5: Comparison of baseline and optimum blade planform shapes generated by Geng et al.[15]

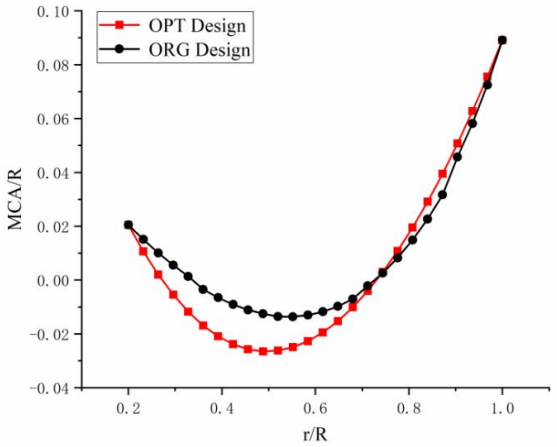

Figure 3.6: Comparison of baseline and optimum sweep distributions generated by Geng et al.[15]

In 2019, a gradient-based optimization study was performed by Ingraham et al.[26]. In this study, a propeller performance code and an acoustic prediction tool were used in combination with a gradient-based optimization to analyze and optimize propeller designs. As a baseline propeller, the propellers on the X-57 Maxwell were used. The objective function included a maximization for propeller efficiency, which was subjected to a thrust equality constraint and a range of maximum overall sound pressure levels (OASPL). Two cases were considered: a case including twist and chord distribution as design variables and a case including propeller diameter and rotational speed as design variables. For the first case, the noise is reduced by moving blade loading more inboard by increasing chord/twist inboard and decreasing chord/twist outboard, as shown in figure 3.7. The noise reduction obtained in this case was a maximum of 1dB in OASPL. For the second case, a noise reduction of 5dB could be obtained, at a cost of 1% in propeller efficiency. For this case, a maximization of the propeller diameter and a minimization of the propeller rotational rate was desired by the optimizer. There was no assessment of blade sweep in this study, but it did prove valuable results could be obtained by gradient based optimization using low-order numerical tools.

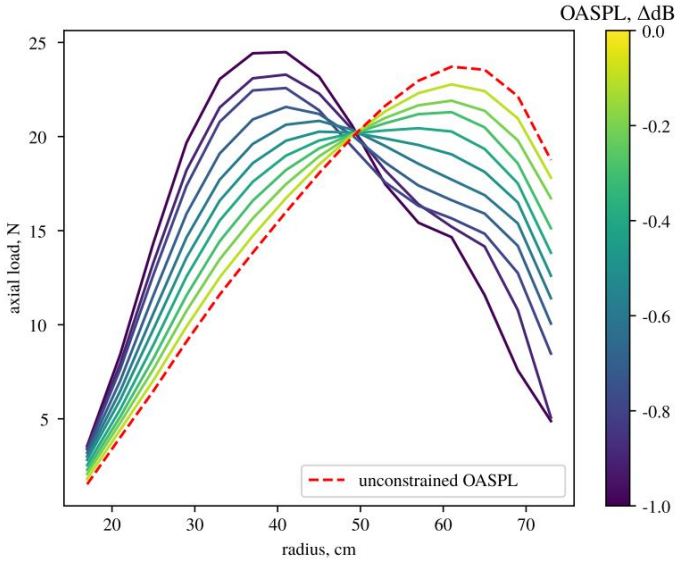

Figure 3.7: Effect of shift in blade loading on OASPL, as obtained by increasing chord and twist inboard and decreasing chord and twist outboard.

A final study which serves as background for this thesis is the master thesis by Burger[20]. This is not an optimization study, but a sensitivity study. 993 random propeller geometry designs have been evaluated to perform a sensitivity study, thereby quantifying the trade-off between propeller efficiency and noise emissions. These designs only differed in the radial sweep distribution, while other design variables were identical. Similarly to the previously discussed work by Geng et al., the BEM-model and the HST-model were used as aerodynamic and aeroacoustic performance tools. Additionally, higher-fidelity RANS-simulations were used to verify the results generated by the lower order BEM-model. Main findings of this thesis included that a noise reduction of 13dB at a cost of 3.4% in propeller efficiency could potentially be gained by only adjusting pitch and advance ratio for a given design. Additionally, designing a blade with a forward or backward sweep of approximately 20 degrees was found to be beneficial for noise reduction. A key recommendation which was made is to use an optimization routine to obtain a clearer trade-off between noise and efficiency as a function of the blade parameters. This may lead to more insight regarding phase delay by adding sweep. This recommendation was used to set the research objective of this thesis.

II

Research Tools

4

Propeller Geometry Parametrisation

An essential element of this optimization study is the parametrisation of the propeller geometry. The parametrisation of propeller geometry is the process of describing the geometry of a propeller in terms of a mathematical representation. For the purpose of a successful optimization study, it is required to provide an adequate set of design variables to the optimization algorithm. This means, a small amount of design variables should be provided which can accurately represent the propeller geometry.

For this optimization study, the challenge of parametrisation is to accurately express radial distributions of chord, sweep and twist of the propeller blades in a small amount of design variables. In section 4.1, a discussion of three methods to parametrise a radial distribution is provided. Additionally, an elaboration is given on the selected method, a Bézier curve representation. Subsequently, in section 4.2, a complete overview is provided including explanations of all design variables which mathematically represent an entire propeller geometry. The propeller geometry parametrisation presented in this section is based on previous optimization studies[8, 20, 27].

4.1. Representation of Radial Distributions

The mathematical representation of the radial distributions of sweep, chord and twist are needed for an optimization study in propeller blade design. A possibility is to use the twist, chord and sweep values of each of the radial segments. However, the aerodynamic and aeroacoustic characteristics are calculated at 25 blade elements in this optimization study. This would yield 25 design variables for each of the previously mentioned design variables and the computational costs would be excessive. Moreover, if these blade sections are individually optimized, there is a high probability to obtain non-smooth radial distributions of the design variables, which subsequently yields unfeasible designs.

Therefore, parametric curves are often used, defined by a small amount of control points. An area where these curves are used on a more regular basis is the field of computer graphics[28]. This results in broad availability of literature describing the working principles of these curves. The solution of using these curves allows the number of design variables to remain small. The effect of different types of parametric curves on the results is studied in this thesis, with the considered types of parametric curves being the following:

- **Bézier-curves**
  Bézier curves are curves which are defined by a number of control points. The curve does not pass through these points, but it is attracted by the points. The influence of each point is the strongest when the curve is nearest to the control point. Next to a set of control points, Bézier curves are also defined by a set of Bernstein polynomials, which are basis functions for the curve. An important property of the curve is that the first- and last control point are also the starting- and end point of the curve. This means, by moving the control points of the curve, the curve is allowed to change in shape. In the optimization study, these control points are design variables to change the radial distribution of mid-chord alignment.

- **NURBS-curves**
  A different approach is to use Non-Uniform Rational B-Splines (NURBS-curves), which is a more versatile curve type compared to the Bézier curve. Similar to a Bézier curve, a NURBS-curve is defined by a set of control points. Additionally, a NURBS-curve is also defined by a knot-vector and a set of weights, which can both change the shape of the curve. This means a NURBS-curve is the most general parametric curve

available, due to the many shapes which can be attained by changing the knot-vector, the weights and the control points[28].

An example of both a Bézier curve and a NURBS curve representation is shown in figure 4.1, for the control points tabulated in table 4.1. It becomes apparent that the control points for the NURBS-curve can exert a larger influence on the curve with respect to the Bézier curve. In figure 4.1b, by changing the knot-vector or the weight-vector, the NURBS-curve can change shape, while the Bézier curve in figure 4.1a is only defined by a set of control points.

Table 4.1: Control point coordinates of examples shown in figure 4.1

X-Coordinate	Y-Coordinate
0.5	0.0
0.7	0.33
0.2	0.8
1.0	1.0

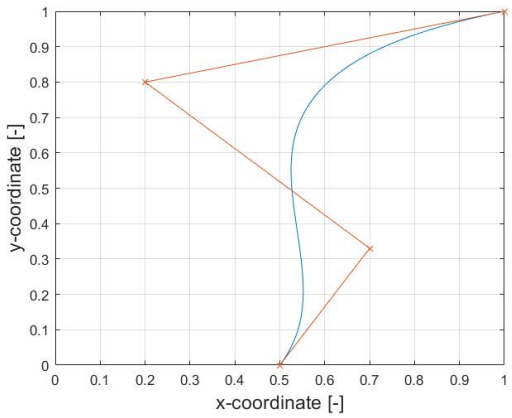

(a) Bézier curve example

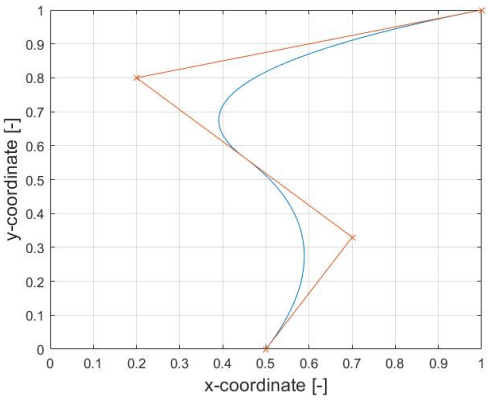

(b) NURBS curve example

Figure 4.1: Bézier and NURBS curve examples for the control points shown in table 4.1

For this optimization study, the Bézier curve implementation was used to represent the radial distribution of sweep. The Bézier curve was preferred over the NURBS-curve due to its simplicity. For an optimization using a Bézier curve implementation, only the control points are implemented as design variables, while a NURBS-curve also offers the possibility to include design variables for the knot-vector and the weights-vector of the curve. This means a Bézier curve limits the amount of design variables, which saves computational time. Despite the advantage of the NURBS-curve of allowing more complex shapes, the smooth continuous curves which can be created by the Bézier curve increases the feasibility of the design. Additionally, previously performed optimization studies successfully used Bézier curves in their numerical models[7, 9]. Based on these advantages, the Bézier curve implementation is used.

For the implementation of the Bézier curve, the Bernstein formulation of the Bézier curve is used (equation 4.1). As shown, the Bézier curve is represented by a weighted sum of the control points $\mathbf{P}_i$ and a set of Bernstein polynomials $B_{n,i}(t)$. The i-th control point is denoted by $\mathbf{P}_i$. These control points are a set of coordinates on the (X,Y) grid whereby $0 \leq X \leq 1$ and $0 \leq Y \leq 1$. The degree of the curve is given by n, which is equal to the number of control points + 1.

$$\mathbf{P}(t) = \sum_{i=0}^{n} \mathbf{P}_i B_{n,i}(t) \tag{4.1}$$

The Bernstein polynomial-functions act as different weights for the Bézier-curve, which are defined in equation 4.2. These weights can be considered as blending functions, which blend the contributions of all control points on the curve.

$$B_{n,i}(t) = \binom{n}{i} t^i (1-t)^{n-i} \tag{4.2}$$

where:

$$0 \leq t \leq 1$$

In figure 4.2, the basis functions for Bézier-curves of 3 and 4 control points are shown. In this figure, each of the curves represents the weight of each control point along the length of the curve. In the case of 3 control points, there are three Bernstein polynomials $B_{20}(t)$, $B_{21}(t)$ and $B_{22}(t)$. An interesting property of the Bézier curve is that the curve starts at the first control point and ends at the last control point. This can be confirmed by looking the first Bernstein polynomial $B_{20}(t)$, which is 1 at t = 0 (figure 4.2a). Since the values of the other Bernstein polynomials are 0 at t = 0, the other control points do not influence the curve at t = 0. Therefore, the curve starts at the first control point. This is also true for the last Bernstein polynomial $B_{22}(t)$. The implementation of the Bézier curve as a radial distribution for sweep in the optimization study is discussed in chapter 7.

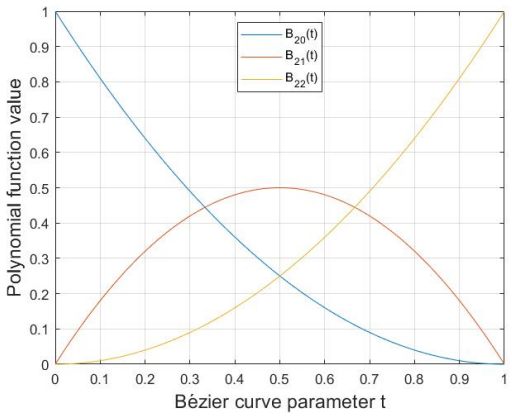

(a) Bernstein polynomials for a 2^{nd} order curve with three control points

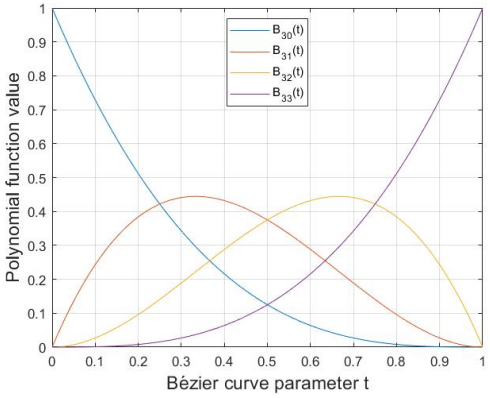

(b) Bernstein polynomials for a 3^{rd} order curve with four control points (for a curve depicted in figure 4.1a)

Figure 4.2: Bernstein polynomials acting as basis functions for Bézier curves. Basis functions for a 2^{nd} order curve and a 3^{rd} order curve are shown.

4.2. Propeller Design Variables

In this section, the discussion is focused on the parametrisation of the design variables that were mentioned in section 3.1. First, 2D cross-sectional airfoil shape characteristics of the blades are discussed. Second, design variables of the 3D propeller blades are considered. Finally, overall propeller design variables, such as diameter and blade count are discussed. Additionally, the introduction of key geometry parameters in this section forms a basis for the selection of aerodynamic and aeroacoustic numerical models in chapter 5 and 6.

For this optimization study, the shape of the propeller hub is not considered, which means the drag created by the propeller hub is not taken into account when calculating the propeller thrust. However, the assumption is also made that the hub does not influence the optimization study, thus comparing the effect of different blade designs on propeller performance is not influenced by including the propeller hub.

2D Airfoil shape

The **airfoil shape** along the blade is a cross-sectional design variable which varies along the radius of the propeller. Due to an increase of the velocity component in rotational direction when increasing the radial coordinate, an airfoil at a larger radius is usually thinner compared to an airfoil near the root. The airfoil shape at each section can be defined by a NACA profile or the previously mentioned Bézier curve representation can be used to describe the upper and lower part of the airfoil. However, including this design variable in the optimization increases the computational cost due to the high amount of associated design variables. Therefore, the effect of airfoil design along the radius on propeller performance is not included in this thesis. As a result, this optimization study is performed using the unmodified cross-sections of the baseline propeller.

3D Blade design variables

The **twist distribution** $\beta(r)$ is the distribution of the twist angle along the radius of propeller blades. The twist angle of an airfoil section at radial position r is defined as the angle between its chord line and the chord line of the airfoil section at radial position of r/R = 0.7. Due to a difference in inflow angle along the radius of the propeller, the twist angle is required to change along the radius to ensure an optimum loading distribution along the propeller blade. Thus, an optimized twist distribution is critical to obtain an efficient propeller.

The **chord distribution** $c(r)$ is defined as the distribution of chord length along the radius of the blade. Similar to the twist distribution, an optimized chord distribution is also critical to obtain an efficient propeller, since the loading distribution of the blade is affected by the chord distribution. This is because an increase in chord length leads to an increase of local lift and drag forces.

Hanson [27] defined the **mid-chord alignment** $MCA(r)$ as the offset between the mid-chord point and the root-plane at each blade element, illustrated in figure 4.3. Application of mid-chord alignment to a propeller blade design can cause destructive interference between sound-waves originating from different blade elements at the blade, which can lead to a decrease in sound pressure originating from the propeller. Therefore, the MCA-distribution is a design variable which is included in the optimization study. A fully dependent design variable is the blade sweep angle $\Lambda(r)$. The calculation of the blade sweep angle along the blade is necessary, since the blade sweep angle along the radius is needed for aerodynamic performance models. The blade sweep is defined as the angle between the mid-chord of two adjacent blade elements, as shown in equation 4.3. The relation between the mid-chord alignment and the blade sweep angle at a blade element is illustrated in figure 4.4. In this figure the blade section is swept back with respect to an adjacent blade section. This means that a blade section is swept backwards when it has a positive MCA and a positive blade sweep. An accurate representation of blade sweep angle requires small distances between adjacent blade elements.

$$\Lambda_i = \arctan\left(\frac{MCA_{i+1} - MCA_i}{r_{i+1} - r_i}\right) \tag{4.3}$$

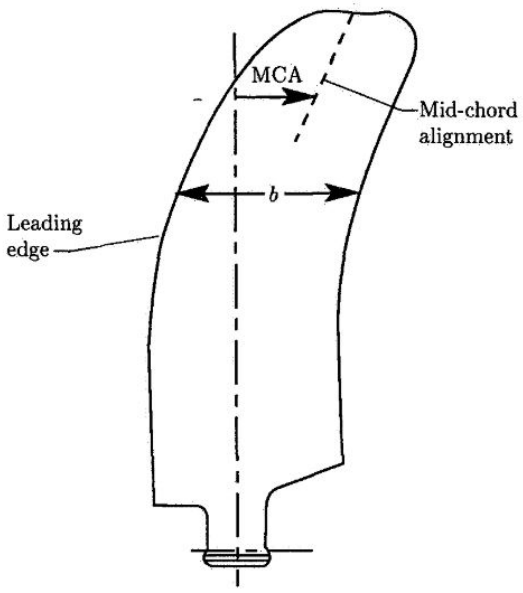

Figure 4.3: Definition of the mid-chord alignment illustrated [13]

Usually, when assessing the sweep angle in aircraft wings, often the quarter-chord sweep angle is used. In BEMT-approach by Gur et al.[29], the quarter-chord sweep angle is used to determine the effect of blade sweep on aerodynamic performance. However, in this thesis a mid-chord sweep is used, since out of plane movement of the leading edge and the trailing edge of the blade is averaged by this definition. A detailed explanation of the use of mid-chord sweep instead of quarter-chord sweep can be found in the work by Burger[20].

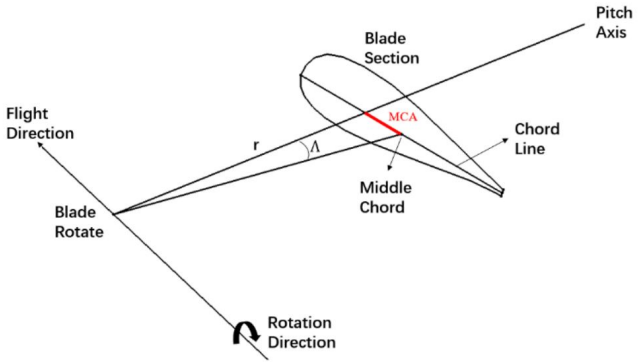

Figure 4.4: Relation between Blade sweep and MCA[15]

Additional variables are the **face alignment**, often denoted by FA, and its dependent variable blade lean angle, denoted by Ψ. The face alignment is defined as the ofsett normal to the blade between the pitch axis and the blade section. Similar to the blade sweep angle and mid-chord alignment, the lean angle is fully dependent on the face alignment. The definition of mid-chord alignment and face alignment is shown in figure 4.5. The variables face alignment and lean angle are included in this overview for completeness, since these are not considered in this thesis due to a weak effect on noise reduction[19].

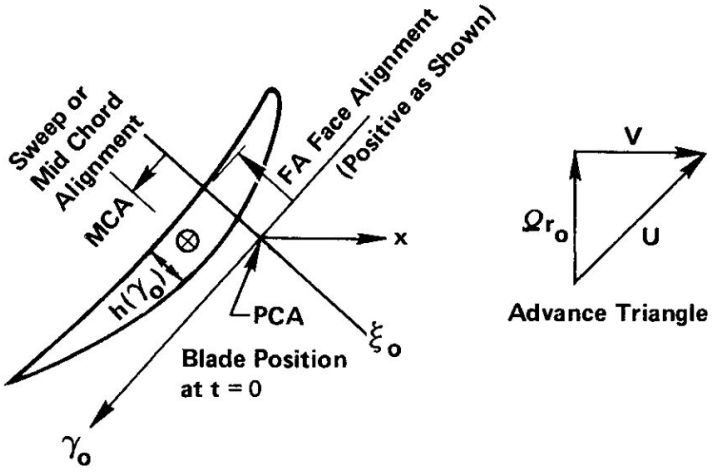

Figure 4.5: Blade section shown in helical coordinates including definition of face alignment and mid-chord alignment[27]

Overall propeller design variables

Since a large **propeller diameter** D_p leads to a high propulsive efficiency due to the higher attainable air mass flow, a large propeller diameter is desired. However, due to operational conditions limiting the tip Mach number, structural constraints, sizing constraints or other types of constraints, the maximum propeller diameter is often limited. In this optimization study, the effect of propeller diameter on propeller performance is not considered, since this is out of the scope of this study.

The **number of blades** N_b of the propeller can have a significant impact on both propulsive efficiency and noise emissions[8, 24]. The individual blade loading changes if there is a change in number of blades. An increase in blade number implies a decrease in blade loading, which decreases the tip losses and thereby the propulsive efficiency increases. A change in noise emissions due to a change in blade number is caused by a change in fundamental blade passing frequency and acoustic interference. However, often the number of blades is limited by mechanical complexity in the hub. In this study, the effect of number of blades on propeller performance is not considered, since this is out of the scope of this study.

The **collective blade pitch** β is defined as the angle between chord line at 70% of the blade radius and the azimuthal plane. Thus, a collective pitch angle of zero degrees means that the chord line at r/R = 0.7 runs parallel to the azimuth. It should be noted that this variable is not classified as a design variable in this thesis, but rather as an operational variable. Often, for fixed speed propellers this variable can be changed in-flight, to operate at an optimum propulsor efficiency.

5

Aerodynamic Numerical Model

Numerical models used to determine the propulsor performance of a propeller in the optimization study are discussed in this chapter. In order to perform a successful optimization, an accurate and fast numerical model is of great importance. Therefore, a numerical model is chosen which is both computationally efficient and provides accurate results. Firstly, in section 5.1, prior to the discussion of the numerical model, the justification for the choice of the model is explained. Secondly, the background and implementation of the chosen isolated propeller model is discussed in section 5.2. Verification and validation of this model is discussed in chapter 8.

5.1. Aerodynamic Numerical Model Selection

For aerodynamic performance prediction of propellers, various numerical models are available which all have their own advantages and disadvantages. In this study, the decision was made to perform the numerical analysis using low-order numerical models. This decision was made to decrease the computational costs. For an application in a low-order study, the main consideration for choosing a model is the trade-off between the accuracy of the model and the required computational power. To argue the choice for a specific aerodynamic performance model, the results and limitations of different available models are discussed in this section.

For an isolated propeller, a propeller subjected to uniform inflow, there are a number of low-order methods available. The simplest model to calculate propeller propulsor performance, the actuator disk model, is not included. Although the actuator disk model can estimate the induced axial velocity in the slipstream of the propeller, it fails to accurately predict key performance indicators of the propeller[2]. Additionally, the method does not allow to take different blade geometry parameters into account. Therefore, this method is not considered. The various models[30] which are considered include:

- Blade Element Momentum-model
- Lifting line-model - Based on Prandtl's lifting line theory
- Vortex-models - Based on optimum distribution of blade's circulation and Kutta-Joukowski condition

The comparison between the considered numerical methods is based on research performed by Gur&Rosen[30], who generated results by various aerodynamic performance models and by a wind-tunnel test campaign. The key performance indicators of the comparison included the thrust coefficient, power coefficient and propulsor efficiency for a range of advance ratios. Various propellers with different blade counts and application of sweep angles were tested. Since the optimization study will also include sweep as a design variable, the generated results for swept blades are of importance as well.

For a straight-bladed propeller operating at a low pitch setting and a high advance ratio in axial conditions, a simple model is recommended since differences in propulsor efficiency are negligible. Larger differences exist when the propeller operates at a high thrust-level and a low advance ratio. At these conditions, it appeared that for the propellers with straight blades the lifting line model and the Theodorsen model overpredict the thrust and power coefficient, while McCormick model underpredicts the test results[30]. The simplified momentum model, which is a simplification of the BEM-model, showed results which were in agreement with experimental results. Furthermore, the advantages of a BEM-model are the simplicity, accuracy and low demand of computational resources. Additionally, the BEM-model offers the capability to include many geometrical parameters

of the propeller blades. According to Branlard et al.[31], the BEM-model can generate results in a matter of seconds, while lifting-line models and Vortex models can be in the order of minutes. Since an optimization process requires a large number of evaluations of the propulsive numerical model, the BEM-model is suitable for this application due to high accuracy and numerical efficiency. Considering these advantages and its correspondence with experimental results, it was decided to use a BEM model as a propulsive performance model in the optimization study.

When considering a propeller with swept blades, the relation between the modelled and experimental results becomes different. In figure 5.1, results are depicted for a propeller with two swept blades. For a propeller with swept blades, most of the numerical models overpredict the test results. McCormick's model is the only model which shows fair agreement with the test results for a propeller with swept blades. According to Gur&Rosen, an explanation for the overprediction of most models could be that the elastic torsion in the blades due to sweep is not taken into account[30]. The elastic torsion generated by the sweep angle could lead to a smaller elastic pitch angle in the wind-tunnel experiment. McCormick's model is not selected however, since it underpredicts results for a propeller including straight blades.

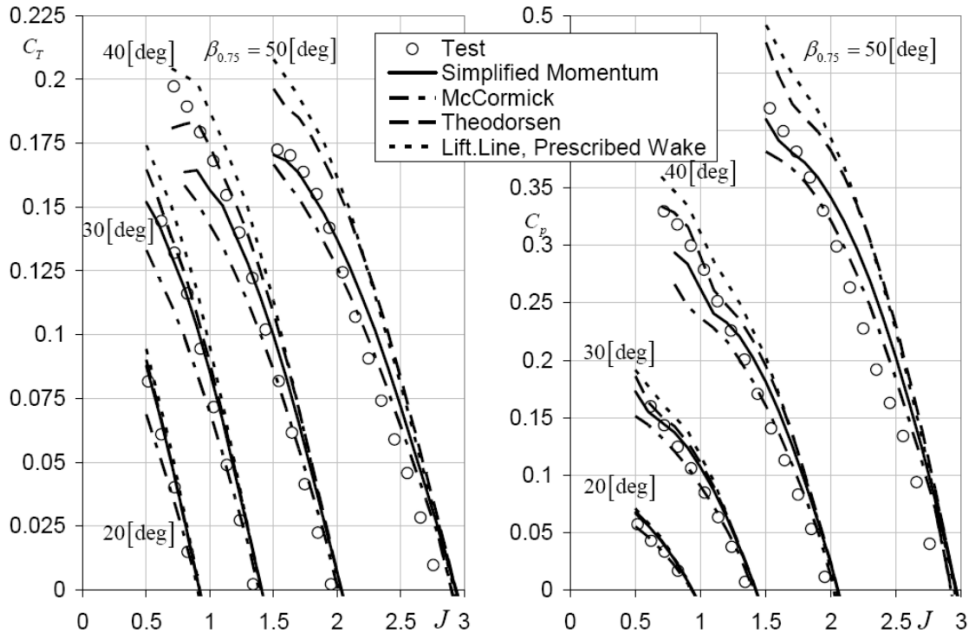

Figure 5.1: Comparison between results generated by aerodynamic numerical models and experimental results of a two bladed swept propeller [30]

However, it should be noted that the classical implementation of the BEM-theory lacks the incorporation of blade sweep as a design variable. There is no dependency to blade sweep in the classic BEM-implementation since the blades are divided into small elements along the radial direction, in which it is assumed each element behaves as a 2D-wing. Additionally, there is no radial interference between elements. These assumptions limit the ability for the classic implementation to take blade sweep into account. Since blade sweep is considered in the optimization study, a BEM-model including blade sweep is used. A method developed by Geng et al.[15], which models the effect of sweep assuming the blade as an infinite wing, is used as an extension to the BEM-model. Additionally, the BEM-model requires corrections for the hub and tip-losses of the blade. It is assumed that the advantages of the BEM-model outweigh the potential accuracy losses and that are induced by the previously mentioned adaptations. The general theory and the implementation of the model are described in section 5.2.

5.2. Aerodynamic Performance Prediction Method

In this section, the background theory of the BEM-model is treated, including key assumptions that are made when using this model. Subsequently, the implementation of the BEM-model in the optimization study is discussed. Since the classical implementation of the BEM-model does not consider a dependency to blade sweep, a correction to the model has to be made, which is also discussed.

5.2.1. General BEM-Theory

The BEM-model is a model in which the momentum theory or actuator disk theory and the blade element theory are combined. These theories including their assumptions, which are relevant for the BEM-model as well, are treated in this section.

Actuator Disk Theory

In actuator disk theory, also known as classical momentum theory, the propeller is replaced by an ideal actuator disk. The roots of this theory are in marine propulsion applications, where Rankine introduced the model[32]. In this theory, the flow is assumed to be captured in a well-defined streamtube. Due to the increase of axial velocity the streamtube is contracting, as shown in figure 5.2. For the flow properties throughout this streamtube, Bernoulli's theory is used. It is assumed that the thrust generated by the actuator disk exists due to the momentum difference far upstream and far downstream in the streamtube. This momentum difference is achieved due to the instantaneous increase in total pressure at the actuator disk. Using the actuator disk model means a number of assumptions are made[2]:

- The freestream flow is steady, inviscid and incompressible.
- The flow passing through the propeller is separated from the rest of the flow by a well-defined streamtube.
- The rotation of the flow which is imparted on the flow is neglected.
- The pressure and velocity are distributed uniformly over the disk.

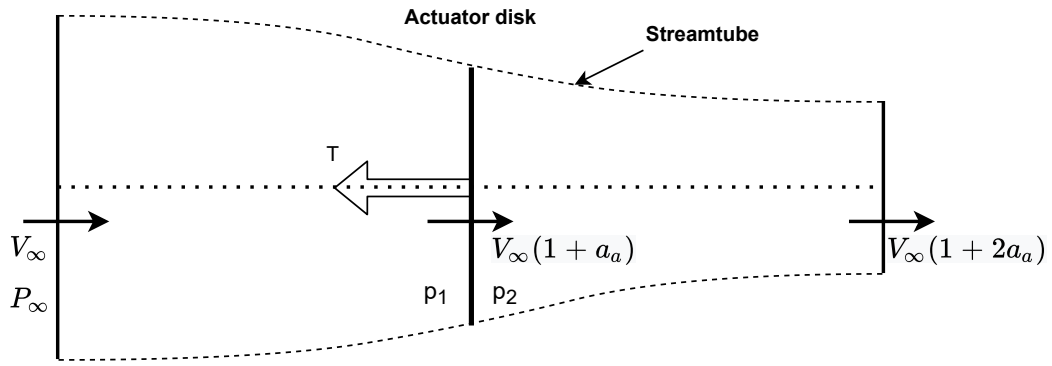

Figure 5.2: Representation of the actuator disk theory, showing the contracting streamtube, the actuator disk and the properties of the flow far upstream and downstream.

Blade Element Theory

Blade Element theory is combined with the actuator disk model in the BEM-model. By using blade theory, it is assumed that the streamtube as shown in figure 5.2 can be divided in several annular streamtube control volumes. As a result, the boundaries of these control volumes divide the blades in blade elements of width dr. This allows the geometry of the blade to be taken into account in the calculation of aerodynamic performance characteristics. In Blade Element theory, is it assumed that the relevant two-dimensional forces of each blade element can be determined by using the shape of the blade element and the blade angle of attack α. In figure 2.1, a 2D blade element is shown including the relevant forces - torque and thrust - and velocities.
By combining the Blade Element theory and the Momentum theory, the following assumptions are made:

- The momentum increase in each of the annular streamtubes is the result of thrust and torque forces generated by each blade element.
- There is no radial interaction effect between blade elements/annular streamtubes.

- In the combination of Blade Element and Momentum theory, the assumption of uniform velocity and loading over the entire actuator disk is no longer valid. However, by subdividing the disk into smaller annuli, the assumption of uniform loading and velocity is valid considering the individual annuli.

Thus, in each of the individual annuli over the disk a constant loading is assumed. This assumption enables an assessment of the radial distributions of thrust and torque over the propeller blades.

Due to the two-dimensional analysis of the blade elements, the effects of vortices leaving the root and tip of the blade on the propeller induced velocity field are not considered in the Blade Element Momentum theory. The blade induced velocity field is negatively affected by the vortices leaving the blade. Therefore, Prandtl's loss correction factor is applied when using the BEM-model to correct for this loss effect.

5.2.2. BEM-model Implementation

The BEM-implementation used in the optimization study is based on work of Liu et al.[33] and Geng et al.[15]. In these papers, a classic implementation of the Blade Element and Momentum theory is provided, including a correction method for blade sweep. The solution procedure of the BEM-implementation is shown in figure 5.3. The analysis chain can be divided into three stages: initial calculations (stage 1), calculation of induction factors for all blade elements (stage 2) and calculation of overall propeller performance (stage 3). In this section, the implementation of the BEM-model is explained based on these three stages.

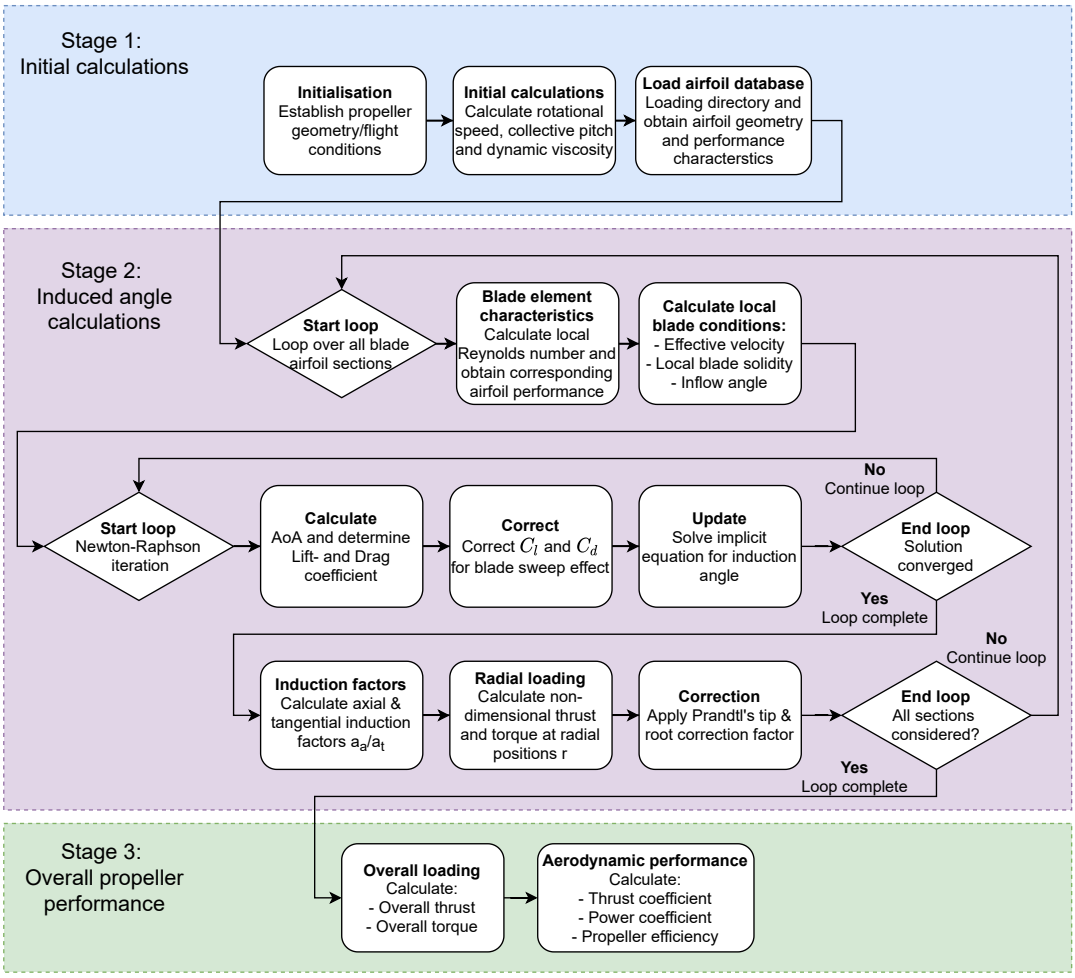

Figure 5.3: Flowchart of Blade Element Momentum model implementation

Stage 1: Initial calculations

In the first stage, the propeller geometry together with the flight conditions and simulation setup are defined. According to BEM-theory, the disk is divided into a number of annuli. In this implementation, 25 different annuli are used. The twist angle of the blade induces a different pitch angle for each of these annuli. This means the pitch angle at a certain radial coordinate r is defined as the twist at that radial coordinate r added to the pitch at r/R = 70%. The rotational speed in rad/s, which is constant along the radius, is defined as:

$$\Omega = 2\pi \frac{V_\infty}{JD_p} \tag{5.1}$$

Additionally, an initial calculation is made of the blade solidity of a blade cross section at radial position r (equation 5.2).

$$\sigma = \frac{N_b c}{2\pi r} \tag{5.2}$$

The computationally expensive task of calculating airfoil properties is done beforehand and stored in a database, such that it can be easily accessed during the BEM-calculations. For the generation of this database, RFOIL[34] was used to determine the lift and drag coefficient and the pressure distribution of each blade element. RFOIL, a modification of XFOIL, is a program for the design and analysis of isolated airfoils. This program uses a linear-vorticity panel method to determine lift and drag coefficients. A grid sweep was performed for a range of angle of attack and Reynolds number for each blade element. These range in angle of attack and Reynolds number are discussed in stage 2. For each of the airfoil-simulations, the lift and drag coefficients are not corrected for compressibility by the RFOIL code itself, because this correction is performed in the BEM-model. The result of the RFOIL simulations are interpolants of C_l and C_d for a specific Reynolds number and blade element, which are used in the BEM-model. In addition to the lift and drag coefficients generated by RFOIL, the program also generates corresponding pressure distributions of the blade sections. These pressure distributions are used for the aeroacoustic model, discussed in chapter 6.

Stage 2: Induced angle calculations

The second stage of the BEM-implementation includes a Newton-Raphson iteration to obtain the axial- and tangential induction factors, as shown in the purple box in figure 5.3. For each blade element, initial calculations are performed to determine the inflow angle (equation 5.3) and the effective velocity (equation 5.4). These equations are based on the blade elements as shown in figure 2.1. The inflow angle is the angle between the freestream velocity vector and the local rotational velocity vector at a radial coordinate r. The corresponding effective velocity is calculated by the vector addition of the freestream velocity vector and the rotational velocity vector at radial coordinate r.

$$\phi_0 = \arctan\left(\frac{V_\infty}{r\Omega}\right) \tag{5.3}$$

$$V_{eff} = \sqrt{V_\infty^2 + (r\Omega)^2} \tag{5.4}$$

The effective velocity is used to determine the Reynolds number (equation 5.5) and the Mach number (equation 5.6). These variables are required to obtain proper lift and drag coefficients which are corrected for compressibility and Reynolds number.

$$Re = \frac{\rho V_{eff} c}{\mu} \tag{5.5}$$

$$M = \frac{V_{eff}}{\sqrt{\gamma RT}} \tag{5.6}$$

As discussed previously, by using the BEM-model, blade element- and momentum theory are combined. The assumption is made that the momentum increase in each annular streamtube is the result of the forces generated by the blade elements. Therefore, the incremental thrust dT and torque dM calculated by blade element theory and momentum theory should be equal. Blade element theory provides the following expressions for incremental thrust dT and torque dM:

$$\begin{aligned} dT &= \frac{1}{2}\rho V^2 C_L b \frac{\cos(\phi+\gamma)}{\cos(\phi)} dr \\ &= \frac{1}{2}\rho V^2 \frac{C_L b(1+a)^2}{\sin^2\phi\cos\gamma} \sin(\phi+\gamma) dr \end{aligned} \tag{5.7}$$

$$dM = \frac{1}{2}\rho V^2 \frac{C_L b(1+a)^2}{\sin(\phi)\cos(\gamma)} r\sin(\phi+\gamma) dr \tag{5.8}$$

On the other hand, the incremental thrust dT and torque dM as derived by momentum theory are:

$$dT = 4\pi r \rho V_\infty^2 a_a (1+a_a) dr \tag{5.9}$$

$$dM = 4\pi r^2 \rho V_\infty (2\pi r n) a_t (1+a_a) dr \tag{5.10}$$

A more complete derivation of these expressions can be found in the work by Liu et al.[33]. By equalling these definitions for incremental thrust (equation 5.7 to equation 5.9) and torque (equation 5.8 to equation 5.10), an expression can be derived in which the loading derived from momentum theory and the loading derived from blade element theory is equal. This expression is shown in equation 5.11.

$$C_L\sigma = \frac{4\sin(\phi_0+\phi_i)\tan(\phi_i)}{1-(C_d/C_l)\tan(\phi_i)} \tag{5.11}$$

This is a single equation with one unknown: the angle due to induction ϕ_i. By using the Newton-Raphson iteration method, a solution for the induced angle due to induction is found such that the loading generated by the blade elements is equal to the momentum increase of the streamtube. The Newton Raphson iteration method used to find the angle due to induction is defined as follows:

$$\phi_{i+1} = \phi_i - \frac{f_{\phi_i}}{f'_{\phi_i}} \tag{5.12}$$

in which:

$$f(\phi_i) = C_L\sigma - \frac{4\sin(\phi_0+\phi_i)\tan(\phi_i)}{1-(C_d/C_l)\tan(\phi_i)} = 0 \tag{5.13}$$

This is an iterative method to find the converged solution in a computationally cheap manner. In this iterative method, the lift and drag coefficient C_l and C_d are obtained using the RFOIL results. The Reynolds number calculated according to equation 5.5 was used to obtain the corresponding lift and drag coefficient in the database. Additionally, in each iteration the angle of attack α is calculated using the updated induced angle ϕ_i:

$$\alpha_i = \beta_r - \phi_i - \phi_0 \tag{5.14}$$

For the RFOIL results, the angle of attack range varied from -10 to 20 degrees. A viscous analysis of each of the blade elements is performed using a Reynolds number range varied from $0.5{\cdot}10^5$ to $12{\cdot}10^5$, to allow for a wide range in Reynolds numbers. It was decided not to use the viscous solution acceleration option of RFOIL. In the analysis of the blade elements of the propeller, free transition is used, including a critical amplification component of N_{crit} = 0.1. By using a N_{crit} of 0.1, the assumption is made that the propeller operates in large free stream turbulence. As discussed previously, there is no compressibility correction applied in the RFOIL simulations, since these corrections are applied in the BEM-model itself. Additionally, rotational effects are not taken into account.

In this BEM-implementation, an adaptation to the classical BEM-model is made to determine aerodynamic performance results for a propeller including swept blades. This is a correction which is applied to the lift and drag coefficients as obtained by the RFOIL results. This adaptation to the model was proposed by Geng et al.[15], and a number of assumptions/considerations were made to allow this correction to be implemented. For the effect of blade sweep on aerodynamic performance, only the effect of sweep on individual 2D blade elements is considered. For highly swept propeller blades this assumption is questionable, since the formation

of leading edge vortices due to high leading edge sweep can affect the loading of swept back-sections. However, in this optimization study, it is assumed these assumptions are valid due to the strict bounds on the maximum sweep angle which is allowed.

For the correction which is applied to the lift and drag coefficients, simple sweep theory is used[35]. This theory is mainly used to determine the performance characteristics of swept wings on aircraft. However, as will be discussed, the theory will be applicable to propeller blades with a small sweep angle as well. The correction for blade sweep starts with an infinite blade section placed in an oblique position, as shown in figure 5.4.

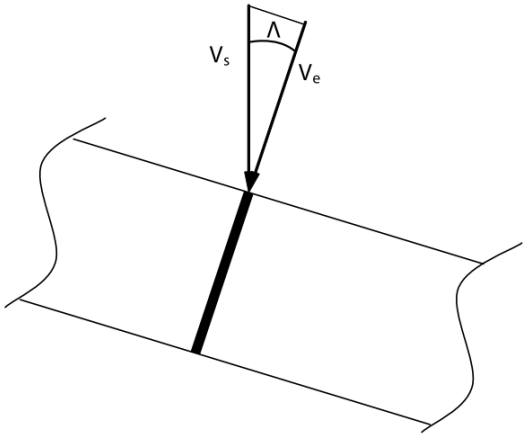

Figure 5.4: Infinitely long blade section placed in an oblique position[35]

In order to determine the effect of blade sweep on the lift and drag coefficient, the relation between the velocity perpendicular to the leading edge and the freestream velocity is considered. The effective velocity component perpendicular to the leading edge V_s and the freestream velocity component V_s are shown in figure 5.4. The angle between these velocity components is the sweep angle Λ. The relation between the freestream-component V_s and V_e is:

$$V_{eff} = V_s \cdot \cos\Lambda \tag{5.15}$$

By using the relation between the freestream component V_s and V_e, the relation between the freestream lift coefficient $C_{l,s}$ and the lift coefficient of the straight blade $C_{l,e}$ can be described. As shown in equation 5.16, a correction factor of $\cos^2(\Lambda)$ is used.

$$C_{l,s} = C_{l,e}\cos^2(\Lambda) \tag{5.16}$$

A different approach is used for the drag coefficient The friction drag and the potential drag are divided in a ratio of 2:1. It is assumed blade sweep does not influence the size of the friction drag. On the other hand, pressure drag is corrected by $\cos^3(\Lambda)$. The $\cos^2(\Lambda)$ is similar to the term to which the lift coefficient is corrected. The drag coefficient is corrected by $\cos^2(\Lambda)$, which is caused by a correction of the drag-vector itself. This yields the following equation for the drag coefficient:

$$C_{d,s} = \frac{2}{3}C_{d,e} + \frac{1}{3}C_d\cos^3(\Lambda) \tag{5.17}$$

The assumption of considering the blade section as infinite only holds for blades with a small chord-to-radius ratio and small sweep angles. For a large chord-to-radius ratio, the flow over the swept blades is influenced by the root- and tip-effect of the blade. Additionally, for large sweep angles, the validity of the theory can be called into question as 3D-effects become more significant. As a result, the assumption that there is no radial interaction between streamtubes might lose its validity, since the displacement of the bound vortex line causes an induction of different blade sections on one another. For high leading-edge sweep angles a leading edge vortex might even be generated, which can have a significant influence on propeller performance[36]. Therefore, only small sweep angles are considered in the optimization study.

Next to the blade sweep correction, the Karman-Tsien compressibility correction is applied to both the lift and drag coefficient in the iteration according to equation 5.18.

$$C_p = \frac{C_{p,0}}{\sqrt{1-M^2} + \left[M^2/\left(1+\sqrt{1-M^2}\right)\right] C_{p,0}/2} \tag{5.18}$$

When the solution is converged, the resulting induction angle is used to calculate the axial- and tangential induction factors a_a and a_t. These are determined using equation 5.19 for the axial induction factor a_a and equation 5.20 for the tangential induction factor a_t.

$$a_a = \frac{\tan\phi(1+\tan\phi_0\tan(\phi+\gamma))}{\tan\phi_0(1+\tan\phi\tan(\phi+\gamma))} - 1 \tag{5.19}$$

$$a_t = a_a \tan(\phi_0)\tan(\phi+\gamma) \tag{5.20}$$

By using equation 5.7 and equation 5.8, the thrust can be determined for each blade element. As discussed previously, Prandtl's tip and root correction factors are applied to the thrust and torque at each radial station. The expressions for Prandtl's tip and root corrections are shown in equation 5.21 and equation 5.22. Prandtl's overall correction factor is shown in equation 5.23.

$$f_{tip} = \frac{N_b}{2}\frac{(1-r)}{R\sin(\phi)} \tag{5.21}$$

$$f_{hub} = \frac{N_b}{2}\frac{(R-r)}{R\sin(\phi)} \tag{5.22}$$

$$f = \frac{2}{\pi}\arccos\left(e^{-f_{hub,tip}}\right) \tag{5.23}$$

Stage 3: Overall propeller performance

The third and last stage of the BEM-implementation is to generate the desired overall propeller performance. When the induction factors of all blade elements are calculated, the key aerodynamic performance indicators of the propeller can be determined. The overall thrust and torque including all radial positions for each of the blades can be determined using the blade element theory and the integral over all blade elements according to:

$$T = \frac{1}{2}\rho V_\infty^2 N_b \int_{r_0}^{R} \frac{f C_L b(1+a)^2}{\sin^2(\phi)\cos(\gamma)}\cos(\phi+\gamma)\,dr \tag{5.24}$$

$$M = \frac{1}{2}\rho V_\infty^2 N_b \int_{r_0}^{R} \frac{f C_L b(1+a)^2}{\sin^2(\phi)\cos(\gamma)} r\sin(\phi+\gamma)\,dr \tag{5.25}$$

The non-dimensional characteristics are obtained according to the equations provided in chapter 2. These equations are repeated here for completeness.

$$C_T = \frac{T}{\rho_\infty n^2 D_p^4} \tag{5.26}$$

$$C_P = \frac{2\pi Q}{\rho_\infty n^2 D_p^5} \tag{5.27}$$

$$\eta = J\frac{C_T}{C_P} \tag{5.28}$$

$$T_C = \frac{T}{\rho_\infty V_\infty^2 D_p^2} \tag{5.29}$$

6

Aeroacoustic Numerical Model

The numerical models used to determine noise emissions of a propeller in the optimization study are discussed in this chapter. Firstly, in section 6.1, prior to the discussion of the numerical model, the justification for the choice of this model is explained. Secondly, the background and implementation of the chosen noise prediction model is discussed in section 6.2. The verification and validation of this model is discussed in chapter 8.

6.1. Aeroacoustic Numerical Model Selection

Similar to aerodynamic performance prediction, various numerical models are available for aeroacoustic performance prediction of propellers. There are multiple criteria that weigh in on the decision for a particular model. Similar to the aerodynamic numerical model selection, the trade-off between accuracy and required computational power is of importance. Additionally, some aeroacoustic methods are limited in their capability to take blade sweep into account, which limits the options for this particular study. As discussed in chapter 2, tonal noise is the dominant contributor to the overall noise level for a propeller. Therefore, only aeroacoustic numerical models calculating tonal propeller noise are considered. Prior to arguing for the selection of an aeroacoustic numerical model, first the fundamental principles and different types of noise prediction methods are briefly discussed.

In the estimation of propeller noise, the propeller blades are modelled as a number of sources and sinks. It is assumed that the sources produce noise, due to the unsteadiness associated with rotation. Most of the propeller noise methods which are used, are derived from the Ffowcs Williams and Hawkings equation [37]. The simplified wave equation is depicted in equation 6.1.

$$\nabla^2 p - \frac{1}{c^2}\frac{\delta^2 p}{\delta t^2} = -\rho_0 \frac{\delta q}{\delta t} + \nabla \bar{F} \tag{6.1}$$

In this equation, the left hand side represents the linear wave operator acting on the acoustic pressure p. The right hand side represents the source terms, which results from the motion of the fluid. The first right hand side term represents the effect of the blades parting the air, therefore producing thickness noise. In the representation of the thickness noise in equation 6.1, the thickness source is a volume distribution of sources of strength q. The other term on the right hand side represents the loading of the blade on the air, therefore producing loading noise. The loading distribution is represented by a volume distribution of doublets associated with the force imposed by the blades on the air. In order to find a solution for equation 6.1, there are two types of methods which can be used: time-domain methods and frequency-domain methods.

Time-domain Methods

Time domain methods are used to solve the wave-equation directly in terms of space-time variables[38, 39]. When using time-domain methods, the wave equation is rewritten in terms of the distance from source point to observer, the Mach number from source to observer, the normal surface velocity at the source and the blade load factor. In order to determine the acoustic pressure at time t, the location of every element of the surface should be determined when the emitted sound wave arrives at the observer. In time-domain methods the

blade geometry can be treated with any desired level of precision, which comes at a cost in terms of required computational power.

Frequency-domain methods

In frequency-domain methods the time-component is eliminated from the wave equation by a Fourier transformation. According to Magliozzi et al.[13], an insignificant amount of precision with respect to the representation of the blade geometry is lost, which is acceptable up to harmonics of a high order[13]. When using a frequency-domain approach in order to determine the far-field acoustic pressure, the need is eliminated for the computation of the retarded blade location and numerical derivatives. As a result, these methods are often more suitable in an optimization framework as they are computationally less demanding [40]. Therefore, in this optimization study only frequency-domain methods are considered.

Method selection

Kotwicz et al.[40] compared results generated by three frequency-domain noise models and results generated by a wind-tunnel test campaign. The three different models and their prediction capabilities are summarized in table 6.1. As shown, Hanson's Helicoidal Surface Theory (HST)-model offers a broad range in acoustic prediction capability.

Table 6.1: Acoustic propeller prediction methods which are capable of predicting tonal noise, based on Kotwicz et al.[40]

	Acoustic prediction capability				
Method name	Forward flight	Sweep	Chordwise noncompactness	Nonaxial flow	Average performance
Gutin[41] & Deming[42]	No	No	No	No	0.01s/iteration
Barry & Magliozzi[43]	Yes	No	Yes	No	
Hanson [27]	Yes	Yes	Yes	Limited	

For each of these numerical models, there was a significant variation in accuracy of the results considering different test cases. These multiple test cases considered included a range of different microphone positions to validate acoustic models. It was shown that there was reasonable agreement between the acoustic models and the experiments. Hanson's model was found to be the most consistent, with an average error of 5.9 dB in perceived sound pressure level relative to experimental data. Although not an insignificant error, for a low-fidelity model this is an acceptable estimate, especially for design and optimization studies. Moreover, acoustic trends are still correctly estimated. Considering the broad range in acoustic prediction capabilities of Hanson's HST-model, such as calculating acoustic performance for blades with sweep and propellers in forward flight, this model is selected as aeroacoustic numerical model used in the optimization study. It is described in detail in section 6.2.

6.2. Propeller Noise Prediction - HST-model Implementation

As previously discussed, Hanson's Helicoidal Surface Theory is a frequency-domain far-field noise prediction method[27]. In this theory, the assumption is made that the thickness and loading noise sources act on the advancing helicoidal surfaces swept by the propeller blades. These propeller blades are represented by radial lines rotating at an angular velocity Ω and translating at a freestream velocity V_∞. The loading and thickness sources are calculated separately and are then transferred to the radiation equation, after which the acoustic pressure is determined. Additionally, in this model implementation, non-linear effects due to Mach numbers larger than 1 are assumed to be negligible. This is a valid assumption for the operating conditions which are considered in the optimization study, since low speed conditions are examined. The maximum Mach number is approximately M = 0.7. Therefore, quadrupole noise sources which exist due to non-linear effects are not considered in this implementation. The far-field acoustic pressure is found by using the free-space Green's function in the form of an inverse Fourier transformation[19], equation 6.2. According to Hanson, the far-field is defined as the distance larger than one diameter from the propeller.

$$p(t) = 2Re \sum_{m=1}^{\infty} P_{mB} \exp\left(-imB\Omega t\right) \tag{6.2}$$

The term P_{mB} is the Fourier coefficient of the transformed time history of the pressure at the m^{th} harmonic of the blade-passage frequency for a propeller with B blades. This term can be written as the sum of the effects of thickness (Volume,V) and loading (drag,D and lift,L):

$$P_{mB} = P_{Vm} + P_{Dm} + P_{Lm} \tag{6.3}$$

The sum of the effects of thickness and loading depends on the noise sources due to thickness and loading. The strength of the thickness and loading sources are determined using the parametrised blade geometry. This blade geometry is defined according to figure 4.3 in chapter 4. Important parameters of the blade geometry for the noise calculations are the chord-to-diameter ratio B_D, the maximum thickness-to-chord ratio t_b, the normalised radial location z and the MCA-to-diameter ratio. The sources are assumed to act on the mean surface of the blade. Therefore, the thin blade assumption is made, which permits the surface boundary conditions to be satisfied on a mean surface rather than on the blade upper and lower surfaces.

To be able to compute the strength of the noise sources, it is necessary to know the chordwise thickness distribution and the chordwise loading distribution at each considered blade element along the radius of the blade. These chordwise distributions are used to include noncompactness effects, which is the interference at observer location of signals emitted at various locations along the chord. The relevance of noncompactness depends on the ratio of chord length to the wavelength of the considered sound wave component. The thickness distribution is defined to be unity at the maximum thickness point, i.e. the maximum thickness point of the thickness distribution is 1. An example of the thickness shape function is shown in figure 6.1. For this thickness distribution, the chord is represented by the normalised chord X, which ranges from -0.5 to 0.5.

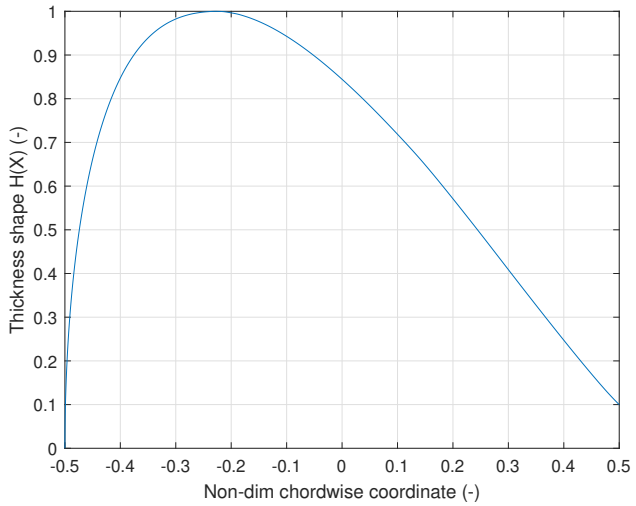

Figure 6.1: Example thickness shape function, derived from an XPROP blade element at r/R = 0.34

Similar to the thickness shape function, the shape function of lift $f_L(X)$ and drag $f_D(X)$ also needs to be known for each blade element. These shape functions are normalised such that each function integrates to unity, i.e. the area under the curve equals 1. An example lift distribution of a blade element of the XPROP-propeller is shown in figure 6.2. The shape functions of loading are generated using RFOIL. At each radial station, pressure distributions are generated for an angle of attack range of [-20:20] and a Reynolds-number range of $[0.5 \cdot 10^5 : 8 \cdot 10^5]$, and the distributions are subsequently stored in a database. By using the known angle of attack from the performed BEM-analysis and the calculated Reynolds number, the corresponding C_p-distribution can be extracted from the database. The pressure distribution is directly used to determine the lift and drag shape functions using the angle of attack from the BEM-analysis. Therefore, an assumption is made that shear stress contributions can be neglected.

The chordwise thickness and loading distribution shape functions are defined in their Fourier source transforms (equation 6.4), which are used in the noise calculations.

$$\begin{Bmatrix} \Psi_V(k_x) \\ \Psi_D(k_x) \\ \Psi_L(k_x) \end{Bmatrix} = \int_{-\frac{1}{2}}^{\frac{1}{2}} \begin{Bmatrix} H(x) \\ f_D(x) \\ f_L(x) \end{Bmatrix} \exp(ik_x x) dz \tag{6.4}$$

With the definitions of the noise sources specified in equation 6.4, according to Hanson[27], the noise harmonics for the far-field noise prediction can be determined using equation 6.5.

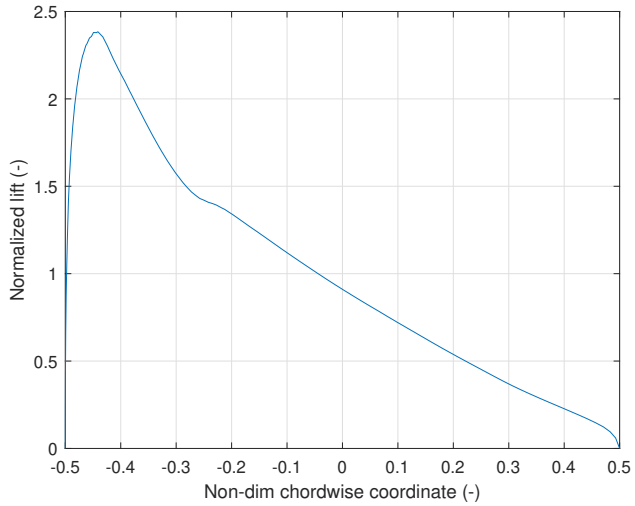

Figure 6.2: Example lift distribution function, derived from an XPROP blade element at r/R = 0.34

$$\begin{Bmatrix} P_{Vm} \\ P_{Dm} \\ P_{Lm} \end{Bmatrix} = -\frac{\rho_0 c_0^2 B \sin(\theta) \exp\left[imB(\frac{\Omega r}{c_0} - \frac{\pi}{2})\right]}{8\pi(y/D_p)(1 - M_x \cos(\theta))} \\ x \int_0^1 M_r^2 e^{i(\phi_s + \phi_o)} J_{mB}\left(\frac{mBzM_t \sin(\theta)}{1 - M_x \cos(\theta)}\right) \begin{Bmatrix} k_x^2 t_b \Psi_V(k_x) \\ ik_x(C_D/2)\Psi_D(k_x) \\ ik_y(C_L/2)\Psi_L(k_x) \end{Bmatrix} dz \tag{6.5}$$

where:

ρ_0 = free-stream density
c_0 = ambient speed of sound
B = number of blades
θ = retarded radiation angle from propeller axis to observer point
m = harmonic of blade passing frequency
Ω = angular speed propeller
r = radial coordinate
y = observer distance from propeller axis
D_p = propeller diameter
M_x = free stream Mach number
M_r = sectional relative Mach number
M_t = tip Mach number
ϕ_s = phase delay contribution due to sweep
ϕ_o = phase delay contribution due to lean
J_{mB} = bessel's function of order mB
k_x = chordwise noncompactness parameter
k_y = thickness noncompactness parameter
C_L = sectional lift coefficient
C_D = sectional drag coefficient
t_b = sectional maximum thickness to chord ratio
z = radial coordinate

In equation 6.5, the noise harmonics are given as a function of the propeller geometry and operating conditions. Next to the ambient density and speed of sound, these operating conditions are also defined by the Mach number along the blades. The Mach number at a radial position z along the blade is defined by the free-stream Mach number and the tip Mach number according to equation 6.6.

$$M_r^2 = M_x^2 + z^2 M_t^2 \tag{6.6}$$

The observer point with respect to the aircraft is defined with respect to the retarded position of the aircraft, not by the visual position. The retarded position is defined by the observer location with respect to the propeller axis and the retarded radiation angle from propeller to observer point. The retarded angle from propeller to observer point is related to the visual angle by the following equation:

$$\cos\theta = \cos\theta_1 \sqrt{1 - M_x^2 \sin^2\theta_1} + M_x \sin^2\theta_1 \tag{6.7}$$

The non-dimensional chord-wise wave numbers k_x and k_y are defined by equations 6.8 and 6.9. The function k_x can be considered as the chordwise noncompactness parameter. A high value of this function, due to a large chord, can lead to significant chordwise interference of sound-waves. This is interference at the observer location due to signals emitted from various chordwise locations of the blade.

$$k_x = \frac{2mBB_D M_t}{M_r(1 - M_x \cos(\theta))} \tag{6.8}$$

$$k_y = \frac{2mBB_D}{zM_r}\left(\frac{M_x - M_r^2 \cos(\theta)}{1 - M_x \cos(\theta)}\right) \tag{6.9}$$

The phase lag ϕ_s due to blade sweep is defined according to equation 6.10. An additional phase shift which can be considered is a phase shift due to displacement normal to the planform ϕ_o, called face alignment or offset. However, this is usually a minor contributor to the overall phase shift. Therefore, the application of face alignment is not considered in this thesis, and will be set equal to 0.

$$\phi_s = \frac{2mBM_t}{M_r(1 - M_x \cos(\theta))} \frac{MCA}{D_p} \tag{6.10}$$

In equation 6.5, J_{mB} is defined as Bessel's function of order mB and argument x. This function characterises the radiation efficiency of the sound-waves. If the argument is equal to the order, Bessel's function reaches a maximum, after which it oscillates. As shown in equation 6.11, the order of Bessel's equation depends on $\sin(\theta)$, which causes noise to diminish towards the propeller front and rear axis, thus representing the noise generating mechanism of a propeller.

$$J_{mB} = J_{mB}\left(\frac{mBzM_t \sin(\theta)}{1 - M_x \cos(\theta)}\right) \tag{6.11}$$

When the factors are known which are needed for the Fourier transformation of acoustic pressure at all harmonics, the formulation for the acoustic pressure (equation 6.2) is solved. Subsequently, the acoustic pressure can be used to obtain the key performance indicators for propeller noise emissions: the root mean squared form of the acoustic pressure (p_{rms}), the sound pressure level (SPL) and the thrust specific sound pressure (TSSP). These key performance indicators are discussed in chapter 2.

A flowchart of the model implementation is depicted in figure 6.3. The model is implemented in MATLAB. For the implementation of the HST-model in the optimization study, the maximum number of harmonics considered is 3. It was found that higher harmonics were negligible compared to the dominant contributions of the first and second harmonics to the overall noise emissions. An elaboration of the maximum number of harmonics is provided in chapter 8.

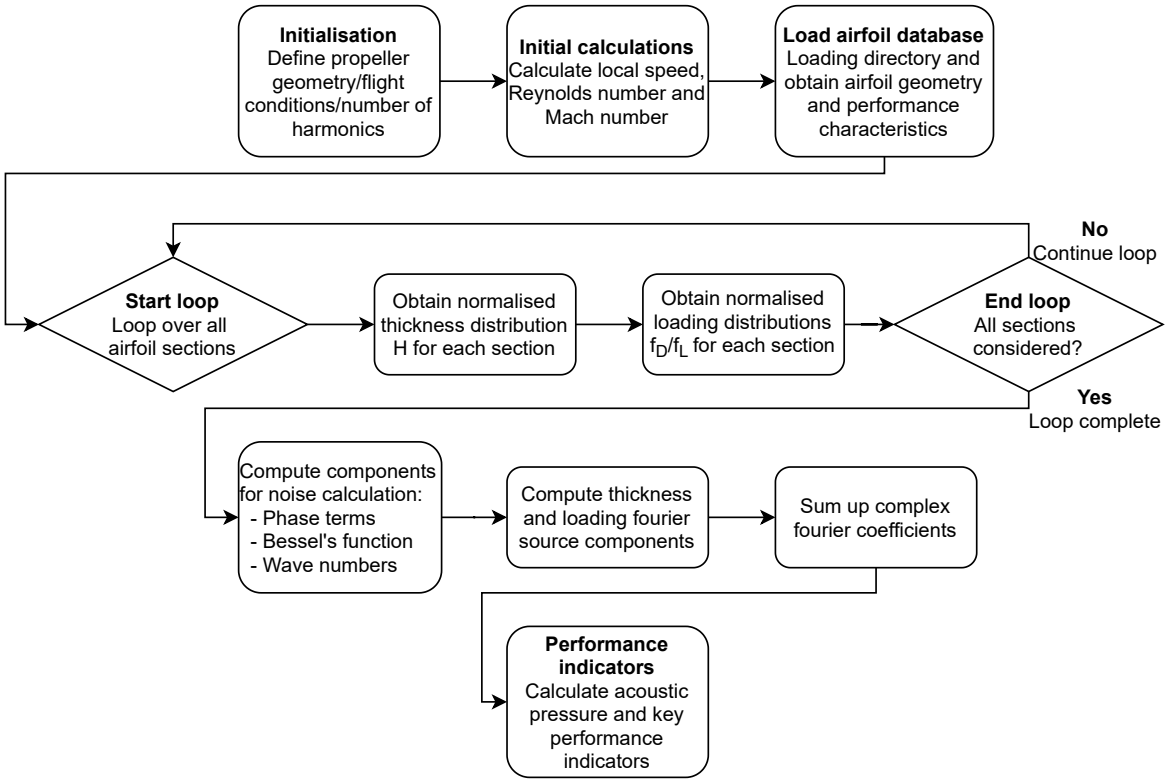

Figure 6.3: Flowchart of HST-noise model implementation

7

Propeller Optimization Setup

In this chapter the setup of the optimization study is outlined. The inputs described in this chapter are of major influence to the results of the optimization study. First, in section 7.1, the baseline propeller is discussed. The geometrical properties of this propeller are used throughout the optimization study. Secondly, the optimization problem is defined in section 7.2. In this section, key aspects including the objective function, design variables, bounds on design variables, constraints and the optimization algorithm are explained.

7.1. Baseline Propeller

The choice of baseline propeller used as input for an optimization study is of significant importance to the result of an optimization. The propeller which is used as a baseline in this optimization study is called the TUD-XPROP, referred to as XPROP(figure 7.1). For this particular propeller, CFD- and experimental data are available, which allows for validation and verification of the numerical models which are used and therefore the optimization results can be assessed with confidence.

Figure 7.1: Picture of TUD-XPROP propeller[44]

The diameter of the XPROP is 0.4064 meter and the amount of blades is equal to 6, which is relatively a relatively high number. The choice for this high number was made since the influence of mid-chord alignment on aeroacoustic performance is more pronounced for higher blade counts[14]. For numerical analysis, the blades are divided in to 25 uniformly distributed cross section across the blade. Each of these cross sectional shapes of the XPROP-blades are shown in appendix A. The radial distributions of twist and chord for a single blade of the XPROP are shown in figure 7.2. Since no blade sweep is applied in the design of the XPROP, it can be classified as a propeller including straight blades.

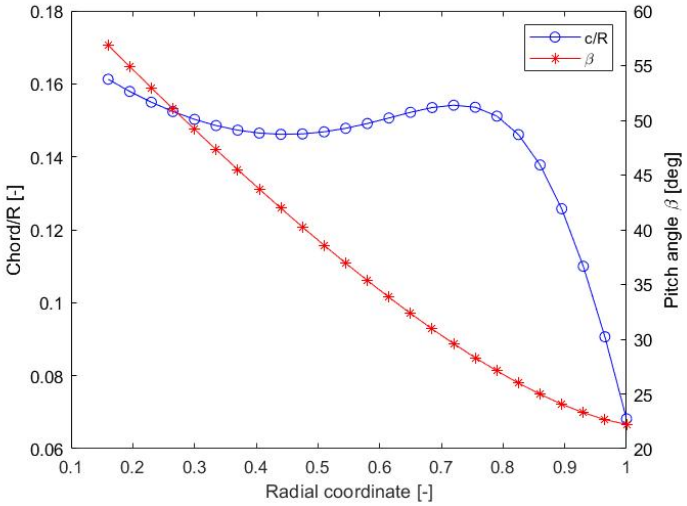

Figure 7.2: Radial distribution of pitch and chord of the XPROP blades

7.2. Definition of Optimization Problem

A successful optimization study depends on the definition of the optimization problem. In the optimization problem, the objective function, the design variables and the constraints are specified. This optimization problem is solved in the following manner. An optimization algorithm changes the value of the design variables to increase the performance of the objective to eventually arrive at maximum performance. During the optimization process, the design variables are subjected to a set of bounds and constraints to limit the design space. Before going into details of the individual components of the optimization problem, first the overall optimization architecture is presented in figure 7.3.

The initial design variables mark the start of the optimization process. These initial design variables are used as an input for the optimization. Subsequently, in the first iteration of the optimization routine, calculations are made of the initial key performance indicators of the performance models, the value of the objective function and the value of the constraint. Based on these findings, the optimization algorithm changes the design variables such that a lower objective function value or a lower constraint violation is obtained. If there is no constraint violation and the smallest change in design vector does not lead to a decrease of the objective function, the optimization is terminated and an optimum point is found.

7.2.1. Objective Function

The optimization algorithm aims to minimize the objective function, which makes this a critical element of the optimization study. As discussed previously, there are two objectives in the optimization study: maximizing aerodynamic performance and minimizing noise emissions. For this optimization study, the decision has been made to use one objective function due to its simplicity. The performance indicators defining aeroacoustic and aerodynamic performance are combined in this objective function.

As discussed in section 2.2, there are multiple performance indicators which can be used to represent propeller noise. However, for a fair comparison between different propeller geometries, it is chosen to consider a performance indicator whereby the sound pressure is related to the pressure jump over the propeller disk (T/D^2). This performance indicator is called the Thrust Specific Sound Pressure (TSSP), defined by equation 7.1. In addition, the propeller efficiency is the performance indicator for aeroacoustic performance, defined by equation 7.2.

$$TSSP = 20\log_{10}\left(p_{rms} \cdot \frac{D_p^2}{T}\right) \tag{7.1}$$

$$\eta_p = J\frac{C_T}{C_P} \tag{7.2}$$

Since propeller noise is emitted along the entire directivity range, using only a single thrust specific sound pressure at a specific directivity angle yields a limited representation of the noise emissions along the entire

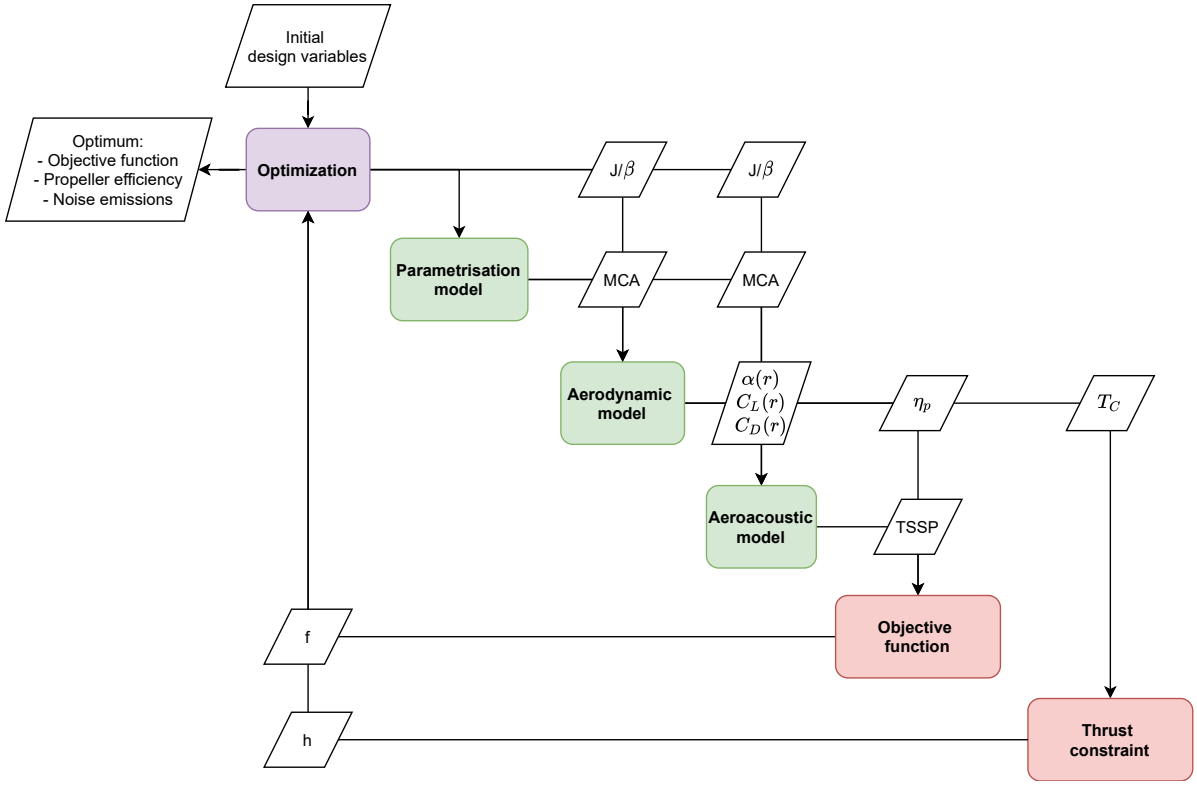

Figure 7.3: Architecture of the optimization process

directivity range. Therefore, three points along a sideline at a distance of 10 propeller radii parallel to the propeller axis are taken at directivity angles of 60°, 90° and 120°, represented in figure 7.4. An illustration defining the propeller with respect to the directivity pattern and the freestream flow is provided in figure 7.5. Three points are considered, which ensures a computationally cheap process despite the various points along the directivity range. The average of the three points is used as a key performance indicator, which is calculated according to equation 7.3. In this equation, the average TSSP is calculated by using a linear sum, which is chosen since this may help to avoid a bias towards the point of maximum noise emissions. In this way, it forces the optimizer to reduce noise along the entire sideline.

$$TSSP_{mean} = \frac{\sum TSSP_{\theta=60°,90°,120°}}{3} \tag{7.3}$$

For an optimization in which both of the objectives are included in the optimization study, two different approaches are considered:

1. The relative importance of each objective can be changed by considering one objective, while the other objective is subjected to an inequality constraint. The objective function of and aeroacoustic performance is shown in equation 7.4. The variable $TSSP_0$ is included to normalise the aeroacoustic performance indicator, which causes the optimization to start at a value of 1. In this thesis, the propeller efficiency is constrained to a minimum value, while the design variables are optimized for noise emissions. The value of the minimum accepted propeller efficiency states the size of the design space and as such, it describes the amount of noise reduction which can be attained with respect to the design for maximum propeller efficiency. As an example: if the minimum allowed propeller efficiency is similar to the propeller efficiency as obtained for maximum aerodynamic design, the design space is highly constrained and an optimization will not yield a noise reduction. However, if the minimum accepted propeller efficiency is decreased, the design space for aeroacoustic optimization grows. As a result, this allows for design variables with higher aeroacoustic performance. By constantly decreasing this minimum value for propeller efficiency, a trade-off plot between aerodynamic and aeroacoustic performance can be obtained.

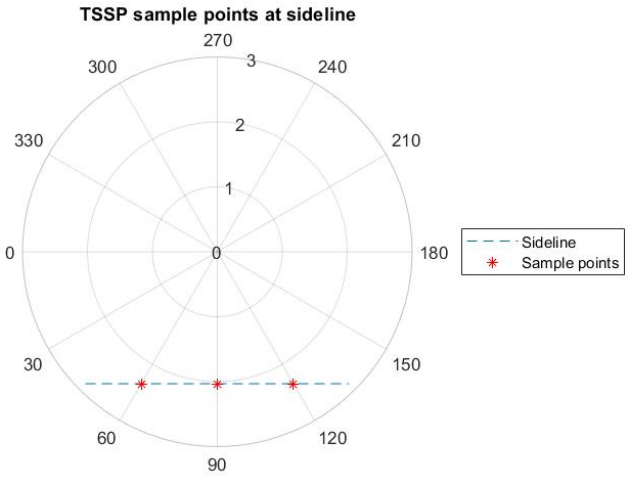

Figure 7.4: Sample points taken at a sideline parallel to the propeller axis

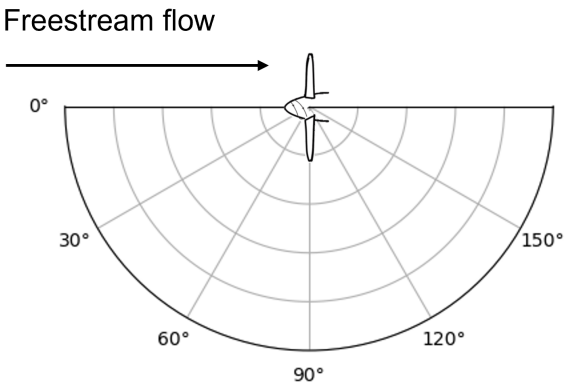

Figure 7.5: Illustration of directivity pattern with respect to the freestream flow including propeller at the origin.

$$f = \frac{TSSP_{0,mean}}{TSSP_{mean}} \tag{7.4}$$

2. The relative importance of each objective, aeroacoustic or aerodynamic performance, can be changed by changing a weighting variable k. This weighting variable states the amount of importance of each objective in a single objective function which includes both aerodynamic and aeroacoustic performance indicators. The corresponding objective function is shown in equation 7.5. The variable k can be varied from 0 to 1 to obtain a trade-off plot between aeroacoustic and aerodynamic performance. A weighting factor of 0 represents optimizing only for high aeroacoustic performance, while a weighting factor of 1 represents optimizing solely for high aerodynamic performance. This means, for a value between 0 and 1, both the aerodynamic and aeroacoustic objectives are taken into account. In addition, the initial propeller efficiency η_0 and the initial noise emissions $TSSP_0$ are included, which normalises the aerodynamic and aeroacoustic performance indicators. As a result, the optimization to start at a value of 1.

$$f = k\left(2 - \frac{\eta_p}{\eta_{p0}}\right) + (1-k)\frac{TSSP_{0,mean}}{TSSP_{mean}} \tag{7.5}$$

where:

$$0 \leq k \leq 1$$

7.2.2. Constraints

In order to ensure a proper comparison between different propeller designs, constraints on the optimization process are used. For each of the optimizations which are performed, the thrust-coefficient-constraint is always active (equation 7.6). This is an equality constraint, which means the thrust coefficient T_C of the optimized design variables must be equal to a predefined design thrust coefficient $T_{C,des}$. By using this equality constraint, a fixed amount of thrust must always be generated by the propeller, which ensures a fair comparison between different design vectors and propeller designs. The thrust coefficient $T_C = T/\rho_\infty V_\infty^2 D_p^2$ is a function of the overall propeller thrust and the dynamic pressure due to the freestream. Since the dynamic pressure due to the freestream is a fixed quantity, the only variable which is affected is the overall propeller thrust.

$$\frac{T_C}{T_{C,des}} = 1 \tag{7.6}$$

Changing the mid-chord alignment only will change the thrust of the propeller. Therefore, a change in the mid-chord alignment must be compensated by the operational variables. One could argue that another possibility is to use an alternative definition of the thrust coefficient C_T (equation 2.2), in which the thrust is non-dimensionalized by the dynamic pressure associated with the tip speed of the propeller. However, the use of this definition is not desirable, since thrust with respect to the free stream dynamic pressure is desired. If the thrust coefficient C_T is fixed, then the advance ratio can change the thrust itself, which is not desired for a fair comparison between different design vectors.

An additional constraint is used when the first optimization approach is considered. As discussed, if the objective function solely consists of the thrust specific noise, a constraint is used which states that the optimization is limited by a minimum allowed propeller efficiency, shown in equation 7.7. The use of this constraint is based on the expectation that optimization for aeroacoustic performance is at the expense of aerodynamic performance.

$$\frac{\eta_{min}}{\eta} \leq 1 \tag{7.7}$$

7.2.3. Design Variables

The design variable which is of most interest in this study is the mid-chord alignment (MCA), since a proper use of this design variable has the potential to reduce propeller noise emissions. As baseline design variables, the advance ratio J and the collective pitch angle β of the blades are used. This allows for an insight in the behaviour of these operational variables when the optimization is conducted for different objectives. The results of the baseline optimization forms a basis for the addition of the assessment of blade sweep on noise reduction. The design vector for the baseline optimization is defined according to equation 7.8. The initial design vector consists of initial design variables J = 1.1 and β = 30°.

$$\overline{x} = \begin{bmatrix} J[-] \\ \beta[rad] \end{bmatrix} \tag{7.8}$$

The addition of MCA to the design vector add multiple design variables to the optimization. As discussed in chapter 4, the mid-chord alignment along the radius is a distribution which is parametrised by using Bézier curves. An indication of the location of the control points which define the Bézier curve as being used in the optimization for blade sweep is shown in figure 7.6. The Bézier curve are defined such that $0 \leq x \leq 1$ and $0 \leq y \leq 1$. The y-coordinate of the Bézier curve is scaled to the lower and upper bounds of the non-dimensional radial coordinate. The x-coordinate of the Bézier curve is scaled to the lower and upper bounds of the MCA-distribution defined by the optimization setup.

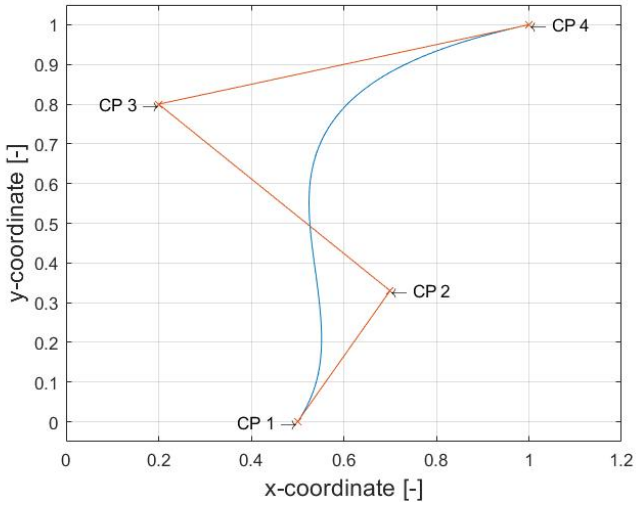

Figure 7.6: Indication of the locations of the control points which define the Bézier curves.

In the optimization, the control points are allowed to be moved in x- and y-direction. However, the first control point is not allowed to be moved, because the blade is fixed at the root. Additionally, control point number four is located at the tip of the blade, which is not allowed to be moved in radial direction. As a result, there are a total of 5 design variables which represent the MCA-distribution and makes the definition of the design vector according to equation 7.9. The initial design vector consists of initial design variables J = 1.1 and β = 30°and control points which establish a straight blade: y_{CP_2} = 0.4, y_{CP_3} = 0.7, x_{CP_2} = 0.5, x_{CP_3} = 0.5 and x_{CP_4} = 0.5.

$$\overline{x} = \begin{bmatrix} J[-] \\ \beta[rad] \\ y_{CP_2}[-] \\ y_{CP_3}[-] \\ x_{CP_2}[-] \\ x_{CP_3}[-] \\ x_{CP_4}[-] \end{bmatrix} \tag{7.9}$$

The comparison between the optimization of advance ratio and collective blade pitch and the optimization of advance ratio, collective blade pitch and MCA-distribution gives an insight into the effect of MCA-distribution on both propeller aerodynamic and aeroacoustic performance.

7.2.4. Bounds on Design Variables

For each of the design variables mentioned in section 7.2.3, upper and a lower bound are defined, which are tabulated in table 7.1. As shown, the bounds on the operational design variables, the advance ratio J and the collective pitch β, are predefined such that there is a large design space. These bounds are in most cases not relevant, since the operational variables are generally dictated by the thrust coefficient T_C as there should be an adequate pitch setting and advance ratio in order to achieve the required thrust level.

Table 7.1: Upper and lower bounds of operational design variables used in the optimization

Parameters	Lower bound	Upper bound
J[-]	0.4	4
β[deg]	10	85

The bounds on the control points defining the MCA-distribution require a more in-depth elaboration. As the MCA distribution is the variable of interest for this study, the bounds on this particular variable can be of major influence on the results. The bounds on the design variables should be set in such a way that the optimized design can be manufactured and it is structurally feasible. Including manufacturability and structural feasibility into two single values for the upper and the lower bound of the MCA-distribution is a challenge. The manufacturability of the design depends on the manufacturer itself, while the structural feasibility would require a structural analysis module in the optimization. Including a structural analysis module in the optimization process is out of the scope of this thesis. Therefore, the values for the upper and lower bound of the control points defining the MCA-distribution are an estimation. Based on previous research by others[9, 15], the bounds on the control points are established as follows:

- There is no mid-chord alignment at the root. Therefore, there is a control point on the location of the root, which is not a design variable: CP_1 is fixed.
- An overall backward sweep should exist, which means the mid-chord alignment at the tip should be positive: $x_{CP_4} > 0$.
- The value of the mid-chord alignment, positive and negative, is not allowed to be higher than the maximum chord of the blade: $X_{CP} < c_{max}$. These limits are shown in figure 7.7.
- The final control point is positioned at the radial location of the tip: $y_{CP_4} = 1$.

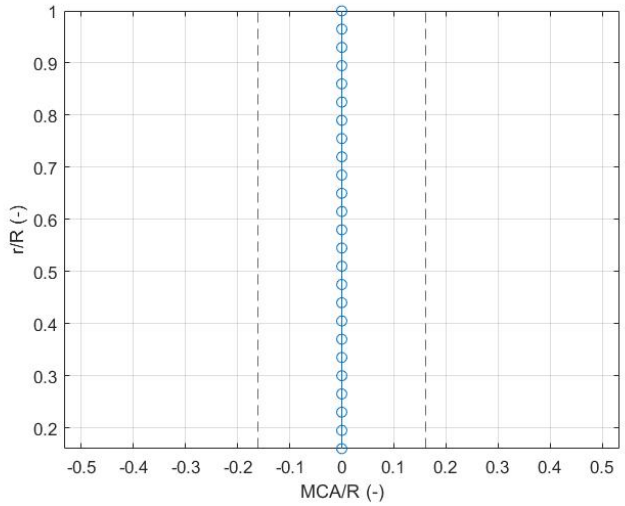

Figure 7.7: Illustration of the bound on the mid-chord alignment design variables

7.2.5. Optimization Algorithm

The selected optimization method should be capable of solving an optimization problem which is classified as single-objective, multivariable, nonlinear and constrained. The optimization method which is used is the "FMINCON"-function by MATLAB©. This is an off-the-shelf, gradient-based optimization method. For the fmincon-function, there are a number of algorithms available, which are all algorithms used for constrained nonlinear optimization[45]. The algorithm which is used is the sequential quadratic programming (SQP) method, described in detail by Nocedal et al.[46]. This method was selected because it can handle the highly nonlinear character of the optimization problem and the algorithm can recover from NaN or Inf results.

In the SQP-method, the constrained nonlinear optimization problem is transformed into an easier sub-problem, which is solved and used as a basis of a new iteration. An important part is the design of this quadratic subproblem. For a nonlinear optimization including inequality constraints, the aim is to solve the Karush–Kuhn–Tucker equations, which are necessary conditions to satisfy the active constraints. The KKT equations are necessary and sufficient for a global solution point if the objective function and the constraint function are convex functions.

7.2.6. Optimization Problem

The previously discussed components of optimization lead to a final definition of the optimization problem. For the approach in which the propeller efficiency is used as a constraint and the mean TSSP defines the objective function, the optimization problem is defined as follows:

$$\min_{x} \quad \frac{TSSP_{0,mean}(x)}{TSSP_{mean}(x)} \tag{7.10a}$$

$$\text{subject to} \quad T_C = T_{C,des}, \tag{7.10b}$$

$$\eta_p \geq \eta_{p,min} \tag{7.10c}$$

For the approach in which a weighting variable k is used in the objective function to define the amount of importance for each objective, the optimization problem is defined as:

$$\min_{x} \quad k\left(2 - \frac{\eta_p}{\eta_{p0}}\right) + (1-k)\frac{TSSP_{0,mean}}{TSSP_{mean}} \tag{7.11a}$$

$$\text{subject to} \quad T_C = T_{C,des}, \tag{7.11b}$$

$$0 \leq k \leq 1 \tag{7.11c}$$

III

Model Validation & Results

8

Model Validation & Verification

In order to build confidence in the aerodynamic and aeroacoustic models, a verification- and validation routine is performed. Firstly, in section 8.1, parametrisation errors and the influence of parametrisation on aerodynamic and aeroacoustic results are investigated. Secondly, in section 8.2, the BEM-model implementation discussed in chapter 5 is verified by means of experimental and CFD results of a swept-bladed propeller. Finally, in section 8.3, the HST-model implementation is verified by means of a qualitative comparison. With these validation and verification steps, the optimization results in chapter 9 can be used to draw conclusions of this study.

8.1. Geometry Parametrisation Verification

In this section, an estimation is made of the errors induced by the parametrisation process of the propeller blades. The purpose of this section is to assess how well the parametrisation of the numerical model represents the actual geometry of the propeller blades. As discussed in chapter 4, Bézier curves are generated by using a number of control points. The amount of control points for each parameter is a compromise between low computational times and low parametrisation errors. These errors and the effect of these errors on aerodynamic and aeroacoustic results are treated in section 8.1.1 and section 8.1.2 respectively, where geometry verification is done by using the geometry of the XPROP-propeller.

8.1.1. Geometry Parametrisation Errors

By using an optimization scheme, the control points are positioned such that the parametrised curve of a specific radial distribution represents the actual blade geometric radial distribution. For the XPROP, there are 25 radial positions along the radius for which the chord, twist and sweep are specified. At these 25 radial stations, the chord, twist and sweep values are computed of both the Bézier curve representation and the actual geometry. Least squares is used in the optimization routine to quantify the error between the values generated by the Bézier curve representation and the actual propeller geometry. For the Bézier curve representation, the twist and chord distribution of the XPROP are used. Although the twist and chord are not optimized in this thesis, these parameters can be used to verify the Bézier curve representation.

In figure 8.1 the chord distribution of the XPROP is shown as well as the Bézier curve representation using a set of control points. As shown, there is a small difference between the parametrised chord and the original XPROP chord, which is more clearly illustrated using figure 8.2. The error between the parametrised curve and the actual blade chord shows an oscillatory behaviour with a maximum error of approximately 2×10^{-6}. This maximum error in non-dimensional chord is acceptable, since this corresponds to a maximum difference in chord of 0.0001 mm. Additionally to the chord distribution parameter, the twist distribution is also used to verify the Bézier curve representation. In figure 8.3 the XPROP twist distribution and the Bézier curve representation are shown. As shown in figure 8.4, the maximum error is approximately 2×10^{-5}, which is a negligibly small error. These combined results indicate that the error in aerodynamic and aeroacoustic results induced by the parametrised Bézier curve with respect to the actual Bézier curve is negligible and thus the Bézier curve can be used with confidence to represent a radial distribution of MCA.

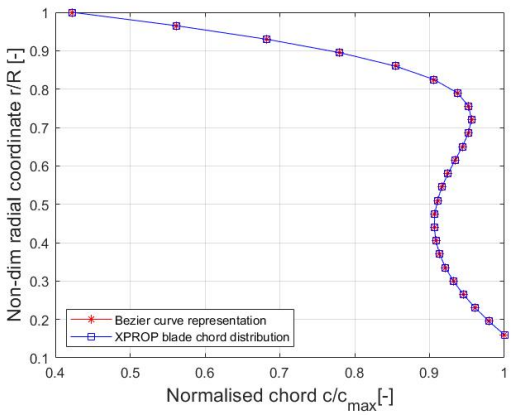

Figure 8.1: Bézier curve parametrisation and XPROP geometry of the chord distribution

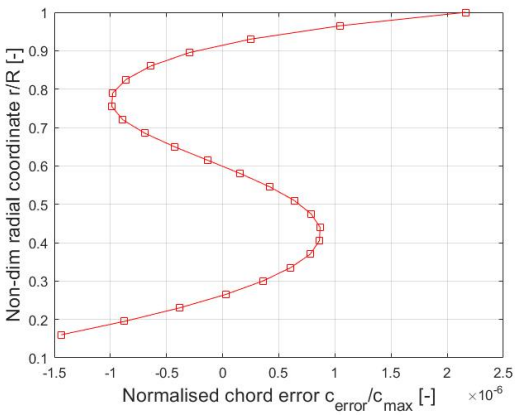

Figure 8.2: Radial error plot showing the difference between the parametrised XPROP and the actual XPROP chord

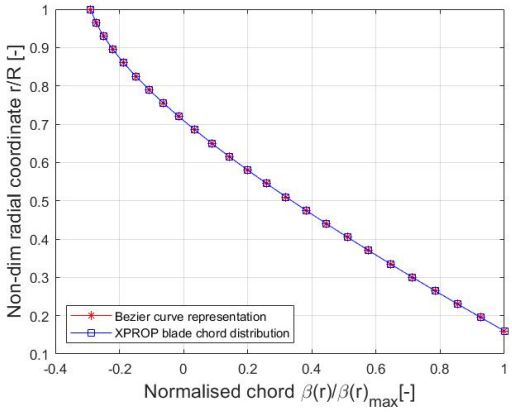

Figure 8.3: Bézier curve parametrisation and XPROP geometry of the twist angle distribution

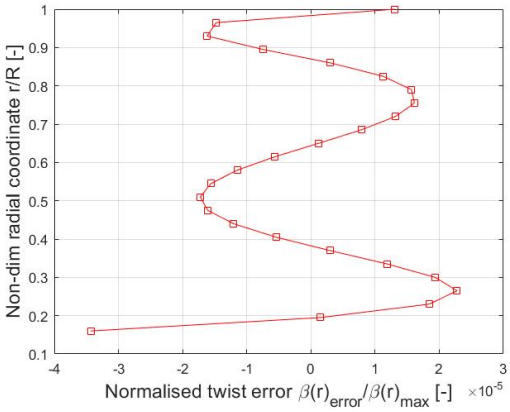

Figure 8.4: Radial error plot showing the difference between the parametrised XPROP and the actual XPROP twist angle

8.1.2. Influence of Parametrisation Errors on Results

In this section, it will be shown that the error induced by parametrisation has a negligible effect on aeroacoustic and aerodynamic results. For the aerodynamic results generated by the BEM-model, the propeller efficiency as a function of the advance ratio is shown in figure 8.5. A maximum error of 2×10^{-3} % was found between the aerodynamic results generated by the actual XPROP geometry and the parametrised blade geometry. For aeroacoustic results generated by the HST-model, the sound pressure level is shown in a directivity plot in figure 8.6. The maximum error between the actual XPROP geometry and the parametrised blade geometry for aeroacoustic results was 1×10^{-5} dB. This shows that the Bézier curve representation is a well performing parametrisation technique which can be used to represent these relatively simple geometrical radial distributions with confidence.

8.2. BEM-model Verification and Validation

Verification is required of the BEM-model implementation including sweep theory by Hu (chapter 5). To verify and validate this model, a BEM-implementation by Gur and Rosen[29], CFD results and wind-tunnel test results are used. First, a straight-bladed propeller, the XPROP, is used to assess the performance of both the BEM-implementation by Hu and by Gur and Rosen for a straight-bladed propeller with 6 blades (subsection 8.2.1). Secondly, a propeller including swept blades is used to quantify the differences in aerodynamic results due to the application of sweep to the blades (subsection 8.2.2). This allows an assessment of the performance of each BEM-implementation calculating aerodynamic results of a propeller containing highly swept blades.

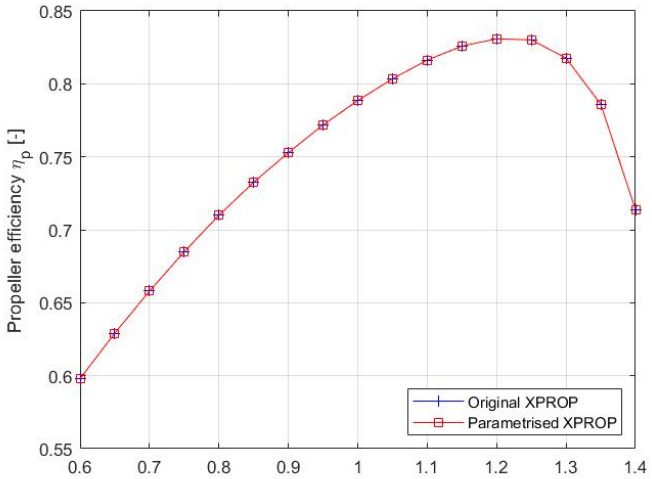

Figure 8.5: Propeller efficiency calculated with the BEM-model as determined from the XPROP-geometry and parametrised XPROP-geometry

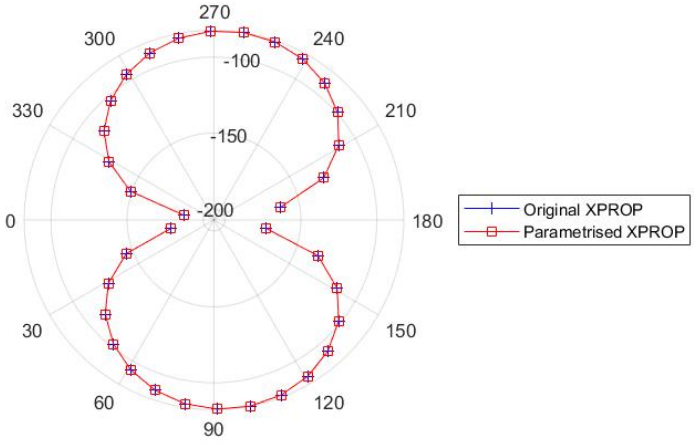

Figure 8.6: TSSP directivity plot calculated with the HST-model as determined from the XPROP-geometry and parametrised XPROP-geometry

8.2.1. Straight-bladed Propeller Verification

As a baseline comparison between the numerical models, the CFD-simulation and the wind-tunnel test, the XPROP propeller is used. This baseline comparison is required, since it allows for an assessment of the accuracy of blade sweep modelling by both the BEM-implementation by Hu and by the BEM-implementation by Gur and Rosen. The XPROP-propeller, which is used to verify the straight-bladed propeller aerodynamic results, is described in detail in section 7.1. The cross-sectional shapes of the XPROP-blades are shown in appendix A. For this verification, a freestream velocity of 30m/s is used, since experimental results are available for freestream velocities of 30 m/s. Ambient conditions are tabulated in table 8.1.

Table 8.1: Ambient conditions used to verify the BEM-model

Property	Value	Unit
T_{amb}	288.15	K
ρ_{amb}	1.225	kg/m^3
V_∞	30	m/s
P_{amb}	101325	Pa

The experimental results are obtained by a wind-tunnel experiment in the Open-Jet facility in 2017 at the TU Delft[47]. These experimental results are shown in figure 8.7 and figure 8.8. The thrust and power coefficient are shown for an advance ratio range between 0.6 and 1.4. A 3rd order polynomial fit is used for both the thrust and power coefficient. These polynomial fits show the small amount of spread in the data. The propeller efficiency is determined by using the polynomial fit of the thrust and power coefficient and the corresponding advance ratio. The polynomial fits which represent the C_T and C_P results generated by the wind-tunnel experiment are subsequently used in the comparison.

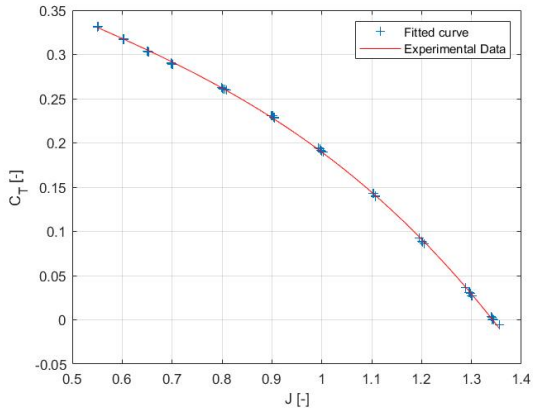

Figure 8.7: Thrust coefficient C_T of the 6-bladed XPROP measured in a wind-tunnel experiment and a 3rd order polynomial fit

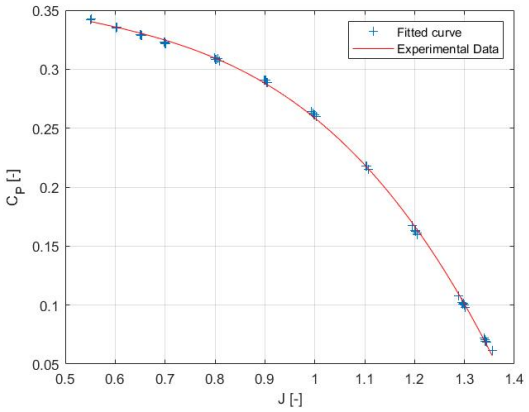

Figure 8.8: Power coefficient C_P of the 6-bladed XPROP measured in a wind-tunnel experiment and a 3rd order polynomial fit

In figure 8.9 and figure 8.10, the comparison in thrust and power coefficient is shown for experimental results and numerical BEM-model results for the XPROP-propeller. Additionally, in figure 8.11, a plot is shown in which the resulting propeller efficiencies are compared. Due to convergence issues, there were no results for advance ratios lower than 0.8 for the Gur and Rosen model. A possible explanation for this lack of data is that the sectional loading coefficients by RFOIL are computed at a high blade loading, at which blade separation starts to occur. This introduces a non-uniform blade loading, which may introduce convergence issues. However, this possible explanation has not been verified. Nevertheless, since the results included the point of maximum efficiency and a reasonable amount of data, the results generated by the Gur and Rosen model were satisfactory for verification of the model used in this thesis.

Some features stand out in the results generated by the numerical models and the wind-tunnel test. As shown in the comparison between propeller efficiency, both BEM-models show the same behaviour. When considering the thrust and power coefficients at a high advance ratio, for example J=1.4, both BEM-implementations show similar results. However, when decreasing the advance ratio, the BEM-model by Hu generates lower thrust and power coefficients compared to the BEM-model by Gur and Rosen. These findings are in line with the findings by Gur and Rosen, who also showed a higher thrust coefficient compared to general momentum theory, due to a difference in modelling to obtain the induced velocities.

By comparing the power coefficient curve generated by the numerical models and the wind-tunnel test, one could argue that the Gur & Rosen model shows a better agreement to the experimental data compared to the Hu-model. For high advance ratios, there is an equal offset between experimental results and numerical simulations by both models. However, at lower advance ratios the gradient of both the thrust and power coefficient as obtained from experimental data shows better agreement with the Gur & Rosen model. Since the propeller efficiency is dependent on the ratio of thrust and power coefficient, the propeller efficiency of both BEM-models closely agree. At lower advance ratios, the difference is slightly larger compared to the higher advance ratio. Based on these results, it would justifiable to select the Gur & Rosen model, if only straight

blades were considered in the optimization study. However, in this optimization study propellers including swept blades are considered. Therefore, selection of numerical model can not only be based on the verification for a propeller including straight blades. In the next section, a propeller including swept blades is used to verify the numerical models.

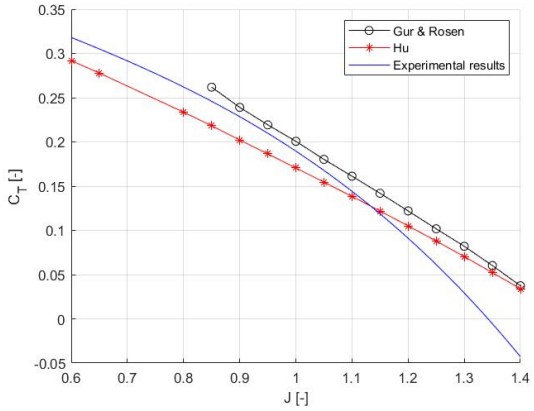

Figure 8.9: Thrust coefficient comparison between experimental results, BEM-Hu model results and BEM-Gur and Rosen model results for the XPROP

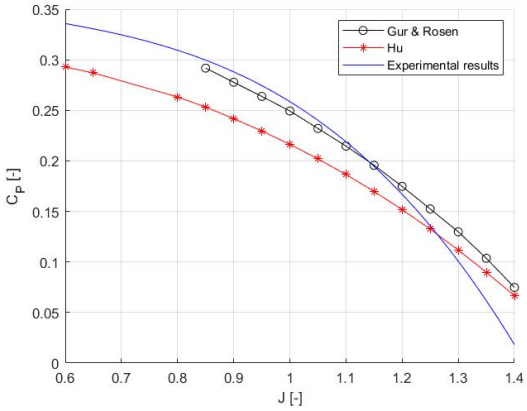

Figure 8.10: Power coefficient comparison between experimental results, BEM-Hu model results and BEM-Gur and Rosen model results for the XPROP

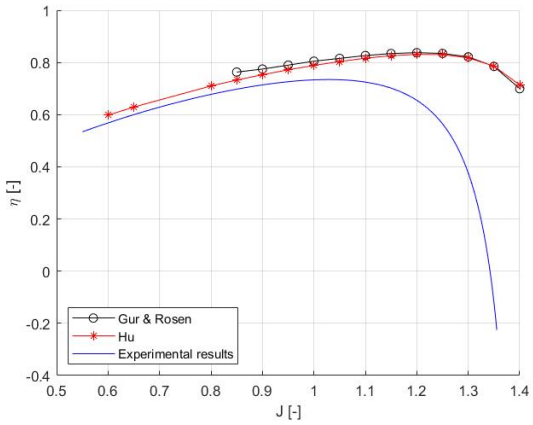

Figure 8.11: Propeller efficiency comparison between experimental results, BEM-Hu model results and BEM-Gur and Rosen model results for the XPROP

However, these models differ significantly from the experimental data. The cause of this discrepancy between experimental data and numerical results is unknown. Possible explanations are errors in the measurement devices or an inaccuracy in the Reynolds number computation for the numerical results. According to Sinnige[12], for Reynolds numbers at 70% of the blade radius lower than 1.5×10^5, the performance is especially sensitive to the Reynolds number for the XPROP. For the numerical results, the assumption of a fully turbulent flow is made in the computation of the sectional data. However, at lower Reynolds numbers which occur during high advance ratios, the flow has the potential to become laminar, which can induce an error in the sectional loading coefficients. Additionally, the BEM-model assumes that there is no radial interaction between different sections. However, during the experiment the occurrence of radial interaction between different sections is is not inconceivable, since the centrifugal force of the rotating propeller forces air particles to higher radial coordinates, while the Coriolis force affects these movements as well. The impact of these interactions still remain to be elucidated.

Since the exact reason for the discrepancy is still unknown, there is a lack of confidence in the experimental data. Therefore, no conclusions can be drawn from the comparison between experimental results and numerical BEM-results. This means, validation cannot be performed for the straight-bladed propeller. However, as discussed in the next section, validation of an equal method was performed for a swept-bladed propeller[15]. Therefore, the result presented in chapter 9 are still believed to be trustworthy.

8.2.2. Swept-bladed Propeller Verification

In order to verify if the BEM-model can be accurately used to determine aerodynamic performance for propellers with (highly) swept blades, the Advanced Propulsion Integration Aerodynamics and Noise project(APIAN) propeller is used as input geometry, since CFD-results and wind-tunnel test results are available for this particular geometry. A picture of the APIAN propeller is depicted in figure 8.12. The APIAN propeller features 6 highly swept blades with a total diameter of 0.508m. At a radial position of r/R = 0.75, the pitch angle was set to 40.4 degrees. Additionally, the cross sectional shapes of the APIAN propeller-blades are shown in appendix A.

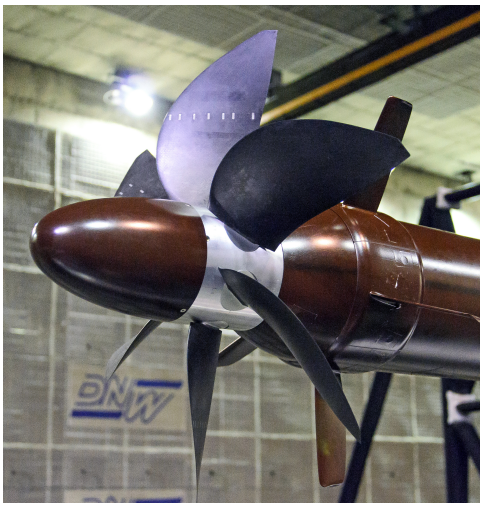

Figure 8.12: Picture of APIAN propeller[44]

The radial distributions of twist, chord and MCA for a single blade of the APIAN propeller are shown in figure 8.13 and 8.14. Comparing the chord-distribution of the APIAN propeller blade with an XPROP-propeller blade, it can be concluded that the shape of the distribution is similar. However, one major difference is that the average chord-to-diameter ratio of the APIAN propeller blade is three times larger compared to that of the XPROP-propeller blade. For this reason, the solidity of the APIAN propeller is significantly larger compared to the XPROP-propeller. In figure 8.14, a forward sweep is present close to the root of the APIAN propeller blade, since a negative MCA is shown. As the radial coordinate increases, the sweep angle starts to increase, which means a backward sweep angle is induced as the tip is approached. At the tip of the blade, there is a maximum sweep angle of about 45 degrees. Therefore, the APIAN propeller blades can be classified as highly swept blades, which makes it useful for verification of the BEM-model including a correction for sweep.

Prior to validation of the BEM-results to experimental and CFD results, an evaluation is performed to assess the different modelling approaches of the effect of sweep in both BEM-implementations. This is an extra verification step which gives an additional insight in blade sweep modelling in BEM-models. The difference in the modelling approaches is assessed by performing simulations for a non-existing APIAN propeller with blades containing zero sweep and for the actual APIAN propeller containing highly swept blades. The results of these simulations are shown in the thrust coefficient plot (figure 8.15) and the power coefficient graph (figure 8.16).

In figure 8.15 and 8.16, a key difference in the sweep modelling methods becomes apparent at high advance ratios. For the Gur and Rosen simulation, the point of zero thrust shifts to a lower advance ratio for the swept-bladed APIAN propeller compared to the unswept-bladed APIAN propeller. The reason for this shift is the approach of modelling blade sweep in the BEM-model. In the model by Gur and Rosen, blade sweep is modelled by using the cross-section of a blade element as defined in the model (figure 8.17). As shown in the blade element, a correction of the local blade sweep is applied to the azimuthal velocity and the tangential/axial induction velocities. The correction for sweep in the Gur and Rosen-implementation is applied to the azimuthal

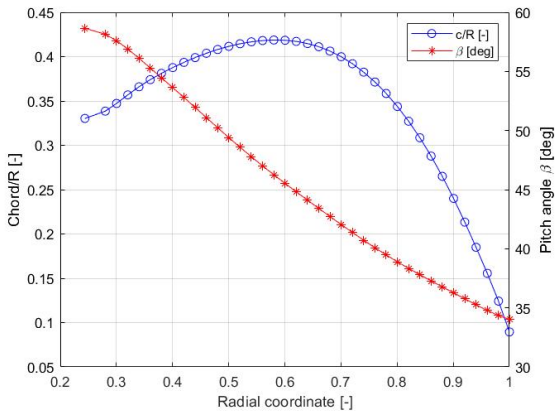

Figure 8.13: Normalised chord and the pitch angle of the APIAN propeller.

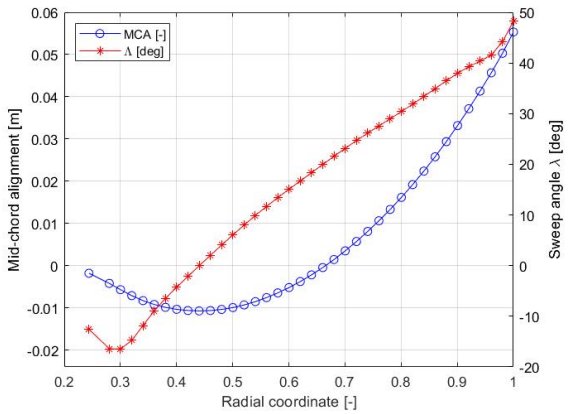

Figure 8.14: Mid-chord alignment and the dependent sweep angle of the APIAN propeller.

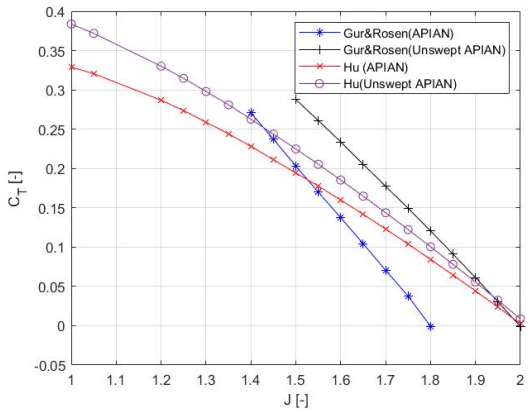

Figure 8.15: Thrust coefficient of both the actual APIAN propeller and an APIAN propeller without swept blades as computed by the Gur and Rosen BEM implementation and the BEM-Hu implementation

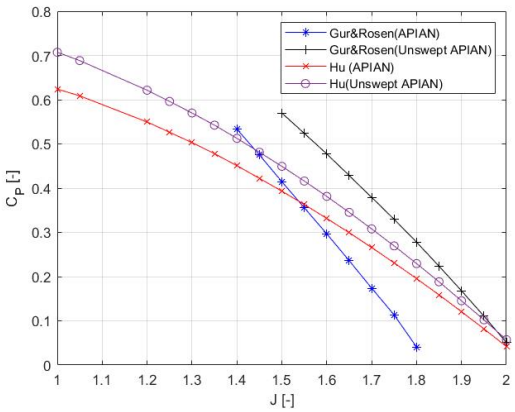

Figure 8.16: Thrust coefficient of both the actual APIAN propeller and an APIAN propeller without swept blades as computed by the Gur and Rosen BEM implementation and the BEM-Hu implementation

and induced velocities shown in the cross section of a blade element, whereas the Hu-implementation directly corrects the elemental lift and drag coefficients for blade-sweep. This is a clear difference in modelling blade sweep, which has an effect on the resulting thrust and power coefficient plots.

As shown in figure 8.15, the difference in results between the approaches is especially clear near zero thrust ($C_T = 0$). At a thrust coefficient of zero, a different advance ratio exists for these BEM-simulations. For the simulation by the BEM-Hu model, only the loading coefficients are corrected, which means no correction is made at zero thrust. As a result, the advance ratio at zero thrust is the same for both the swept-bladed APIAN propeller and the unswept-bladed APIAN propeller. For the Gur and Rosen simulation, blade sweep is modelled in a different manner. Since there is no induction at zero thrust, the only correction for a sweep angle is the correction applied to the azimuthal velocity (as shown in figure 8.17). However, contrary to the results by the Hu-simulation, this correction has a significant impact on results at zero thrust. Since the correction of the azimuthal velocity is applied, the rotational speed at which a thrust coefficient of zero occurs is higher for the swept-bladed APIAN propeller. Therefore, the point of zero thrust for the swept-bladed APIAN propeller occurs at a lower advance ratio compared to the unswept propeller.

Besides the findings at zero thrust, additional differences in results occur for a positive thrust. Due to the direct correction on the thrust and power coefficient by the Hu-model, the difference in thrust coefficient between the swept-bladed propeller and a straight-bladed propeller simulation gradually increases for a decreasing advance ratio. On the contrary, this effect does not occur for the simulations by the Gur and Rosen-implementation, as the difference between the results for the swept-bladed propeller and straight-bladed propeller slightly decrease for a decrease in advance ratio.

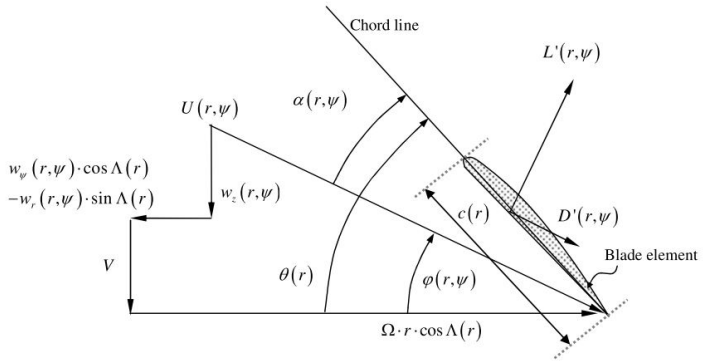

Figure 8.17: Cross-section of a blade element as defined by the BEM-implementation of Gur and Rosen[29]

For the comparison between the experimental results[48], CFD results[48] and BEM-model implementations of Gur and Rosen and Hu, the thrust and power coefficients are computed for advance ratios dictated by the available data. For both the CFD-results and wind-tunnel experimental results, measurements were taken at advance ratio's of J = 1.1, J = 1.4 and J = 1.75. Therefore, advance ratios are used in the range of 1.0 to 2.0 with an interval of 0.05 in order to establish the performance of the numerical models. The thrust and power coefficients for both the BEM-simulations and the CFD- and experimental results are shown in figure 8.18 and figure 8.19.

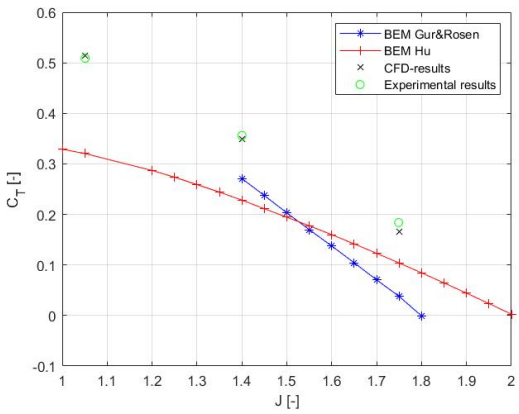

Figure 8.18: Thrust coefficient of the APIAN propeller generated by a CFD simulation, an experiment, a BEM-simulation by the HU-implementation and a BEM-simulation by the Gur and Rosen-implementation

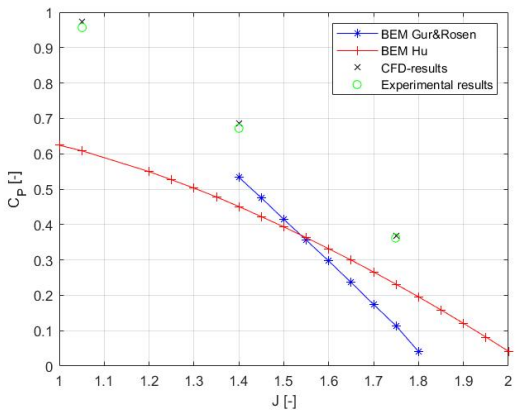

Figure 8.19: Power coefficient of the APIAN propeller generated by a CFD simulation, an experiment, a BEM-simulation by the HU-implementation and a BEM-simulation by the Gur and Rosen-implementation

As shown in both these figures, the experimental results and the results of the higher order CFD-simulation are in close agreement. However, the simulations performed by both BEM-models show results with a different behaviour. By comparing the generated results, it can be concluded that these models generate results which are not in agreement with CFD- and wind-tunnel results for propellers with a high blade solidity and highly swept blades. When looking at similarities between the experimental and CFD results and the BEM-models, it seems that at higher advance ratios the model of Hu generates more similar results to experimental and CFD results compared to the model by Gur and Rosen. On the contrary, for the lower advance ratios, thus higher thrust coefficients, the BEM-model by Gur and Rosen seems to show closer agreement with the results. Since the BEM-model simulation by Gur and Rosen did not converge for advance ratios smaller than 1.4, this final statement can be challenged.

For the purpose of aerodynamic and aeroacoustic propeller optimization, the BEM-implementation by Gur and Rosen is disqualified based on the thrust coefficient diagram. For the highly swept APIAN propeller blade, the BEM-implementation by Hu generates more accurate results compared to the BEM-implementation by Gur and Rosen for thrust coefficients C_T lower than 0.2. However, in this thesis a different definition of the

thrust coefficient, T_C, is used. Nevertheless, verification showed that throughout the optimization study, the calculated thrust coefficient C_T does not exceed a value of 0.2. Therefore, the BEM-implementation by Hu is used in the propeller optimization study.

In order to build confidence in this BEM-implementation by Hu, an ICAS-reference is used[15]. Here, a similar BEM-implementation is used to generate aerodynamic results for a 6-bladed propeller with a similar blade solidity compared to the 6-bladed XPROP. The results generated by the BEM-implementation by Hu for thrust coefficients smaller than 0.2 agree very well with experimental results generated by Geng et al., as shown in figure 8.20. Therefore, the BEM-implementation by Hu is used in the optimization study. There are two additional reasons which support this selection. Firstly, the 6-bladed XPROP is used as a baseline propeller in the optimization study, which is similar to the propeller used in the ICAS-reference. Secondly, the bounds on the maximum mid-chord alignment in the optimization study are similar to the mid-chord alignment of propeller which is used as a validation-case in the ICAS-paper. This means, in the entire optimization study, aerodynamic efficiency can be determined according to a similar accuracy compared to results in the ICAS-reference.

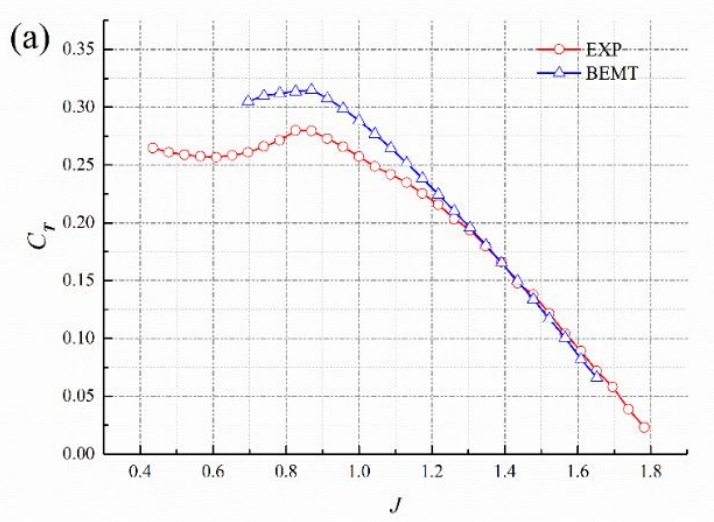

Figure 8.20: Comparison between experimental and BEMT predicted results for the M-type propeller (which is a similar propeller compared to the XPROP in terms of blade solidity and blade count)[15]

8.3. HST-model Verification

Besides verification of the used BEM-model, the HST-model that was applied in this optimization study also needs to be verified. In this section, the HST-model is first verified by making the comparison to another HST-model implementation. Second, the results are verified by a qualitative comparison between the shapes of computed noise sources and the shapes of the noise sources as dictated by theory. Third, the sensitivity of the number of harmonics on the noise emissions is investigated. The choice was made to perform this qualitative comparison rather than validation, since no experimental data is available. However, it should be stressed that extensive validation of the HST-model has been performed by others[27, 40].

8.3.1. Comparison of Model Implementation

The results of the implemented HST-model are compared to another independent HST-model implementation by Goyal with equal inputs. This means both HST-models generated directivity plots for the same operating conditions, the same propeller geometry and the same radial lift and drag coefficients. Since the HST-model implementation by Goyal used analytical expressions for the chordwise thickness- and loading distributions, these were temporarily implemented to verify the HST-model used for the optimization study. These expressions for chordwise thickness- and loading are parabolic distributions, shown in equation 8.1 and 8.2.

$$T(x) = 1 - 4x^2 \tag{8.1}$$

$$\begin{cases} f_d(x) = 1.5 - 6x^2 \\ f_l(x) = 1.5 - 6x^2 \end{cases} \tag{8.2}$$

For the comparison, the 3-bladed XPROP is evaluated at an advance ratio of 0.9, a free-stream velocity of 30 m/s and a collective pitch angle of 15°. The radiation angle θ is varied from 0 to 360° with a constant distance of 10 radii from origin to observer point (2.032 meter). Using these input conditions, the directivity plots for the thickness, lift and drag sources were compared. These directivity plots proved to be identical, which increases the confidence in the HST-model implementation.

8.3.2. Noise Source Shape Verification

The shape of the noise sources are a second check to verify if the noise computations are correct. The directivity plots for thickness and loading noise are plotted and compared to the noise source shapes obtained from literature[49]. The theoretical patterns for noise due to thickness and torque should be a dipole-shape, while the theoretical pattern for noise due to thrust should a quadrupole-shape. These plots are shown in figure 8.21, figure 8.22 and figure 8.23. The directivity plots generated by the HST-model implementation for the thickness, torque and thrust noise sources are shown in figure 8.24, figure 8.25 and figure 8.26 respectively. The two-lobed pattern which characterises the dipole shape for thickness and torque noise is similar for both the generated plots and the plots obtained from theory. Likewise, the four-lobed pattern which characterises the quadrupole shape for thrust noise is similar for the generated plot and the plot obtained from theory. The theoretical patterns and the generated directivity patterns differ due to the use of the retarded system and a specific propeller geometry. However, these plots are qualitatively similar.

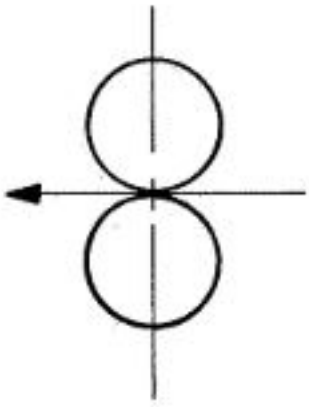

Figure 8.21: Theoretical thickness noise pattern[49]

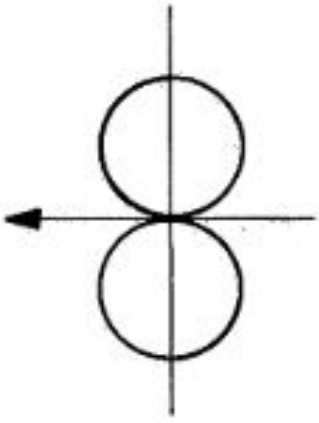

Figure 8.22: Theoretical torque noise pattern[49]

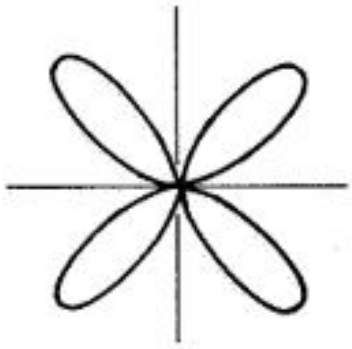

Figure 8.23: Theoretical thrust noise pattern[49]

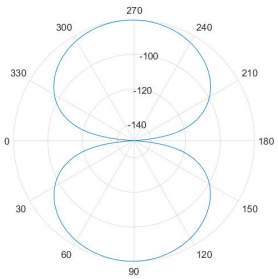

Figure 8.24: Thickness directivity plot

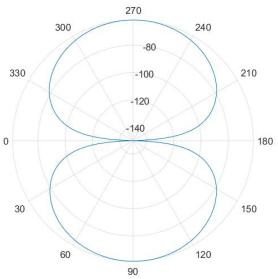

Figure 8.25: Torque directivity plot

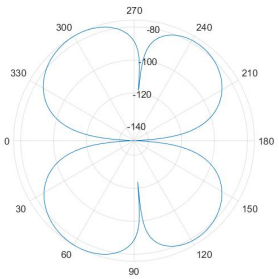

Figure 8.26: Thrust directivity plot

8.3.3. Sensitivity Number of Harmonics

In this section, a sensitivity analysis is performed to obtain the lowest acceptable amount of harmonics. The lowest order harmonics which are considered dominant compared to the higher order harmonics are defined as the lowest acceptable amount of harmonics. A low amount of harmonics should be considered, as the computational cost should remain low, while the accuracy of the results should not be affected. Therefore, the contribution of the first four harmonics on the overall sound pressure is assessed. Three resulting directivity plots of TSSP for the 3-bladed XPROP with a pitch angle of 30° and an advance ratio of J=0.9 are shown in figure 8.27, for either the first harmonic, the first two harmonics, the first three harmonics or the first four harmonics. In figure 8.27 the harmonics are referred as m. It can be concluded that the four plots in the figure are nearly identical, demonstrating that the first harmonic is dominant to the other harmonics.

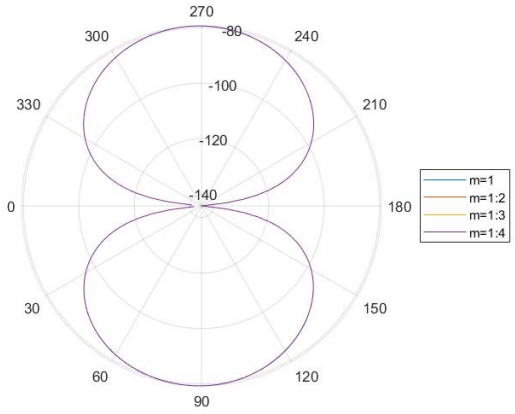

Figure 8.27: Directivity plot showing the contribution of additional harmonics to the overall TSSP

Additionally, a quantification is given in table 8.2 of the contribution of the second, third and fourth harmonic to the overall TSSP. The differences in TSSP indicated in the table show the contribution of the m^{th} harmonic to the TSSP in dB with respect to the previous harmonic. As shown, the average contribution of the second harmonic to the TSSP in comparison to the first harmonics is $1.32x10^{-2}$ dB. This is already considered as a relatively small contribution to the overall TSSP. When adding the third harmonic, it is found that the contribution is only $7.79x10^{-6}$ dB to the overall TSSP, which makes it an insignificant contribution. Therefore, only the first two harmonics are used to generate optimization results.

Table 8.2: Quantification of the contributions of the second, third and fourth harmonic to the overall TSSP

	Maximum TSSP	**Δ TSSP wrt previous m**
m = 1	-79.36	0
m = 1:2	-79.34	$1.32x10^{-2}$
m = 1:3	-79.34	$7.79x10^{-6}$
m = 1:4	-79.34	$3.72x10^{-7}$

9

Optimization Results

In this chapter, the numerical results of the optimization study are presented. Based upon these results, the research questions are answered. Firstly, in section 9.1, a discussion is provided of the operating conditions at which the optimization study is performed. Secondly, the optimization results are discussed in section 9.2. For the entire optimization setup, please refer to chapter 7.

9.1. Evaluation Setup

In this section, the value for the thrust coefficient is identified and the freestream conditions which are used in the optimization routine are discussed. In subsection 9.1.1, the properties of a reference aircraft in climb are established, which are used to identify the value of the thrust coefficient T_C. The thrust coefficient T_C is a non-dimensional scaling parameter, which is used as an input for the optimization process. In subsection 9.1.2, the freestream conditions are discussed. These include the ambient conditions and the freestream velocity, which are physical parameters at which the evaluations presented in this chapter are performed.

9.1.1. Thrust Coefficient

The thrust coefficient which serves as an input for all optimizations is predefined. Since the thrust coefficient is a non-dimensional scaling parameter, the thrust coefficient of a reference aircraft can be used as an input for the simulations presented in this chapter. The thrust coefficient at which the results are computed, depends on the stage of flight and on the aircraft itself. In cruise, the thrust coefficient of the aircraft will be significantly lower compared to the climb phase. In the climb phase, usually the aircraft flies in the vicinity of a residential area, where noise emissions create the highest level of disturbance. Therefore, for the applications of this study, the climb phase will be used to define the thrust coefficient. In the climb phase, the required thrust depends on the aerodynamic efficiency, the weight of the aircraft itself and the rate of climb. The aircraft taken as a reference in this study is the ATR42-500. The relevant specifications are shown in table 9.1.

Table 9.1: Relevant climb specifications of the ATR42-500[50]

Property	Value	Unit
V_{climb}	82.3	m/s
Rate of climb	9.4	m/s
Take-off weight	18,300	kg
D_p	3.93	m

These reference properties are used to approximate the thrust coefficient T_C of the ATR42-500 in climb. In order to determine the thrust value T in climb of the ATR42-500, equation 9.1 is used. This is a simple equation to determine the required thrust of the aircraft in climb for a given rate of climb. It is assumed that the lift is equal to the weight of the aircraft and that the lift-to-drag ratio is around 10. Additionally, it is assumed that the thrust is equally distributed between the two propellers of the ATR42-500. The thrust T is used to calculate the thrust coefficient T_C of the ATR42-500 in climb using the definition of the thrust coefficient $T_C = T/\rho_\infty V_\infty^2 D_p^2$. This yields a thrust coefficient of 0.15 during climb. Therefore, similar to the thrust coefficient of each propeller

of the ATR42-500, a thrust coefficient of 0.15 is used throughout this optimization study. Clearly, this is a rough estimation. Therefore, the effect of different thrust coefficients (T_C = 0.05 and T_C = 0.1) on the results are also assessed in the optimization.

$$\frac{T-D}{W} = \sin(\gamma) \tag{9.1}$$

9.1.2. Freestream Conditions

Besides the thrust coefficient, the ambient conditions which are used to evaluate the results are predefined. These are conditions at sea level, which are tabulated in table 9.2. For all evaluations, a freestream velocity of 60m/s is used, as this value avoids low Reynolds numbers. Typically for the XPROP, this results in Reynolds number larger than 1.5×10^5. At Reynolds number lower than 1.5×10^5, the performance of the propeller becomes especially sensitive to the Reynolds number, which is undesirable[12]. In addition, a velocity of 60m/s leads to maximum tip Mach numbers of approximately 0.5. Due to compressibility effects, a proper BEM-simulation at higher Mach numbers is not possible.

Table 9.2: Ambient conditions used in the optimization study

Property	Value	Unit
T_{amb}	288.15	K
ρ_{amb}	1.225	kg/m^3
h	0	m
V_∞	60	m/s
P_{amb}	101325	Pa

9.2. Optimization Results

In this section the optimization results are presented. These results are twofold. In subsection 9.2.1, optimization results are shown for a design vector only including the operational variables advance ratio and pitch β. Subsequently, in subsection 9.2.2, optimization results are shown for a design vector including advance ratio J, pitch β and mid-chord alignment MCA. By using this approach, an assessment of the impact of blade sweep on noise reduction is made. In subsection 9.2.3, a discussion based on the optimization results is provided of the impact of blade sweep on noise reduction as a function of freestream conditions and propeller geometry.

9.2.1. Results for Advance Ratio and Pitch

First, the results are shown for the design vector including advance ratio and pitch. An important note is that the advance ratio is only altered by varying the operational speed and thus the tip Mach number of the propeller. This means the freestream velocity and propeller diameter are constant throughout the optimization. According to chapter 7, this leads to the following design vector:

$$\overline{x} = \begin{bmatrix} J[-] \\ \beta[rad] \end{bmatrix} \tag{9.2}$$

As discussed in chapter 7, there are two approaches to optimize the design variables for both objectives. These are briefly repeated here:

- The optimization is performed by optimizing for low noise emissions in relation to a baseline noise level, which is subjected to a minimum accepted propeller efficiency constraint. The use of this constraint is based on the expectation that optimization for aeroacoustic performance is at the expense of aerodynamic performance. As such, the design space is controlled by the inequality constraint for minimum propeller efficiency.
- The relative importance of each objective, aeroacoustic or aerodynamic performance, can be changed by changing the weighting variable k. This weighting variable k can be varied from 0 to 1 to obtain a trade-off between aeroacoustic and aerodynamic performance. A weighting factor of 0 represents optimizing only for high aeroacoustic performance, while a weighting factor of 1 represents optimizing solely for high aerodynamic performance.

The first approach is used in the optimization study, while the second approach is used for verification purposes. Initial design variables of J = 1.1 and β = 30° are used. Optimizations for pure aerodynamic and aeroacoustic design were performed, which form the extreme points of the trade-off plot. Subsequently, for a thrust coefficient T_C of 0.15, a set of optimizations are performed using the first approach. Thereby, the minimum allowed propeller efficiency η_p is steadily increased as the optimization aims to minimize thrust specific noise. The increment in propeller efficiency for each optimization is 0.5%. First, the resulting design variables and optimization results are presented. Subsequently, a detailed interpretation of the behaviour of the optimum design variables is provided, followed by an assessment of the results shown in the trade-off between noise emissions and propeller efficiency.

In figures 9.1 and 9.2, the behaviour of the optimized design variables and a resulting trade-off plot is shown. Complementary to these figures, the resulting values for the design variables and performance characteristics are shown in table 9.3. For the point of maximum propeller efficiency, the average TSSP is -67.51dB and the propeller efficiency is 80.2%. For the point of minimum noise emissions, the average TSSP is -78.31dB and the propeller efficiency is 75.2%. This shows that there is a difference of 5.0% in propeller aerodynamic efficiency and 10.8dB in noise emissions between optimizing for either maximum aeroacoustic performance or maximum aerodynamic performance. Next, the optimized design variables and the resulting aerodynamic and aeroacoustic performance for the optimizations in the trade-off are further analysed.

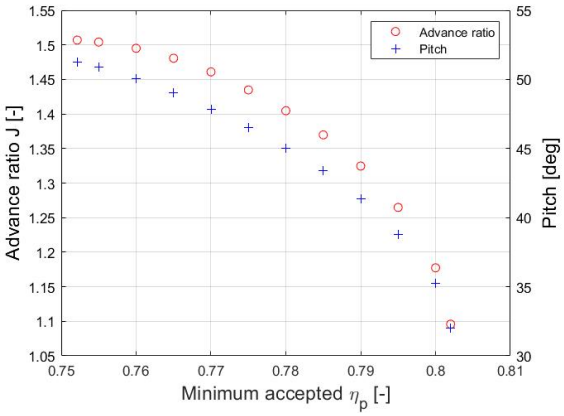

Figure 9.1: Behaviour of the corresponding design variables as a function of minimum accepted propeller efficiency.

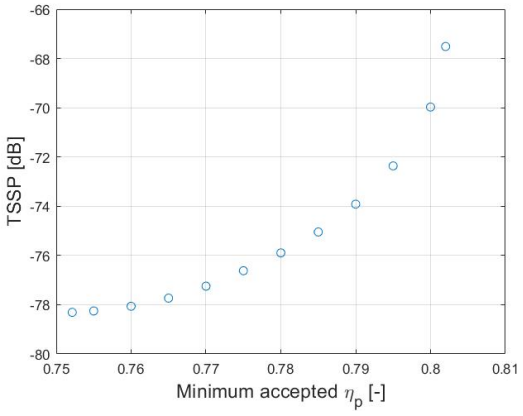

Figure 9.2: Trade-off plot for advance ratio J and pitch β as design variables, showing resulting TSSP and η_p for different values of k (T_C=0.15)

Table 9.3: Table showing optimization results and corresponding optimum design variables for different values, optimized for minimum acceptable propeller efficiency η_p.

$\eta_p(-)$	$TSSP_{mean}$ (dB)	$\mathcal{J}$ (-)	$\beta(deg)$
0.752	-78.31	1.507	51.28
0.755	-78.25	1.504	50.90
0.760	-78.06	1.495	50.07
0.765	-77.73	1.481	49.04
0.770	-77.25	1.461	47.86
0.775	-76.26	1.435	46.99
0.780	-75.90	1.405	45.03
0.785	-75.05	1.370	43.41
0.790	-73.92	1.325	41.37
0.795	-72.36	1.265	38.81
0.800	-69.97	1.177	35.21
0.802	-67.51	1.096	32.00

Optimization Results - Optimum Design Variables

From table 9.3, it becomes apparent that optimizing for high aeroacoustic performance yields a high advance ratio J and a high pitch setting β. At a high advance ratio, the azimuthal velocity of the propeller is low, which can be explained by assessing the equations stated in chapter 6. According to the far-field noise prediction equation(equation 6.5), the noise level decreases with an decreasing tip Mach number. Thus, a low propeller operational speed yields a low tip Mach number, which leads to low noise emissions. It should be stressed that the advance ratio is solely changed by a change in tip Mach number, since the propeller diameter, the freestream velocity and the speed of sound are constant. Therefore, the non-dimensional parameter which is effectively changed is the tip Mach number in the optimization. For a future study it is interesting to assess the effect of the advance ratio on aeroacoustic performance, while constraining the tip Mach number. Since the thrust coefficient T_C is a constant in the optimization study, the blade pitch setting is high to compensate for the low advance ratio to achieve low noise emissions. At maximum aeroacoustic performance, the maximum lift coefficient over the entire blade is reached, since a higher blade pitch setting leads to to boundary layer separation, which prevents a further increment of the blade pitch setting and advance ratio. Thus, lowering the operational speed at maximum aeroacoustic performance yields a lower thrust coefficient, which cannot be compensated by a higher pitch setting. Opposite to optimizing for low noise emissions, optimizing for high aerodynamic performance yields a decrease of advance ratio and pitch. The optimum point for maximum propeller efficiency occurs for the maximum ratio of propulsive- to shaft power. This point occurs at the maximum thrust-to-torque ratio of the propeller blades.

Next, the differences in optimization results in terms of aerodynamic and aeroacoustic characteristics are further analysed. The aerodynamic characteristics are discussed first. An interesting ratio which defines aerodynamic performance is the thrust-to-torque ratio. In figure 9.3, the thrust-to-torque ratio is plotted for each of the optimizations. As shown, there is a direct relation between the thrust-to-torque ratio and the propeller efficiency. In order to reach maximum thrust-to-torque ratio, the advance ratio and pitch setting are optimized to operate the propeller blades at an optimum inflow angle, effective velocity and blade angle of attack. These parameters subsequently define the local direction and magnitude of the lift and drag forces, which determine the thrust-to-torque ratio. Therefore, as shown by the behaviour of the design variables, the advance ratio and pitch decrease concurrently.

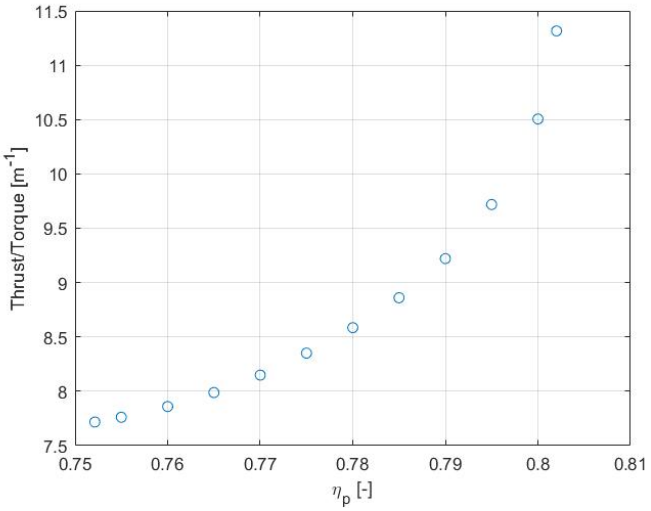

Figure 9.3: Resulting thrust-to-torque ratio for each of the optimizations for advance ratio and pitch

Since the thrust coefficient and blade planform remained equal for each optimization, there is no significant change in the blade loading between optimizing for low noise and high propeller efficiency. However, there is a significant difference in angle of attack α. In figure 9.4, three plots are shown of the radial distributions of angle of attack for optimizations with a minimum propeller efficiency of η_p = 75%, η_p = 78.5% and η_p = 80%. As shown, there is an overall higher angle of attack for the optimization with η_p = 75% compared to the optimization for η_p = 80%. The difference in angle of attack is explained by the fixed thrust constrained. As discussed, optimizing for low noise emissions yields a low operational speed. However, there are two major consequences of this decrease in operational speed. First, a reduction of operational speed also reduces the

blade loading, since the effective velocity perceived by the blade reduces. Secondly, the inflow angle increases for a decreasing operational speed as the inflow angle is defined by the freestream velocity vector and the azimuthal velocity vector. Figure 9.5 shows the inflow angle for optimization of minimum accepted propeller efficiencies η_p = 75%, η_p = 78.5% and η_p = 80% as a function of the radial coordinate. Since the inflow angle decreases for a reduction in operational speed, the pitch β of the blade is increased, both to increase the angle of attack to maintain the thrust coefficient and to compensate for the increment of inflow angle.

A side note should be made on the radial distribution for pure aeroacoustic performance shown in figure 9.4. At the tip of the blade there is an angle of attack of 16°, which is significantly large. It is dependent on the airfoil shape whether or not non-linear effects such as boundary layer separation occur, but it is evident that the probability of these effects to occur increases with this large angle of attack. Whereas this might result in some concerns, figure 9.4 also shows that the highest angle of attack occurs at the tip. At the tip, the blade loading is the smallest, which led us to assume that the error induced by potential effects remain insignificant.

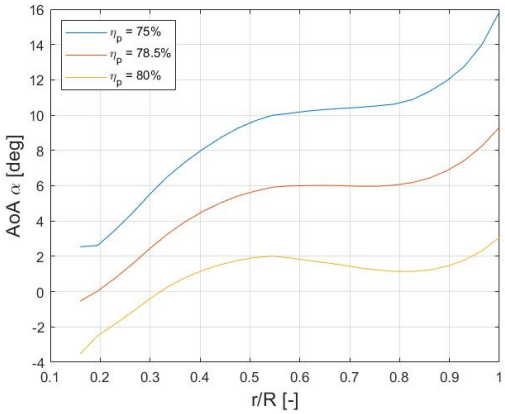

Figure 9.4: Radial distribution of angle of attack α for three optimizations with minimum accepted propeller efficiency of η_p = 75%, η_p = 78.5% and η_p = 80%.

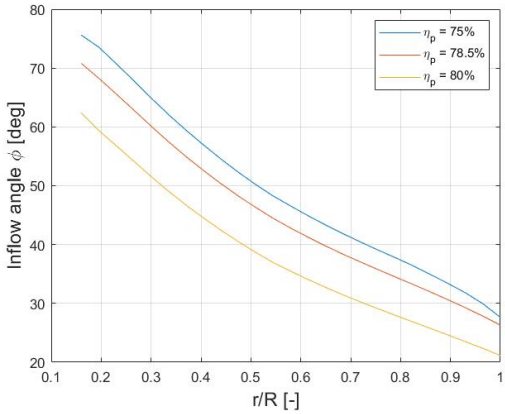

Figure 9.5: Radial distribution of inflow angle φ for three optimizations with minimum accepted propeller efficiency of η_p = 75%, η_p = 78.5% and η_p = 80%.

After having discussed the aerodynamic characteristics, now the aeroacoustic characteristics are discussed. An assessment is provided of the contribution of loading and thickness noise to the overall noise level. In figure 9.6, the loading and the thickness noise contributions are shown for each of the optimizations. For all optimizations, the conclusion can be drawn that the average TSSP at 60°, 90° and 120° at a sideline parallel to the propeller axis is dominated by loading noise. This is caused by the low freestream velocity of 60m/s at which the evaluations are performed, which leads to a low tip Mach number[19].

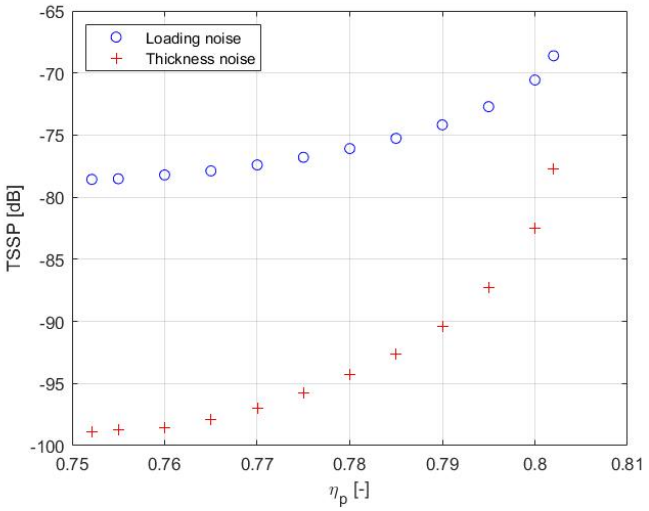

Figure 9.6: Contributions of loading and thickness noise to the overall noise level for each optimization shown in figure 9.2.

However, the contribution of thickness noise grows as the minimum acceptable efficiency increases. This is caused by the increase of operational speed as the advance ratio decreases. For higher blade speeds, the contributions of the thickness noise to the overall noise level grows since the amount air which is being displaced by the propeller blade increases as well.

The difference in contribution of thickness- and loading noise between optimization for pure aerodynamic performance and pure aeroacoustic performance is illustrated using directivity plots. These directivity plots provide additional information about the change of noise level over the complete directivity pattern. Directivity plots are displayed with the design variables resulting from pure aerodynamic and pure aeroacoustic performance. For an optimization for pure aeroacoustic performance(figure 9.7), the high advance ratio and high pitch angle lead to a significant difference between the loading and thickness contribution to the overall noise levels. However, for the optimization for pure aerodynamic performance(figure 9.8), the advance ratio and pitch are lower, which leads to a larger contribution of the thickness noise with respect to the loading noise.

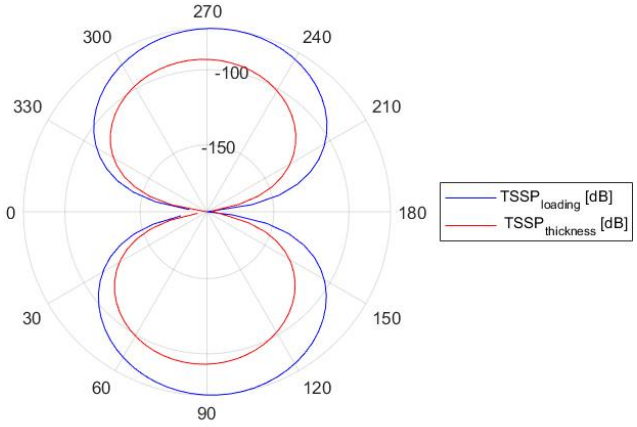

Figure 9.7: Directivity plot for design variables resulting for an optimization for pure aeroacoustic performance, showing both the contribution of thickness and loading noise to the overall noise levels

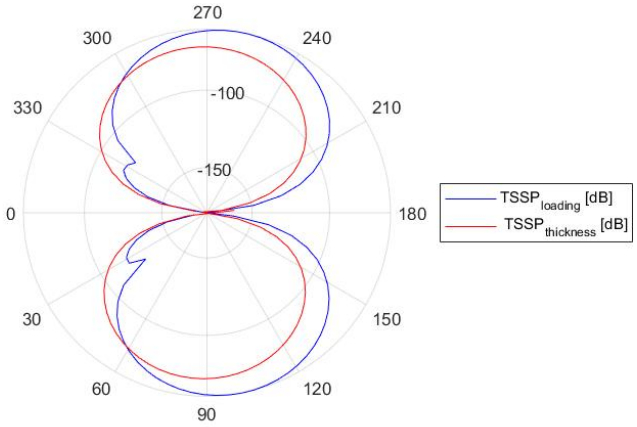

Figure 9.8: Directivity plot for design variables resulting for an optimization for pure aerodynamic performance, showing both the contribution of thickness and loading noise to the overall noise levels

There are two interesting observations which are made with respect to figure 9.7. First, for these optimization results the thickness noise is the dominant contribution to the overall noise level over a range of approximately 120° of the directivity plot. This is an unexpected finding, since the contrary was found in figure 9.6 where the overall contribution of loading noise is significantly higher compared to the contribution of thickness noise to the overall noise level. This shows that a sideline approach with sample points defined at 60°, 90° and 120° induces an error for certain directivity angles. The second observation is the node in the directivity plot for loading noise, which was not visible for the directivity plot for optimized aeroacoustic design. This node exists due to the dipole radiation of the steady loading noise, which is caused by the fluctuation of fluid forces at blade passage frequency at an observer location[51]. The location of this node depends on the ratio of freestream Mach number to blade Mach number squared, which is represented in the wave number k_y of the implementation by Hanson[27]. For figure 9.8, the node is not visible, since it is located at a directivity angle close to 0° due to the small blade Mach number of the propeller.

Optimization Results - Aerodynamic and Aeroacoustic Performance

Next, the aerodynamic and aeroacoustic performance trade-off is assessed. As discussed, in this thesis there are two ways to which multiple objectives are incorporated in the optimization process. In order to verify the optimization results generated using minimum accepted propeller efficiencies, the optimization process is repeated with weighting variables. The weighting variables are varied between 0 (optimization for pure aeroacoustic performance) and 1 (optimization for pure aerodynamic performance), with increments of 0.11. The resulting trade-off plot with results generated by both optimization approaches is shown in figure 9.9. This figure shows that a similar trend exists for both the optimization approach by weighting factors and the optimization approach by a propeller efficiency constraint.

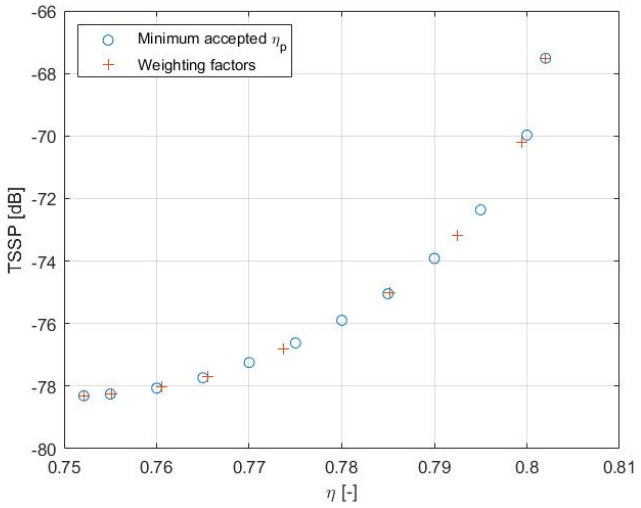

Figure 9.9: Trade-off plot for J and β, showing results for TSSP and η_p (T_C=0.15). Results are generated by using either of the two optimization approaches.

In chapter 8, it was argued that the implemented aerodynamic BEM-model for this study would be the Hu- model, since it provided accurate results for thrust coefficients lower than 0.20. As the difference between the selected thrust coefficient of 0.15 and 0.20 is small, the optimization is also performed for thrust coefficients of 0.05 and 0.1 to assess if similar trade-off plots are generated and to assess the behaviour of the optimizations to a change in thrust coefficient in general. The resulting plots are shown in figure 9.10 and figure 9.11 for T_C = 0.05 and T_C = 0.10 respectively. Both thrust coefficients 0.05 and 0.1 show a similar trend as the selected coefficient of 0.15. This means that the observations addressed for the optimizations for a thrust coefficient of 0.15 are consistent with observations for optimizations with lower thrust coefficients.

By plotting the trade-off plot for different thrust coefficients in the same graph, the effect of a different thrust coefficient is clearly visualised(figure 9.12). If a lower thrust coefficient and corresponding lower thrust setting is required, the optimum points show a decrease in noise emissions and an increase in propeller efficiency. This means that when regarding the aeroacoustic performance, the propeller is able to operate at a lower operational speed, thereby decreasing tip Mach numbers and reducing noise emissions. For the aerodynamic performance,

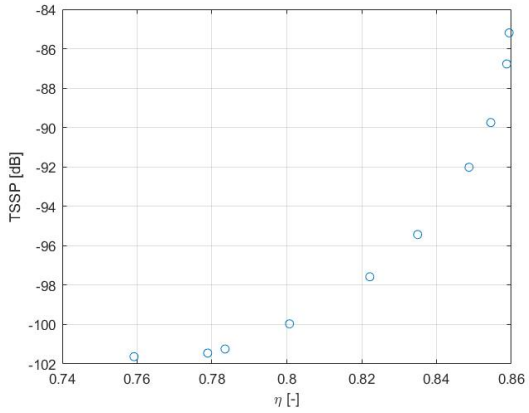

Figure 9.10: Trade-off plot for advance ratio J and pitch β as design variables, showing resulting TSSP and η_p for different values of k (T_C=0.05)

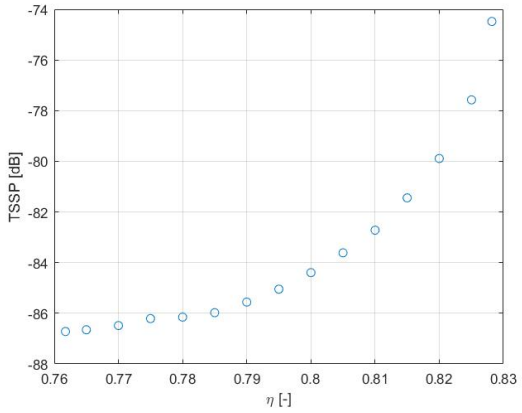

Figure 9.11: Trade-off plot for advance ratio J and pitch β as design variables, showing resulting TSSP and η_p for different values of k (T_C=0.10)

the lower required thrust leads to a decrease in tip losses. These losses decrease since the decrease of blade loading leads to a decreased amount of swirl in the slipstream of the propeller and since a smaller acceleration of the flow leads to a decrease in axial induction factor.

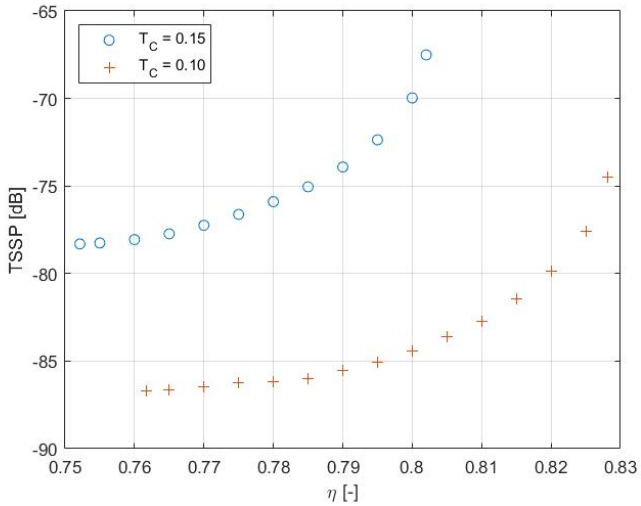

Figure 9.12: Trade-off plot for $\bar{x}$ = [J β], both for T_C = 0.15 and T_C = 0.10.

To provide an analysis of the sensitivity of noise reduction versus efficiency penalty, the optimization results are used for a mathematical fit. It seems that for each of the trade-off plots (T_C=0.05, T_C=0.10 and T_C=0.15), the points for maximum aeroacoustic and aerodynamic performance approach an asymptote. Therefore, an error type function is considered appropriate as a fitting curve through the data. Specifically, the inverse of the complementary error function is used to obtain a fit, as shown in figure 9.13. This choice is made because this function features clear x- and y asymptotes. The fitted curve is generated by using the MATLAB 'fittype'-function, which uses a nonlinear least-squares method to obtain the fitted function.

$$f(x) = a - \frac{b}{erf((x-c)/d)} \tag{9.3}$$

where:

a = - 83.87
b = 5.164
c = 0.8182
d = 0.0556

The error function is defined as:

$$erf(x) = \frac{2}{\sqrt{\pi}} \int_0^x e^{-t^2} dt \tag{9.4}$$

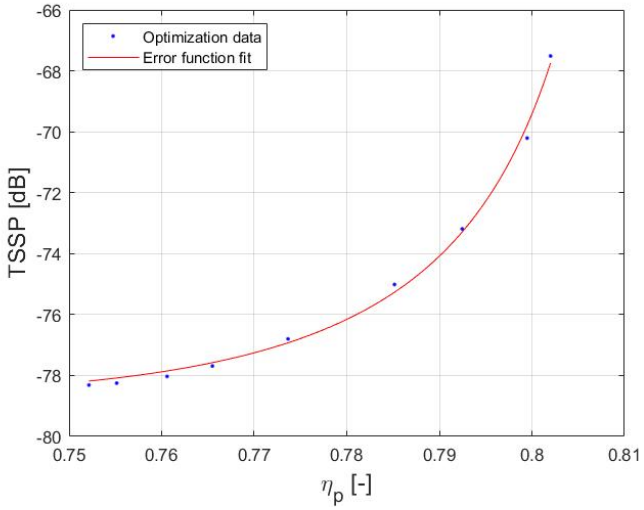

Figure 9.13: Trade-off plot for $\bar{x}$ = [J β], including fitted curve based on an error type function for thrust coefficient T_C = 0.15.

An interesting observation by assessing this fit is that a distinctive trend exists in the trade-off between aerodynamic and aeroacoustic performance for a design vector including advance ratio J and pitch β. At the design point of maximum propeller efficiency, a noise reduction can be achieved at a small penalty in terms of propeller efficiency. At the design point of maximum propeller efficiency a noise reduction of 5.7dB can be obtained for a penalty in propeller efficiency of 1%. For a penalty in propeller efficiency of 2%, a noise reduction of 8.1dB can be obtained. Figure 9.13 shows that a larger penalty in terms of propeller efficiency leads to a larger noise reduction. However, the sensitivity of noise reduction decreases as the maximum allowed propeller efficiency penalty increases.

This is further quantified by the gradient of the fit, shown in figure 9.16, at the point for minimum noise emissions. At this point, there is a gradient of 0.31dB in noise emissions for 1% in propeller efficiency. This also means at the design point of minimum noise emissions, a propeller efficiency increase can be obtained at a small cost in noise emissions. At the point for maximum propeller efficiency, there is a gradient of 9.4dB in noise emissions for 1% in propeller efficiency. The increment of the gradient as a function of minimum accepted propeller efficiency shows that the sensitivity of a noise reduction increases as a function of a larger minimum acceptable propeller efficiency. The trend also shows a rounded transition corner when optimizing for both objectives equally.

In figure 9.14 and figure 9.15 the resulting fits for the optimizations for T_C = 0.05 and T_C = 0.10 are displayed, which shows that for both coefficients an equal trend exists. To make a comparison of figures 9.13- 9.15, figure 9.16 is computed in which the gradient for each of the fits with different thrust coefficients is shown. The gradients show the increase of noise emissions in dB for a percentage increase of propeller efficiency. As shown, there is a similar trend between the optimizations for each thrust coefficient. The difference in derivative for optimizations of thrust coefficients of 0.05 and thrust coefficients of 0.1 and 0.15 is likely to be induced by fitting errors. It can be concluded that the increasing gradient of the trade-off between propeller efficiency and propeller noise emissions is independent of thrust coefficient, given that the thrust coefficient is positive.

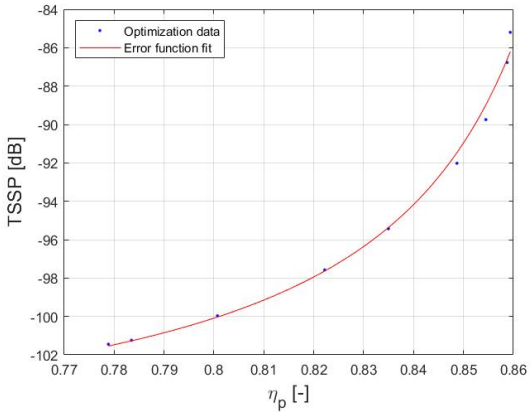

Figure 9.14: Trade-off plot for $\bar{x}$ = [J β], including fitted curve based on an error type function for thrust coefficient T_C = 0.05.

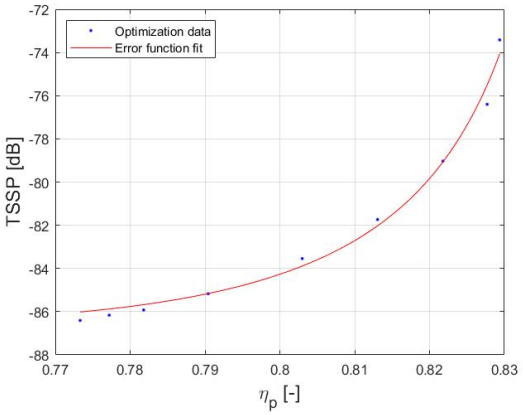

Figure 9.15: Trade-off plot for $\bar{x}$ = [J β], including fitted curve based on an error type function for thrust coefficient T_C = 0.10.

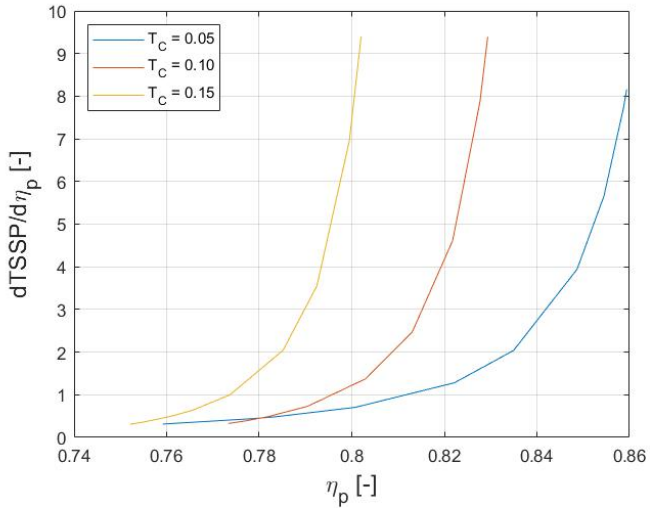

Figure 9.16: Derivative of fits shown in figure 9.13, figure 9.14 and figure 9.15. The derivatives show an increase of noise emissions for each percent in increase of propeller efficiency.

It is interesting to note that the results presented apply for a propeller operating in climbing conditions. Depending on the length of the flight, the climbing phase of flight is usually a minor fraction of the total mission. By only optimizing advance ratio and pitch, according to these results noise emissions around airports can be reduced approximately 11dB, while there is sacrifice of approximately 5% in propeller efficiency for a relatively short amount of time. This sacrifice in propeller efficiency is negligible compared to the overall propeller efficiency during the mission.

9.2.2. Results for Advance Ratio, Pitch and MCA

In this section, the results are shown for a design vector including three design variables: the advance ratio J, pitch β and the mid-chord alignment MCA. The performance difference by adding the mid-chord alignment into the design vector is assessed. As discussed in chapter 4, the mid-chord alignment is parametrised by means of a Bézier curve, which is defined by a number of control points. The x and y position of these control points are used as design variables in the design vector. According to the analogy explained in chapter 7, using 3 control points to represent the mid-chord alignment distribution means adding 3 extra design variables to the design vector. For 4 control points, 5 extra design variables are added to the design vector. Both the 3 and 4 control point cases are considered in the optimization to assess the difference in MCA-distribution on optimization results for a different number of control points. For 4 control points the design vector is defined as:

$$\overline{x} = \begin{bmatrix} J[-] \\ \beta[rad] \\ y_{CP_2}[-] \\ y_{CP_3}[-] \\ x_{CP_2}[-] \\ x_{CP_3}[-] \\ x_{CP_4}[-] \end{bmatrix} \tag{9.5}$$

After generating optimization results for the design vector including control points defining mid-chord alignment, these results can be used to assess the impact of blade sweep on the aerodynamic and aeroacoustic results. A trade-off plot is used to present these aerodynamic and aeroacoustic results, which shows the potential performance increase by using blade sweep for each one of the objectives. Complementary to the trade-off plot are the optimized design vectors. The optimized design variables give an insight into the mechanism to which an optimized mid-chord alignment can decrease noise emissions of a propeller blade.

Figure 9.17 shows a trade-off plot with the results for a design vector including advance ratio and pitch, with and without including mid-chord alignment. At the top right of the figure(η_p > 0.8 and TSSP > -68dB), optimizations are shown for optimum propeller efficiency, where there is a negligible difference in results. This means, an application of blade sweep does not improve the aerodynamic performance for the 6-bladed XPROP. For optimizations performed at a minimum allowed propeller efficiency of η_p = 78%, there is a difference of less than 0.5dB in noise emissions between the baseline propeller and an optimized propeller. The noise benefit by applying sweep for minimum acceptable propeller efficiencies around 76.5% to 78% are approximately 0.5dB. Compared to equivalent studies, a noise reduction of 0.5dB due to blade sweep application is not significant. A study by Geng et al.[15] showed a noise reduction of 2.9dB and a study by Pagano et al.[9] resulted in a noise reduction of 1.5dB, both by applying blade sweep. Therefore, an elaboration of the sensitivity of the blade sweep effect on noise reduction is provided in section 9.2.3.

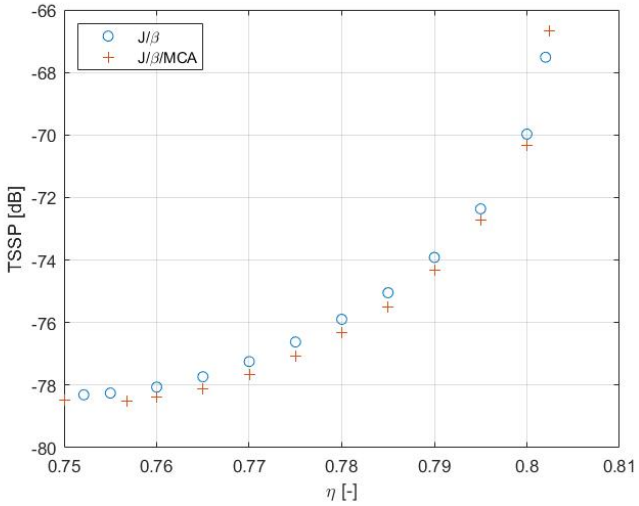

Figure 9.17: Trade-off plot for either $\bar{x}$ = [J β] and $\bar{x}$ = [J β MCA], showing results for TSSP and η_p (T_C=0.15).

Next, the optimized design vectors and their optimization results are assessed for three cases:

1. Pure aeroacoustic performance optimization (k = 0)
2. Pure aerodynamic performance optimization (k = 1)
3. Multi objective performance optimization: a point near the rounded transition curve at a minimum accepted propeller efficiency η_p = 78.5%.

The optimized geometry is assessed by a noise directivity plot at optimized operational conditions and by a propeller efficiency plot for off-design conditions.

Case 1: Pure Aeroacoustic Performance Optimization (k = 0)

In the case of solely optimizing for high aeroacoustic performance, the optimum resulting mid-chord alignment and the corresponding optimum advance ratio and pitch setting are determined for a thrust coefficient of 0.15. The initial design variables include a straight blade (MCA(r) = 0), J = 1.1 and β = 30°. The optimized mid-chord alignment for 4 control points is shown in figure 9.18. The mid-chord alignment MCA and the radial position at the blade r is normalised with respect to the radius of the propeller. As shown, the mid-chord alignment is zero at the root of the blade. Moving from root to the tip, a forward sweep is gradually introduced. However, close to the tip of the blade a large backward sweep is introduced. This backward sweep angle close to the tip forces a phase offset of the noise sources close to the tip of the blade.

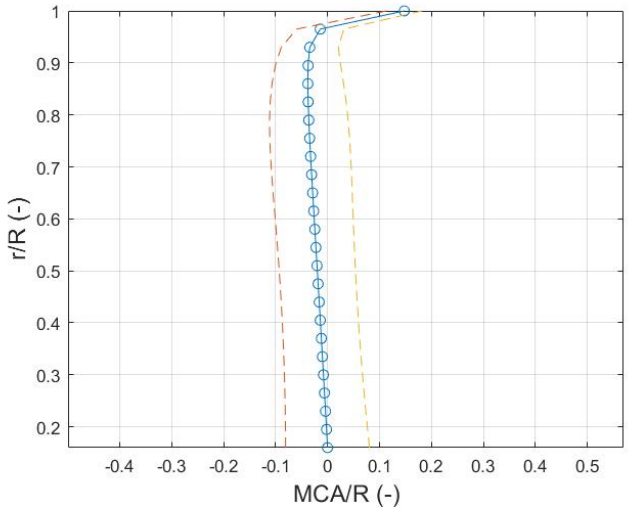

Figure 9.18: Optimized blade mid-chord alignment for the aeroacoustic performance as objective function (4 control points).

Since the strongest noise sources occur at the tip of the blade due to the highest Mach numbers, the introduction of a phase offset is most effective here. Since this phase offset can be achieved by a sweep angle[24], a large sweep angle is induced near the tip. To demonstrate that the strongest noise sources indeed occur at the tip, the real, absolute part of the complex Fourier coefficients of the acoustic pressure for the first harmonic as a function of the radial coordinate of the blade are shown in figure 9.19. The Fourier coefficients are the combined Fourier coefficients of the thickness and loading source contributions for different radiation angles for a straight blade. The amplitude of the sound waves which is represented by these Fourier coefficients is a compromise between the local loading and the Mach number at the tip. The local loading of the propeller blade decreases at the tip, while the blade Mach number is maximum at the tip. The Fourier coefficients scale quadratically with the Mach number along the radial coordinate, which is also shown in figure 9.19. The smaller increase or decrease in the Fourier coefficient values is caused by the reduction of blade loading near the tip. These graphs support the statement that the strongest noise sources occur at the tip of the blade, since the largest Fourier coefficients occur at the tip of the blade for a radiation angle of 90°.

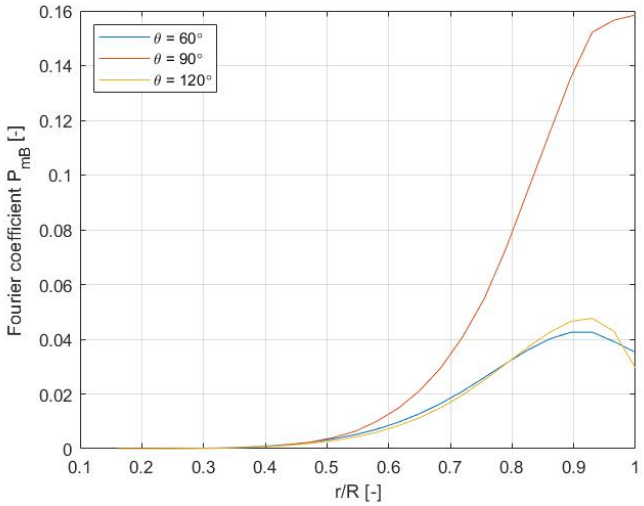

Figure 9.19: Radial distributions of Fourier coefficients of thickness and loading source contributions for different radiation observer angles for a straight blade.

Figure 9.20 shows the mid-chord alignment of 3 and 4 control points side by side. By comparing both distributions, the effect of a difference in the number of control points on the shape of the Bézier curve is illustrated. Using 3 control points to define the Bézier curve, a relatively simple quadratic Bézier curve is the result, and by using 4 control points, a cubic Bézier curve is the result. The Bézier curve defined by 3 control points shows a larger forward sweep around 40%-70% of the blade radius.

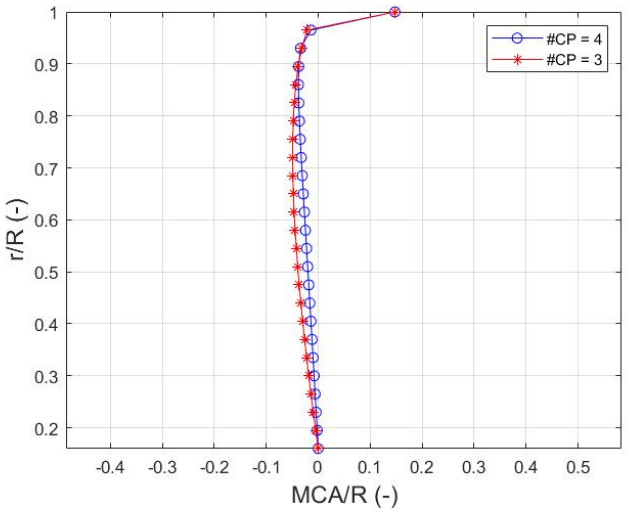

Figure 9.20: Comparison between optimized blade mid-chord alignments defined by 3 and 4 control points. Optimization was performed for pure aeroacoustic performance.

The mid-chord alignment distributions from figure 9.20 are compared to the straight-bladed design to assess the aerodynamic and aeroacoustic performance. In table 9.4, a comparison between aerodynamic and aeroacoustic performance is provided for both the baseline XPROP and the optimized propeller geometries (3 and 4 control points). In order to provide a fair comparison, the results are compared to the 6-blades XPROP with optimized operational conditions. The effect of the mid-chord alignment on key performance characteristics can only be assessed if the propeller with straight blades also operates at a thrust coefficient of 0.15 with optimum advance ratio and pitch setting for maximum aeroacoustic performance. By using this approach, the change in aeroacoustic or aerodynamic performance is solely the result of a change the distribution of mid-chord alignment.

As shown in table 9.4, the application of blade sweep shows an aeroacoustic performance increase of 0.4dB with respect to the straight-bladed propeller, which is an average noise emission decrease across three different point at a sideline at 10 radii from the propeller axis. For the propeller efficiency, there is a 1.1% decrease for the optimized MCA-shape with respect to the straight-bladed propeller. In addition, it is interesting to note that the application of blade sweep changes the value of the operational design variables. These changes are compensating for the loss of thrust generation by an increase in pitch and a decrease in advance ratio, which consequently decreases the propeller efficiency as well. As discussed in chapter 8, the application of blade sweep leads to a reduction of thrust coefficient as modelled by the BEM-model. As shown, the advance ratio decreased for both the 4-control point solution and the 3-control point solution, therefore maintaining a thrust coefficient of 0.15.

Table 9.4: Table showing optimum aeroacoustic design results for a thrust coefficient of 0.15.

	XPROP	Opt_{3CP}	Opt_{4CP}
$T_C(-)$	0.15	0.15	0.15
$\beta(deg)$	51.28	51.61	51.74
J (-)	1.507	1.483	1.486
$\eta_p(-)$	0.752	0.739	0.739
$TSSP_{mean}(dB)$	-78.31	-78.74	-78.76

Similar to the discussion given in section 9.2.1, first a detailed interpretation of the results in terms of aerodynamic performance is provided, after which an interpretation in terms of aeroacoustic performance is provided.

Case 1: Aerodynamic Performance Analysis

The effect of the optimized design including blade sweep on aerodynamic performance can be shown by analyzing the off-design conditions. By varying the advance ratio, the aerodynamic performance of the optimized design and the straight-bladed propeller can be compared. The thrust and power coefficient C_T and C_P are shown in figure 9.21 and 9.22, respectively. The propeller efficiency is shown in figure 9.23. For these graphs, an equal pitch setting is used for both the optimized geometry and the baseline geometry. As shown by these simulations, the optimized design including sweep angle induces a decrement of thrust and power coefficient. Since the propeller efficiency is dependent on the fraction of thrust-to-power coefficient, the difference in propeller efficiency is limited. These findings are in line with the verification results discussed in chapter 8.

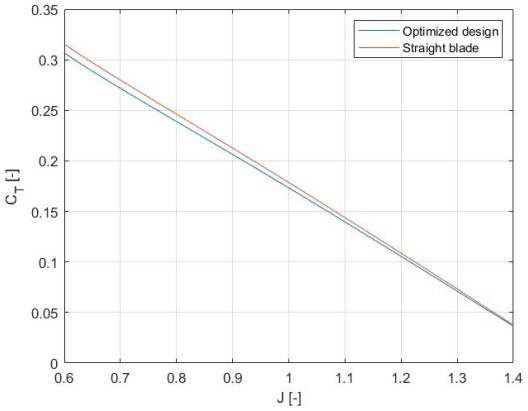

Figure 9.21: Thrust coefficient C_T as a function of the advance ratio, computed for the optimized- and the baseline design

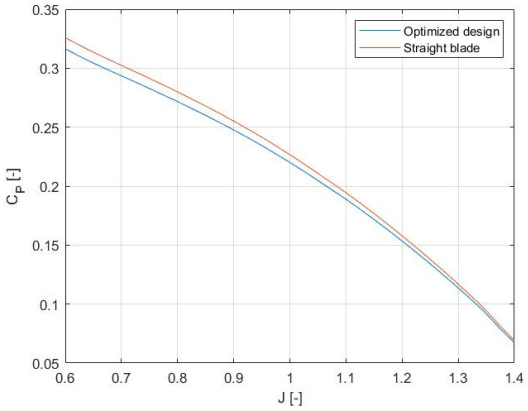

Figure 9.22: Power coefficient C_P as a function of the advance ratio, computed for the optimized- and the baseline design

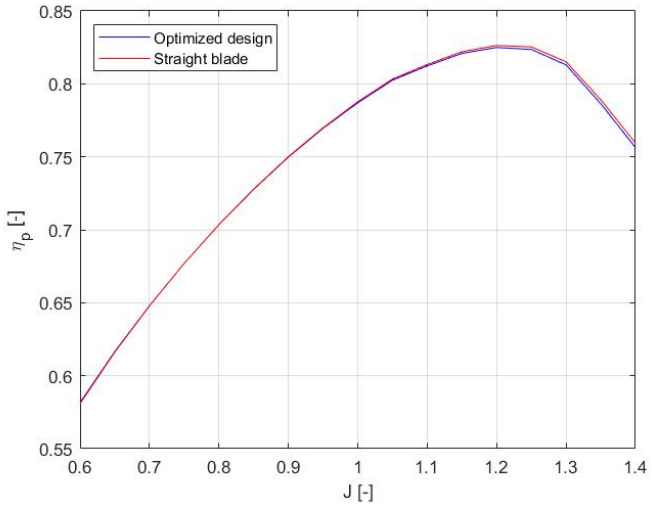

Figure 9.23: Propeller efficiency η_p as a function of the advance ratio, computed for the optimized- and the baseline design

The overall thrust coefficient and propeller efficiency are equal for the straight and swept blade. Therefore, the losses associated with applying blade sweep must be compensated by changing the advance ratio and pitch. The decrease in advance ratio and the increase in pitch lead to a higher effective velocity at the blade, which generates a larger thrust. In figure 9.24, the thrust as a function of the radial coordinate is shown for both the swept blade and the straight blade. Since there is a local application of blade sweep, the difference in the resulting radial blade loading plots is small. However, a clear difference in blade loading remains. Due to the application of blade sweep near the tip of the blade, there is loss of thrust at that location. This is a result which is consistent with the BEMT-model including simple sweep, since the application of a sweep angle leads to a direct reduction of the values for lift and drag coefficients. The loss of thrust at the tip is compensated with a higher thrust at radial positions closer to the root, which is done by decreasing advance ratio and increasing pitch. As a result of the behaviour of the operational design variables, the blade loading shifts inboard.

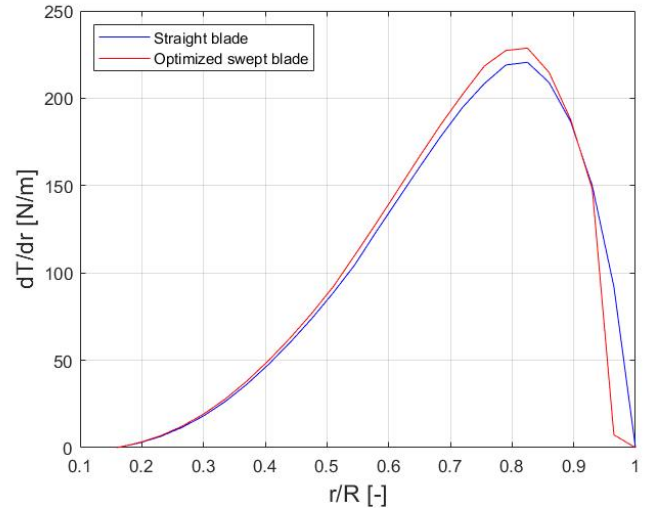

Figure 9.24: Thrust as a function of the radial coordinate of the blade, shown for the straight blade and the blade planform shown in figure 9.18.

The effect of blade sweep as modelled by the BEMT-model are further analysed by the radial plots of angle of attack and inflow angle, shown in figure 9.25 and figure 9.26, respectively. There is a difference in both inflow angle and angle of attack between the straight and swept blade, due to the difference in advance ratio and pitch. However, due to the application of blade sweep near the tip, these figures show a drastic increase of angle of

attack and a decrease of inflow angle. This can be explained by the Newton-Raphson iteration method used in the BEMT-model. At the tip, the lift and drag coefficients are corrected for the application of blade sweep. This leads directly to a decrement in the angle due to induction, since the loading in the local streamtube is decreased. Since the pitch and inflow angle without induction are assumed constant, this directly leads to an increase of angle of attack in the BEMT-model. It is questionable if these results represent the physical process, since the increase of angle of attack should generally lead to an increase in lift coefficient, while the opposite effect occurs in this model. For future studies, a suggestion is to apply the correction after the iteration, since this would prevent a change in angle of attack due to the application of blade sweep.

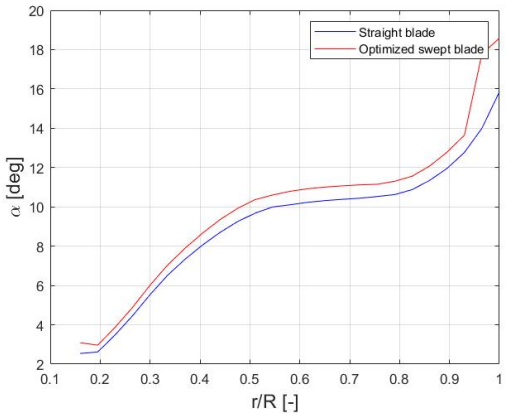

Figure 9.25: Radial distribution of angle of attack α for both the swept and straight optimization results.

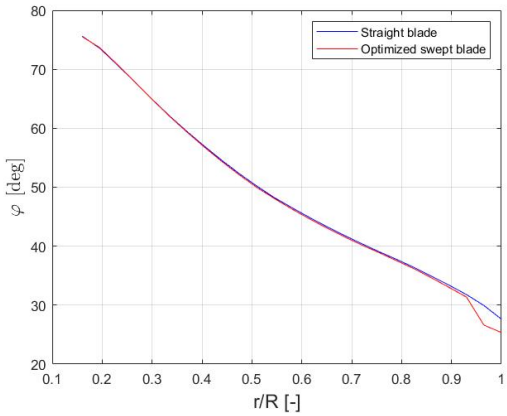

Figure 9.26: Radial distribution of inflow angle φ for both the swept and straight optimization results.

Case 1: Aeroacoustic Performance Analysis

Next, the effect of the optimized design on aeroacoustic performance is analysed. For the 6-bladed XPROP and the optimized geometry, defined by 4 control points, a directivity plot for noise emissions is constructed. As discussed, the noise reduction achieved by application of blade sweep is limited, which is illustrated once more by the directivity plot in figure 9.27.

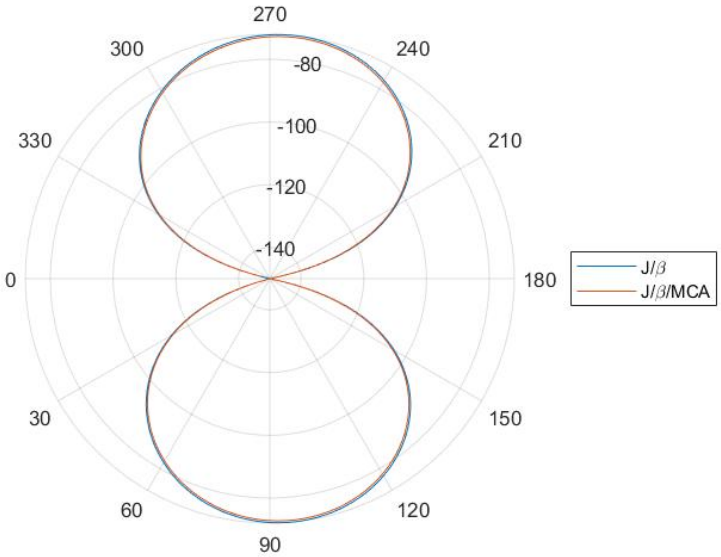

Figure 9.27: Noise emission directivity plot both for the XPROP including straight blades and the optimized blade-shape as depicted in figure 9.18

For the optimized swept blade, the pitch increases and the advance ratio decreases. However, a decrease of advance ratio leads to an increase of tip Mach number, which leads to an increment of the noise emissions by definition. Therefore, the TSSP of the optimized swept blade is calculated at the advance ratio which is optimum for the straight blade, J = 1.507, to assess the effect of advance ratio on noise emissions. For the straight blade the TSSP is -78.31dB. For the optimized swept blade the TSSP is -79.33dB. Therefore, an increment of the tip Mach number due to a required reduction in advance ratio leads to a penalty of 0.6dB in terms of noise emissions. Due to this penalty, the noise reduction which is obtained by applying blade sweep is 0.4dB instead of 1.0dB.

It is interesting to assess the effect of the application of blade sweep on the reduction in both loading and thickness noise. First, the effect of blade sweep on thickness noise is assessed. For the considered freestream Mach number, the thickness noise is not dominant, but the reduction in thickness noise due to sweep can become relevant at higher flight speeds. In table 9.5, the thickness and loading noise for both the optimized swept blade solution and the optimized straight blade solution are provided. Due to the application of blade sweep, there is a 0.7dB increase in thickness noise. This is caused by the decrease of advance ratio as a result of the loss in thrust. The thickness noise increased due to the rise in tip Mach number, which opposed the decrease in thickness noise due to phase cancellation of blade sweep.

Table 9.5: Thickness and loading noise for both the optimized swept blade solution and the optimized straight blade solution.

	XPROP	*Optimized blade*
$TSSP_{thickness}(dB)$	-99.05	-98.35
$TSSP_{loading}(dB)$	-78.45	-78.96
$TSSP_{total}(dB)$	-78.31	-78.76

The assessment of the effect of blade sweep on loading noise is more complicated. Due to the loss of thrust at the tip of the blade, the advance ratio is decreased and pitch is increased to meet the thrust constraint. Therefore, the blade loading shifts more towards the root of the blade, as shown in figure 9.24. As a result, noise reduction due blade sweep is achieved both by a shift of blade loading and phase cancellation. In order to assess the shift in loading and the phase cancellation due to blade sweep on noise reduction, multiple cases are compared at constant advance ratio of J = 1.486 and pitch β = 51.73° to avoid the influence of tip Mach number. Three assessed cased including their results are as follows:

1. For the XPROP including straight blades operating at J = 1.486 pitch β = 51.73°, the loading noise contribution to the overall TSSP is -77.98dB.

2. The loading noise contribution to the TSSP of the optimized swept blade including the loading distribution of the straight blade is calculated. This gives an insight of the noise reduction due to phase cancellation caused by the application of blade sweep. The loading noise contribution to the TSSP is -78.34dB.

3. The loading noise contribution to the TSSP of the XPROP including the loading distribution of the swept blade is calculated. This gives an insight of the noise reduction due to shift in loading inboard caused by the application of blade sweep. The loading noise contribution to the TSSP is -78.81dB.

These cases lead to the conclusion that the loading noise is mostly reduced by shifting blade loading inboard, and the phase cancellation has a smaller effect. Since the loading noise is dominant for these operating conditions, shifting the loading inboard is the most important mechanism for noise reduction by applying blade sweep. However, for an increased flight velocity, the thickness noise becomes more dominant and the MCA-to-λ ratio increases as well, at which the phase cancellation mechanism becomes more important. This is further explored in section 9.2.3.

Case 2: Pure Aerodynamic Performance Optimization (k = 1)

For pure aerodynamic performance optimization, the assessment is made whether application of blade sweep for these operating conditions enhances propeller efficiency. For this purpose, a random set of 3 different initial design vectors were used. These initial design vectors were all within the bounds of the optimization. However, the results were equal for all initial design vectors. In table 9.6, the optimization results and the optimized operational design variables are tabulated. These are compared to the optimized operational design variables of the XPROP. In figure 9.28, the optimized MCA-shape is shown.

There is a negligible difference in optimized operational design variables and optimization results between the XPROP and the optimized shape. This is supported by the shape of the MCA-distribution, which is equal to a straight blade. For an optimization for maximum propeller efficiency, the performance indicators determined by the HST-model are not included in the optimization. This means the amount of sweep which is applied by the optimizer depends on the question if blade sweep enhances propeller efficiency according to the BEMT-model including simple sweep theory. Clearly, according to the resulting straight blade which is shown in figure 9.28, the application of blade sweep does not lead to an increase of propeller efficiency according to the BEM-model. A physical explanation for this phenomenon is that application of sweep means that the bound vortex line is moved, which leads to additional shedding of trailing vortices along the blade radius. For low amounts of blade sweep, the losses associated with these trailing vortices reduces the propeller efficiency. Therefore, the optimizer does not change the values of the control points to apply a blade sweep to the planform.

Table 9.6: Table showing optimum aerodynamic design results for a thrust coefficient of 0.15.

	XPROP	Opt_{4CP}
$T_C(-)$	0.15	0.15
$\beta(deg)$	32.00	31.97
J (-)	1.096	1.095
$\eta_p(-)$	0.802	0.802
$TSSP_{mean}(dB)$	-67.51	-67.49

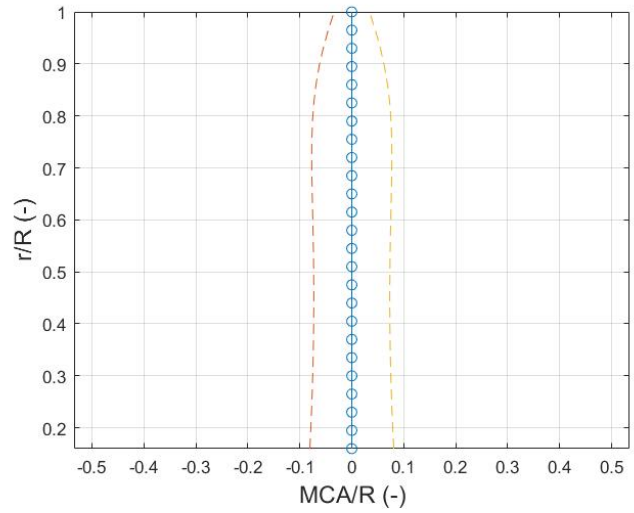

Figure 9.28: Optimized blade mid-chord alignment for pure aerodynamic optimization (4 control points).

Case 3: Multi-objective Performance Optimization

In the final case, both objectives are considered in the optimization process. An assessment is made of the reduction in noise emissions which can be achieved with blade sweep, while an equal propeller efficiency is considered for the design vector including and excluding blade sweep. This means the objective function only considers the reduction in thrust specific noise.

The propeller efficiency which is considered for this case is based on the trend shown in figure 9.13. A point of interest for further assessment is a chosen point in the rounded transition curve of the plot, which is a region

where both a reasonable aeroacoustic and aerodynamic propeller performance can be achieved. The point of interest occurs at approximately 78.5%, where the average value of the gradient dTSSP/dη appears. This point is used as a minimum acceptable propeller efficiency constraint in the optimization for $\bar{x}$ = [J β] and $\bar{x}$ = [J β MCA]. The results of the optimizations are tabulated in table 9.7 and the shape of the mid-chord alignment is shown in figure 9.29. Since the required minimum propeller efficiency is equal for the straight blade and the blade including swept blades, noise reduction is solely the result of blade sweep application to the planform. Losses due to application of blade sweep in terms of thrust or propeller efficiency are compensated by the advance ratio and pitch. For a minimum propeller efficiency of 78.5%, the application of blade sweep yields a 0.5dB noise reduction.

Table 9.7: Table showing optimum design results for design vectors $\bar{x}$ = [J β] and $\bar{x}$ = [J β MCA] subjected to a constrained minimum propeller efficiency η_p = 78.5%.

	$XPROP$	Opt_{4CP}
$T_C(-)$	0.15	0.15
$\beta(deg)$	43.406	43.192
J (-)	1.3698	1.3614
$\eta_p(-)$	0.785	0.785
$TSSP_{mean}(dB)$	-75.05	-75.53

The optimized design for this multi-objective approach shows a less pronounced application of the mid-chord alignment compared to the design for pure aeroacoustic performance(case 1). The trend for both designs is similar: from root to tip there is a gradual increase of forward sweep, after which an abrupt backward sweep is introduced near the tip of the blade. When considering the designs for pure aerodynamic and aeroacoustic performance, it appears the design shown in figure 9.29 is a compromise of the aforementioned designs.

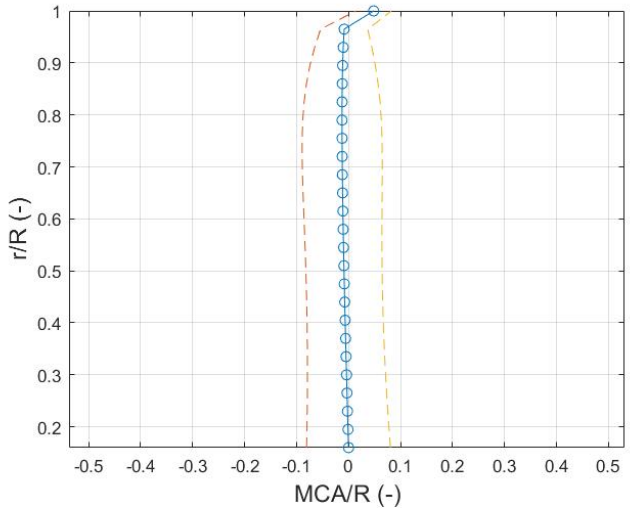

Figure 9.29: Optimized blade mid-chord alignment for high aeroacoustic performance with a propeller efficiency constraint at η_p = 0.785 (4 control points).

For this case the the results yielded similar conclusions to case 1. Therefore, there is no extensive elaboration on these results. However, for this case there is a constraint on the minimum accepted propeller efficiency, which was not active during case 1. As a result, there is a difference in the behaviour of the operational design variables. Due to the application of blade sweep, the thrust coefficient and propeller efficiency decrease. In order to increase the thrust coefficient, the advance ratio is decreased. However, by decreasing the advance ratio the propeller does not operate at an optimum point. Therefore, the pitch angle is decreased as well. This leads to a concurrent decrease of pitch and advance ratio, which is different compared to the behaviour in case 1.

9.2.3. Sensitivity of Blade Sweep Effect

As shown in the previous section, the effect of blade sweep application on the aeroacoustic results was marginal. The maximum difference is 0.5dB between a blade including blade sweep as opposed to a blade without blade sweep, both with optimized operational conditions and a thrust coefficient of 0.15. This is a marginal noise reduction compared to what was found in similar research by others[9, 15]. Since the impact of an application of blade sweep on aeroacoustic performance is a key result of this thesis, an assessment is performed to determine the reason for the marginal impact of blade sweep on noise reduction. In order to determine why there is a marginal impact of blade sweep application on noise reduction, a paper by Hanson[14] is assessed. Hanson described that the phase lag due to blade sweep, which leads to noise reduction, is proportional to the ratio of MCA/chord to the sound wavelength. In addition, Hanson claims that the effect of blade sweep on noise reduction grows as the flight Mach number increases. An increment of the flight Mach number leads to an increment of the operational speed of the propeller, which results in an increment of the blade passage frequency. Since the blade passage frequency is directly coupled to the sound wavelength, a higher flight Mach-number leads to an increase of the ratio MCA to the sound wavelength.

For the results shown in section 9.2.2, the maximum value of the MCA was limited by the bounds of the optimization, while the wavelength of sound is predefined by the freestream Mach number and the advance ratio. In order to assess the effect of the ratio between MCA to sound wavelength on noise emissions, either the wavelength of the sound or the mid-chord alignment can be changed. In order to increase the ratio of MCA-to-λ, the freestream Mach number can be increased. The freestream Mach number affects the impact of blade sweep on noise emissions, since the blade passage frequency and thus the wavelength is dependent on the freestream Mach number for a constant advance ratio. Therefore, the TSSP is calculated for both the optimized swept blade planform and the straight blade as a function of the freestream Mach number. For this calculation, it is assumed that the non-dimensional aerodynamic loading can be kept constant, which ensures only the effect of freestream Mach number is assessed.

Figure 9.30 presents the results of the calculation, which was generated by calculating the noise emissions of both the XPROP and a 6-bladed propeller including the MCA-distribution shown in figure 9.18 for freestream Mach numbers between 0.1 and 0.35. Using higher Mach numbers than 0.35 would yield tip Mach numbers higher than 1. At tip Mach numbers higher than 1, nonlinear effects can become relevant, and loading/thickness noise cannot be assumed as the dominant noise sources and the calculation is no longer reliable. The noise reduction due to sweep at a freestream Mach number of 0.17 is 0.73dB, while the noise reduction at a freestream Mach number of 0.33 is equal to 1.5dB. Thus, this plot generated by the HST-implementation supports the suggestion by Hanson that the effect of the application of blade sweep on noise reduction increases as the freestream Mach number increases. However, by increasing the freestream Mach number in this model, the freestream velocity increases as well, which forces the operational speed to increase for a constant advance ratio. Therefore, the tip Mach number of the propeller increases. Since the noise emissions are also strongly affected by the tip Mach number of the propeller, figure 9.30 only gives an indication that the Mach number affects the impact of blade sweep on noise emissions.

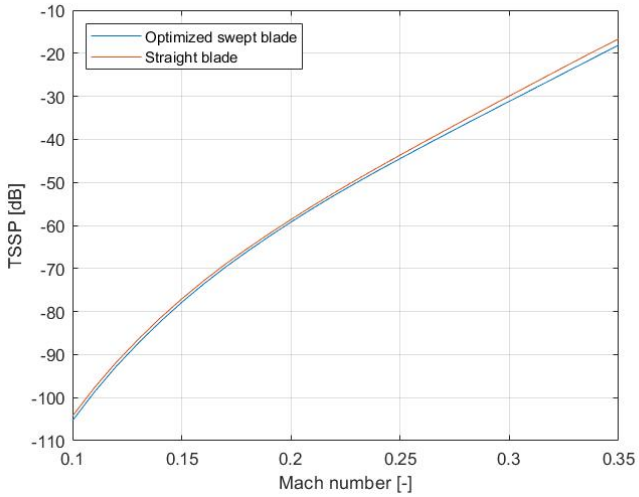

Figure 9.30: Effect of freestream Mach number on noise emissions for the XPROP and the optimized propeller (shown in figure 9.18).

Another measure which can be taken to increase the impact of blade sweep on noise reduction is to use a higher amount of blades, since the blade passage frequency increases, which decreases the wavelength of sound λ. However, increasing the number of propeller blades in this model cannot be used to prove this point, since an increase of propeller blades also leads to an increase in loading. In order to maintain a fixed thrust coefficient, the operational speed should be decreased, which means the tip Mach number decreases. Therefore, it is not possible to assess the effect of blade count on noise emissions in this model, without changing other non-dimensional scaling parameters.

Nonetheless, there is a measure which can be used to prove that the ratio of MCA to sound wavelength leads to a noise reduction by using the optimization model. If the bounds on the design variables in the optimization are increased and the optimization shows a larger blade sweep leading to a larger noise reduction, this proves that the increment of the ratio of MCA to wavelength leads to noise reduction. In this way, no other dimensional or non-dimensional variable changes as a response to an increase in bounds. The optimized planform found in case 1 of section 9.2.2 is used as a baseline for the comparison suggested here. The optimizations are performed for low noise emissions, without the use of a constraint for minimum accepted propeller efficiency. The bound on the MCA-distribution is defined such that the maximum MCA is equal to twice the maximum blade chord length. The resulting blade planform is shown in figure 9.31 and the results are tabulated in table 9.8, both for case 1 of section 9.2.2 and the design shown in figure 9.31.

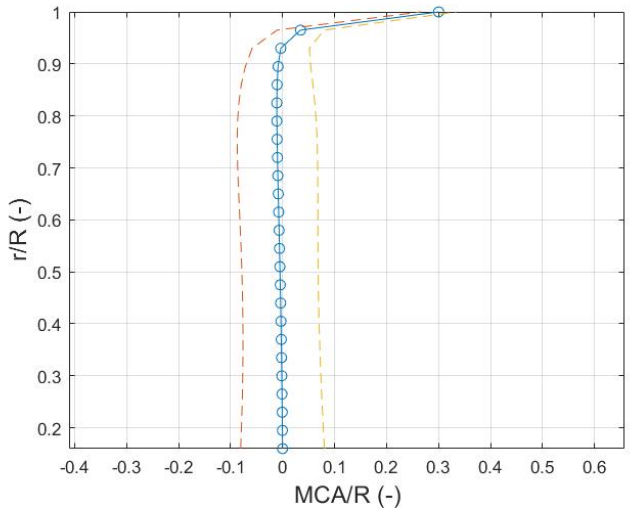

Figure 9.31: Optimized mid-chord alignment distribution including blade planform for maximum aeroacoustic performance, using increased bounds of $MCA_{max} = 2 \times c_{max}$

Table 9.8: Optimization results for design vectors including blade sweep for different bounds on the MCA-distribution.

	$MCA_{max} = c_{max}$	$MCA_{max} = 2 \times c_{max}$
$T_C(-)$	0.15	0.15
$\beta(deg)$	51.61	51.63
J (-)	1.483	1.484
$\eta_p(-)$	0.739	0.738
$TSSP_{mean}(dB)$	-78.76	-78.89

The results in table 9.8 show that an increment of the bounds indeed leads to a noise reduction. However, as discussed in subsection 9.2.2, this noise reduction can also be obtained due to the inboard shift of blade loading and thereby reducing loading noise. Therefore, in order to solely consider the effect of phase cancellation, only the thickness noise is considered. Thus, if a larger MCA-to-λ ratio decreases thickness noise, this is a proof that the increment of this ratio leads to a noise reduction. The wavelength of the sound associated with this optimization setup is calculated using the first blade passage frequency. For an advance ratio of 1.48 and a freestream velocity of 60m/s, the resulting operational speed of the propeller is used to calculate the blade passage frequency for 6 blades, which is 596Hz. The wavelength can be calculated using the speed of sound,

leading to a wavelength of 0.58. The resulting MCA-to-λ ratio is 0.0570. For the optimization including increased bounds, the corresponding MCA-to-λ ratio is 0.1140. The contribution of thickness noise to the overall noise level as determined by the optimization including the baseline bounds ($MCA_{max} = c_{max}$) is equal to -98.35dB. On the contrary, the contribution of thickness noise to the overall noise level as determined by the optimization including increased bounds ($MCA_{max} = 2 \times c_{max}$) is equal to -98.54dB. As a result, the increment of this ratio leads to a noise reduction.

These findings stress the impact of freestream Mach number on the effectiveness of the phase cancellation effect due to blade sweep application. For a higher freestream Mach number, the dominance of the loading noise reduces, which decreases the effect of a shift in blade loading on noise reduction. Therefore, the dependency of noise reduction on the phase cancellation effect due to blade sweep increases. Furthermore, a higher freestream Mach number leads to a reduction of the sound wavelength, since the advance ratio is constant, which means the operational speed and tip Mach number increase. Subsequently, this increases the MCA-to-λ, which enhances the effect of phase cancellation due to blade sweep.

For the initial climb phase, the freestream Mach number is generally below 0.2. At this value, the effectiveness of blade sweep application can be enhanced by operating at a large operational speed, since the wavelength of sound decreases, which increases the MCA-to-λ ratio. However, for an increase of the operational speed, an undesirable effect occurs: the tip Mach number increases which increases noise in general. Therefore, according to this analogy, the effect of blade sweep application to reduce noise remains small considering the initial climb phase. However, within the optimization space, other variables such as the blade number, chord and twist are ignored in this study, which can also be used to enhance the effect of blade sweep application to reduce thrust specific noise.

IV

Conclusions & Recommendations

10

Conclusions and Recommendations

Based on the findings in this thesis, the research questions are answered and the main conclusions are drawn. In this chapter, the conclusions and recommendations for future studies are documented (section 10.1 and section 10.2 respectively).

10.1. Conclusions

The objective of this thesis was to quantify the impact of blade sweep on the trade-off for aerodynamic and aeroacoustic performance of an isolated propeller by means of an optimization study. This optimization study was successfully performed, which allows answering the main research questions.

1. *Which fast and accurate aerodynamic and aeroacoustic performance models for an isolated propeller derived from literature are suitable to be applied in an optimization framework?*

The Blade Element Momentum model with a dependence to blade sweep was used in the optimization study to predict the aerodynamic performance of a propeller. This is a low-order numerical model, which allows for a fast simulation. In the verification and validation process, an assessment was made of two different approaches regarding the treatment of blade sweep in BEM-models: a direct correction of the lift and drag coefficients (Hu-method) and a correction of the induced and azimuthal velocities (Gur and Rosen-method). In this thesis, the optimization study is performed at a relatively low thrust coefficient, which is calculated by using data of a reference aircraft in the climb phase. For this low thrust coefficient, it appears that the correction of the azimuthal velocity due to blade sweep in the Gur and Rosen model induces an error compared to experimental data. Specifically, a comparison to this data reveals that the point of zero thrust was falsely predicted at a lower advance ratio. On the contrary, the Hu-model shows close agreement to the experimental data at low thrust coefficient due to the small correction of lift and drag coefficient for blade sweep, as there is little blade loading. Therefore, for this study the BEM-model implementation including a correction for lift and drag coefficient is selected. Hanson's Helicoidal Surface Theory was used in the optimization study to predict the aeroacoustic performance of the propeller. This model is selected due to the accurate results and a dependence to blade sweep. Since extensive validation has been performed in previous studies by Kotwicz et al.[40], validation is not performed in this thesis. However, based on a proper verification process, accurate aeroacoustic results are generated.

2. *Which suitable optimization method should be selected such that an adequate optimization is performed?*

A gradient-based optimization approach is used in the optimization study, which enables fast convergence of the optimization problem. For gradient-based methods, there is a risk to find local optima. Therefore, in this study the optimizations were performed using different initial design vectors.

3. *How to quantify the trade-off between aerodynamic and aeroacoustic performance for an isolated propeller only considering pitch and advance ratio as design variables?*

Optimization results are generated for a thrust coefficient $T_C = T/\rho_\infty V_\infty^2 D_p^2$ of 0.15, a freestream velocity of 60 m/s and a corresponding freestream Mach number of 0.17. For the quantification of the trade-off between

aerodynamic and aeroacoustic performance considering advance ratio and pitch, various optimizations are performed minimizing the thrust specific noise subjected to an increasing minimum allowed propeller efficiency constraint. For a design vector containing advance ratio and pitch, high aeroacoustic performance is obtained by operating at high pitch and high advance ratio, since the resulting low rotational speed provides low Mach numbers at the blade sections, leading to reduced noise emissions. On the contrary, high aerodynamic performance is obtained by operating at a lower advance ratio and pitch, to obtain an optimum overall thrust-to-torque ratio. The difference in results between optimizing for pure aerodynamic and pure aeroacoustic performance is 10.8dB in propeller noise and 5% in propeller efficiency.

An error-type function fit through the optimization results enables additional quantification of these results. At the design point of maximum propeller efficiency, a noise reduction of 5.7dB can be obtained for a penalty in propeller efficiency of 1%. For a penalty in propeller efficiency of 2%, a noise reduction of 8.1dB can be obtained. The gradient of the error-type function fit shows an increasing behaviour as a function of the minimum accepted propeller efficiency. For the design point for minimum noise, there is a gradient of 0.31dB in noise emissions for each percent in propeller efficiency. At the point for maximum propeller efficiency, there is a gradient of 9.4dB in noise emissions for each percent in propeller efficiency. This leads to the conclusion that a larger penalty in terms of propeller efficiency causes a larger noise reduction, whereas the sensitivity of noise reduction decreases as the maximum allowed propeller efficiency penalty increases.

4. *What is the influence of blade sweep, pitch angle and advance ratio on aerodynamic and aeroacoustic characteristics of a propeller in isolated conditions?*

By incorporating blade sweep into the design vector, the effect of blade sweep on aerodynamic and aeroacoustic performance is quantified. Three cases are investigated: pure aeroacoustic (i), pure aerodynamic (ii), and a multi-objective (iii) performance optimization case. For pure aeroacoustic performance optimization (i), the resulting blade shape features a gradual increase of forward sweep moving from root to tip, until a large backward sweep is introduced near the tip. This design leads to a noise reduction of 0.4dB with respect to the baseline design optimized for advance ratio and pitch. For pure aerodynamic performance optimization (ii) the application of blade sweep does not increase propeller efficiency when considering the XPROP as a baseline propeller. For the multi-objective approach (iii), a minimum acceptable propeller efficiency of 78.5% is used. The resulting blade design proves that the application of blade sweep is less pronounced as compared to the design for pure aeroacoustic performance due to the constraint of minimum propeller efficiency. A 0.5dB noise reduction could be obtained for an optimized design compared to a straight-bladed design.

The previously mentioned impact of blade sweep application on aeroacoustic performance is relatively small (0.5dB), which is contradictory to comparable research by Geng et al.[15] and Pagano et al.[9], as they showed noise reductions of 2.9dB and 1.5dB respectively when blade sweep was incorporated. Therefore, a study of the sensitivity of noise reduction to the effect of blade sweep is performed. The analysis shows that the main mechanism of reducing noise by applying blade sweep is a shift of blade loading to smaller radii, since loading noise is dominant at low freestream Mach number. The shift of blade loading occurs because of the loss of thrust due to the application of sweep near the tip, which is compensated by an increment of advance ratio and pitch. This means noise reduction is only partly caused by the effect of phase cancellation due to blade sweep. According to Hanson[14], the phase lag due to blade sweep is proportional to the ratio between MCA and sound wavelength (MCA-to-λ). The effect of a change of this ratio on thickness noise was assessed to avoid the effect of a shift in radial blade loading. The MCA-toλ ratio is indeed proportional to the phase lag due to blade sweep, since a larger application of blade sweep led to an increase of the MCA-toλ ratio from 0.0570 to 0.1140, which caused a reduction in thickness noise of 0.2dB.

The freestream Mach number has a distinct impact on the effectiveness of phase cancellation due to blade sweep application. For a high freestream Mach number, noise reduction due to blade sweep is solely dependent on the MCA-to-λ ratio and not on a shift in radial blade loading, because the thickness noise is dominant. Furthermore, a high freestream Mach number leads to a reduction of the sound wavelength, leading to an increase of the MCA-to-λ ratio. However, for the initial climb phase, the freestream Mach number is generally below 0.2. At this value, the effect of blade sweep application to reduce noise remains small. It should be stressed that within the optimization space, other variables such as the blade number, chord and twist are ignored in this study, which can also be used in future studies to enhance the sensitivity of blade sweep application to reduce thrust specific noise.

To conclude this thesis, a wider perspective of this work should be emphasised. As shown by this thesis, the operational variables pitch and advance ratio are the defining design variables for the amount of noise emissions and propeller efficiency. For reaching desired noise and propeller efficiency objectives during the initial climb phase, these variables are the most important to meet the objectives. In this thesis, the climbing phase of flight was considered, which is usually a minor fraction of the total mission. By only optimizing advance ratio and pitch, noise emissions around airports can be reduced with approximately 11dB, while there is sacrifice of approximately 5% in propeller efficiency for a limited amount of time. This sacrifice in propeller efficiency is negligible compared to the overall propeller efficiency during the mission.

10.2. Recommendations

Based on the work and discussion presented in this thesis, a number of recommendations are made:

- The use of the BEM-model with sweep-dependency as an aerodynamic performance model is an accurate model when considering low blade sweep angles an a low blade solidity. As shown by the BEM-verification, the accuracy of the model decreases for highly swept blades with a higher blade solidity. Therefore, for highly swept blades it is recommended to use higher-order models, such as panel methods. These methods allow radial dependence between blade elements, which is required in case of the displacement of the bound vortex line of a highly swept propeller blade.
- As the optimization results shown in this study are purely for isolated propellers, installation effects on propeller performance are not considered. However, for a more accurate representation of the aerodynamic and aeroacoustic performance of propellers installed to an aircraft, these effects have to be taken into account for future studies.
- For this study, the effect of blade sweep on aerodynamic and aeroacoustic performance for isolated propellers is treated. However, other design variables such as the twist and chord distributions and blade number can also provide noise reduction. An assessment of optimization for twist and chord distributions optimization could provide valuable insight in the reduction of propeller noise through blade design.
- In this thesis there was no possibility to validate the aeroacoustic model, since no validation data was available. Although validation of the HST-model was performed in previous studies, it is still recommended to test an isolated propeller in a wind-tunnel with limited possibility of acoustic wall reflections to perform an extra validation step and build further confidence in this model.
- The bounds on the blade sweep design variables for this thesis were estimated based on reference studies, such that a feasible structural design could be obtained. However, these bounds were based on estimations. For future studies, a structural model should be used which acts as a constraint for the optimization. Additionally, aeroelastic effects which can induce significant blade deflections should be incorporated in the optimization study as well, to ensure that the optimization generates a feasible design.

References

[1] R. Peterson. "Regional Turboprop resurgence continues; Jet demand shifts upward". In: *Aircraft Engineering and Aerospace Technology* 80.2 (Jan. 2008). ISSN: 0002-2667. DOI: 10.1108/aeat.2008.12780baf.008.

[2] L.L.M. Veldhuis. "Propeller wing aerodynamic interference". PhD thesis. Delft University of Technology, Delft, The Netherlands, 2005. ISBN: 9090195378.

[3] A. Sakharkar. *Pipstrel Velis Electro, the world's first EASA Type certified electric aircraft*. Aug. 2020. URL: https://www.inceptivemind.com/pipistrel-velis-electro-world-first-easa-type-certified-electric-aircraft/13805/.

[4] H. Swift. "A Review of the Literature Related to Potential Health Effects of Aircraft Noise". In: *Partnership for AiR Transportation* (2010).

[5] E.A.M. Franssen, C.M.A.G. van Wiechen, N.J.D. Nagelkerke, and E. Lebret. "Aircraft noise around a large international airport and its impact on general health and medication use". In: *Occupational and Environmental Medicine* 61.5 (May 2004), pp. 405–413. DOI: 10.1136/oem.2002.005488. URL: http://oem.bmj.com/content/61/5/405.abstract.

[6] Tangopaso. *A400M Propeller*. 2009. URL: https://commons.wikimedia.org/wiki/File:A400M_Propeller_(Hamilton-Sundstrand).jpg#filehistory.

[7] B.G. Marinus. "Multidisciplinary Optimization of Aircraft Propeller Blades". PhD thesis. University Lyon, 2011.

[8] O. Gur and A. Rosen. "Multidisciplinary Design Optimization of a quiet propeller". In: *14th AIAA/CEAS Aeroacoustics Conference (29th AIAA Aeroacoustics Conference)* May 2008 (2008). DOI: 10.2514/6.2008-3073.

[9] A. Pagano, L. Federico, M. Barbarino, F. Guida, and M. Aversano. "Multi-objective aeroacoustic optimization of an aircraft propeller". In: *12th AIAA/ISSMO Multidisciplinary Analysis and Optimization Conference, MAO* September (2008), pp. 1–15. DOI: 10.2514/6.2008-6059.

[10] W. de Haan. *Aerodynamic and Aeroacoustic Performance Optimization for a Propeller subjected to Nonuniform Inflow - Literature Study*. Tech. rep. Delft: Delft University of Technology, 2020.

[11] Q.R. Wald. "The aerodynamics of propellers". In: *Progress in Aerospace Sciences* 42.2 (2006), pp. 85–128.

[12] T. Sinnige. "Aerodynamic and Aeroacoustic Interaction Effects for Tip-Mounted Propellers". PhD thesis. Delft University of Technology, 2018. ISBN: 978-94-9301-446-6. DOI: 10.4233/uuid:214e1e9a-c53e-47c7-a12c-b1eb3ec8293b.

[13] B. Magliozzi. "Noise characteristics of model counter-rotating Prop-Fans". In: *AIAA 11th Aeroacoustic Conference*. 1987. DOI: 10.2514/6.1987-2656.

[14] D.B. Hanson. "The influence of propeller design parameters on far field harmonic noise in forward flight". In: *American Institute of Aeronautics and Astronautics (AIAA)* (1979). DOI: 10.2514/6.1979-609.

[15] X. Geng, T. Hu, P. Liu, T. Sinnige, and G. Eitelberg. "Analysis of Thrust-Scaled Acoustic Emissions of Aircraft Propellers and their Dependence on Propulsive Efficiency". In: *ICAS*. 2021.

[16] J.G. Leishman. *Principles of Helicopter Aerodynamics*. Cambridge Aerospace Series. Cambridge University Press, 2002. ISBN: 9780521523967.

[17] M. Bronz, J.M. Moschetta, and G. Hattenberger. "Multi-Point Optimisation of a Propulsion Set as Applied to a Multi-Tasking MAV". In: *International Micro Aerial Vehicle Conference and Competition*. July. 2012.

[18] A.B. Parry, M. Kingan, and B. J. Tester. "Relative importance of open rotor tone and broadband noise sources". In: *17th AIAA/CEAS Aeroacoustics Conference 2011 (32nd AIAA Aeroacoustics Conference)* June (2011), pp. 5–8. DOI: 10.2514/6.2011-2763.

[19] B. Magliozzi, D.B. Hanson, and R.K.K Amiet. "Propeller and propfan noise". In: *Aeroacoustics of Flight Vehicles: Theory and Practice. Volume 1: Noise Sources* 1 (1991), pp. 1–64.

[20] S. Burger. *Multi-fidelity Aerodynamic and Aeroacoustic Sensitivity Study of Isolated Propellers*. Tech. rep. Delft University of Technology, 2020.

[21] C.A. Negulescu. "Airbus AI-PX7 CROR Design Features and Aerodynamics". In: *SAE International Journal of Aerospace* 6.2 (2013), pp. 626–642. ISSN: 19463855. DOI: 10.4271/2013-01-2245.

[22] A.M. Stoll. "Design of Quiet UAV Propellers". PhD thesis. Stanford University, 2012.

[23] C.N. Adkins and R.H. Liebeckt. "Design of optimum propellers". In: *Journal of Propulsion and Power* 10.5 (1994), pp. 676–682. ISSN: 07484658. DOI: 10.2514/3.23779.

[24] C.J. Miller and J.P. Sullivan. "Noise Constraints Effecting Optimal Propeller Designs". In: *NASA Technical Memorandum* 86967 (1985).

[25] F.B. Metzger. "A Review of Propeller Noise Prediction Methodology 1919-1994". In: *NASA Contractor Report* (1995).

[26] D. Ingraham, J. Gray, and L.V. Lopes. "Gradient-based propeller optimization with acoustic constraints". In: *AIAA Scitech 2019 Forum* January (2019), pp. 1–12. DOI: 10.2514/6.2019-1219.

[27] D.B. Hanson. "Helicoidal Surface Theory for Harmonic Noise of Propellers in the Far Field". In: *AIAA Journal* 18.10 (1980).

[28] D. Salomon. *Curves and Surfaces for Computer Graphics*. Vol. 1. 1. Springer, 2006. ISBN: 9783642253874.

[29] A. Rosen and O. Gur. "Novel approach to axisymmetric actuator disk modeling". In: *AIAA Journal* 46.11 (2008), pp. 2914–2925. ISSN: 00011452. DOI: 10.2514/1.37383.

[30] O. Gur and A. Rosen. "Comparison between Blade-Element models of propellers". In: *Technion Israel Institute of Technology - 48th Israel Annual Conference on Aerospace Sciences 2008* 3.3277 (2008), pp. 1139–1169.

[31] E. Branlard, M. Gaunaa, and K. Dixon. "An improved tip-loss correction based on vortex code results". In: *EWEA Conference 2012 - The European Wind Energy Association*. 2012.

[32] W.J.M. Rankine. "On the mechanical principles of the action of propellers". In: *6th session of the Institution of Naval Architects*. 9. 1865, pp. 13–19.

[33] X. Liu and W. He. "Performance Calculation and Design of Stratospheric Propeller". In: *IEEE Access* 5 (2017), pp. 14358–14368. ISSN: 21693536. DOI: 10.1109/ACCESS.2017.2725303.

[34] R.P.J.O.M van Rooij. *Modification of the boundary layer calculation in RFOIL for an improved stall prediction*. Tech. rep. TU Delft IW-96087R, 1996.

[35] E. Obert. *Aerodynamic Design of Transport Aircraft*. Delft: Delft University of Technology, 2006, pp. 168–171. ISBN: 9781586039707.

[36] T. Sinnige, T.C.A. Stokkermans, D. Ragni, G. Eitelberg, and L.L.M. Veldhuis. "Aerodynamic and aeroacoustic performance of a propeller propulsion system with swirl-recovery vanes". In: *Journal of Propulsion and Power* 34.6 (2018), pp. 1376–1390. ISSN: 15333876. DOI: 10.2514/1.B36877.

[37] J.E. Ffrowcs Williams and D.L. Hawkings. "Sound generation by turbulence and surfaces in arbitrary motion". In: *Philosophical transactions of the royal society of London* 264.1151 (1969), pp. 321–342.

[38] F. Farassat. "Theory of noise generation from moving bodies with an application to helicopter rotors". In: *Nasa Technical report* (1975).

[39] F. Farassat, Mark H. Dunn, Ana F. Tinetti, and Douglas M. Nark. "Open rotor noise prediction methods at NASA Langley- A technology review". In: *15th AIAA/CEAS Aeroacoustics Conference (30th AIAA Aeroacoustics Conference)* May (2009), pp. 11–13. DOI: 10.2514/6.2009-3133.

[40] M.T. Kotwicz Herniczek, D. Feszty, S.A. Meslioui, J. Park, and F. Nitzsche. "Evaluation of acoustic frequency methods for the prediction of propeller noise". In: *AIAA Journal* 57.6 (2019), pp. 2465–2478. ISSN: 00011452. DOI: 10.2514/1.J056658.

[41] L. Gutin. "On the sound field of a rotating propeller". In: *National Advisory Committee for Aeronautics* 1195 (1936).

[42] A.F. Deming. "Noise from propellers with symmetrical sections at zero blade angle". In: *National Advisory Committee for Aeronautics* 605 (1937).

[43] F.W. Barry and B. Magliozzi. *Noise Detectability Prediction Method for Low Tip Speed Propellers*. Tech. rep. Airforce Aero Propulsion Laboratory, 1971.

[44] *Propeller models*. Delft, June 2021. URL: https://www.tudelft.nl/lr/organisatie/afdelingen/aerodynamics-wind-energy-flight-performance-and-propulsion/flight-performance-and-propulsion/flight-performance/propeller-aerodynamics/facilities/propeller-models.

[45] *Constrained Nonlinear Optimization Algorithms*. 2021. URL: https://www.mathworks.com/help/optim/ug/constrained-nonlinear-optimization-algorithms.html.

[46] J. Nocedal and S.J. Wright. *Numerical Optimization*. 2006. ISBN: 9780387303031. DOI: 10.1007/0-387-33477-7.

[47] Q Li, K Öztürk, T Sinnige, D Ragni, Y Wang, G Eitelberg, and L.L.M. Veldhuis. "Design and Experimental Validation of Swirl Recovery Vanes for Propeller Propulsion Systems". In: *35th AIAA Applied Aerodynamics*. 2017. ISBN: 9781624105012. DOI: 10.2514/6.2017-3571.

[48] T. Sinnige, D. Ragni, A.M.N. Malgoezar, G. Eitelberg, and L.L.M. Veldhuis. "APIAN-INF: an aerodynamic and aeroacoustic investigation of pylon-interaction effects for pusher propellers". In: *CEAS Aeronautical Journal* 9.2 (2018), pp. 291–306. ISSN: 18695590. DOI: 10.1007/s13272-017-0247-2.

[49] J.E. Marte and D.W. Kurtz. "A Review of Aerodynamic Noise From Propellers, Rotors, and Lift Fans". In: *Technical report, NASA* (1970).

[50] *ATR42-500*. URL: https://modernairliners.com/atr72andatr42.

[51] A. Parry and D. Crighton. *Theoretical prediction of single rotation propeller noise*. Tech. rep. University of Leeds, 1988. DOI: 10.2514/6.1986-1891.

[52] M. Dimchev. *Experimental and numerical study on wingtip mounted propellers for low aspect ratio UAV design*. Tech. rep. Delft University of Technology, 2012.

[53] N. Van Arnhem, R. de Vries, T. Sinnige, R. Vos, G. Eitelberg, and L.L.M. Veldhuis. "Engineering Method to Estimate the Blade Loading of Propellers in Nonuniform Flow". In: *AIAA Journal* (2020), pp. 1–15. DOI: 10.2514/1.J059485.

V

Appendices

A

Blade Cross-sectional Shapes

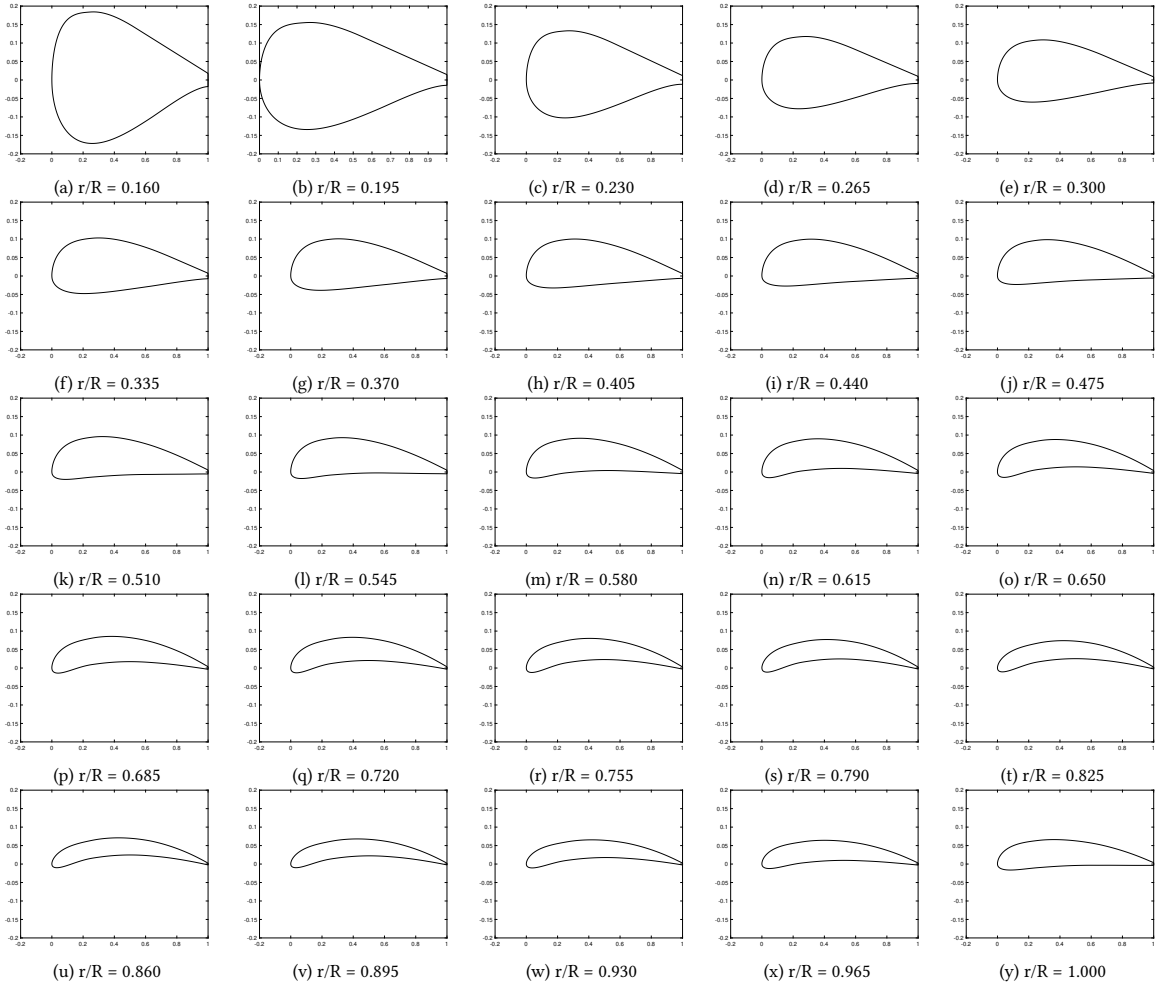

(a) r/R = 0.160 (b) r/R = 0.195 (c) r/R = 0.230 (d) r/R = 0.265 (e) r/R = 0.300

(f) r/R = 0.335 (g) r/R = 0.370 (h) r/R = 0.405 (i) r/R = 0.440 (j) r/R = 0.475

(k) r/R = 0.510 (l) r/R = 0.545 (m) r/R = 0.580 (n) r/R = 0.615 (o) r/R = 0.650

(p) r/R = 0.685 (q) r/R = 0.720 (r) r/R = 0.755 (s) r/R = 0.790 (t) r/R = 0.825

(u) r/R = 0.860 (v) r/R = 0.895 (w) r/R = 0.930 (x) r/R = 0.965 (y) r/R = 1.000

Figure A.1: Blade cross section shapes at the 25 radial positions of the XPROP-propeller(untwisted)

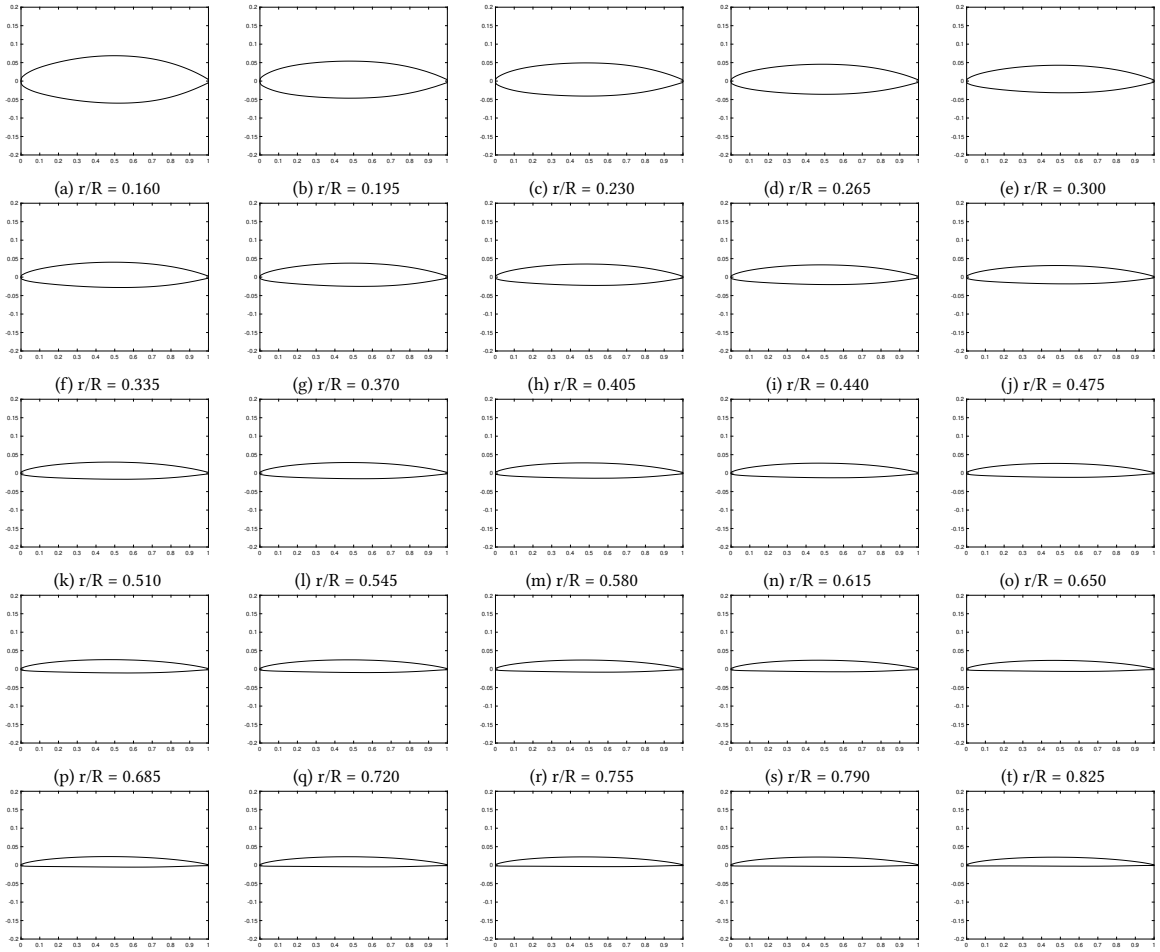

(a) r/R = 0.160 (b) r/R = 0.195 (c) r/R = 0.230 (d) r/R = 0.265 (e) r/R = 0.300

(f) r/R = 0.335 (g) r/R = 0.370 (h) r/R = 0.405 (i) r/R = 0.440 (j) r/R = 0.475

(k) r/R = 0.510 (l) r/R = 0.545 (m) r/R = 0.580 (n) r/R = 0.615 (o) r/R = 0.650

(p) r/R = 0.685 (q) r/R = 0.720 (r) r/R = 0.755 (s) r/R = 0.790 (t) r/R = 0.825

(u) r/R = 0.860 (v) r/R = 0.895 (w) r/R = 0.930 (x) r/R = 0.965 (y) r/R = 1.000

Figure A.2: Blade cross section shapes at 25 radial positions of the APIAN-propeller(untwisted)

B

Experimental Setup

In this appendix the experimental work which has been performed is discussed. The experimental results did not contribute to the thesis itself. Therefore, the setup is included in the appendix as a reference. Both configurations for an isolated propeller and a propeller subjected to non-uniform inflow are discussed. A feasible configuration was selected such that effect of a specific type of non-uniform inflow on propeller aerodynamic and aeroacoustic performance could be measured. Firstly, section B.1 gives an outline of the wind-tunnel facility. Secondly, section B.2 provides an overview of the used test setup. Subsequently, in section B.3 the propeller and wing used during the test are discussed, followed by a discussion of the measurement techniques in section B.4. Finally, the selected test conditions are discussed in section B.5.

B.1. Wind-Tunnel Facility

The wind-tunnel facility which was used is the Low-Turbulence Tunnel (LTT) at the Delft University of Technology, shown in figure B.1. This wind-tunnel features a closed-return circuit with a closed-walled test section. The orthogonally shaped wind-tunnel test section is 1.80 m wide, 1.20 m tall and 2.60 m in length. In the test section itself the wind-tunnel is capable of generating speeds of up to 120 m/s. Generally, tests are performed at speeds between 30 and 100 m/s. As a result of a large contraction ratio of 17.8, a low freestream turbulence level of less than 0.1% can be guaranteed at these speeds[12]. Additionally, the test section is slightly divergent to account for boundary layer growth at the wall.

However, for acoustic measurements the wind-tunnel is not ideal, because the wind-tunnel test section is not acoustically treated. This means reflection of sound waves will occur, which can affect acoustic measurements. Additionally, due to background noise originating from the motor and fan driving the wind-tunnel, measuring a high signal to noise ratio can be a challenge.

B.2. Overview of Test Setup

To analyse the effect of a nonuniform inflow field on propeller aerodynamic and aeroacoustic performance, a test setup including a propeller and a wing upstream of the propeller was used. As such, a pusher propeller configuration was simulated, in which the propeller inflow field was influenced by the wake of an upstream wing. The upstream wing was located at a fixed upstream distance from the propeller plane, which was constrained by the geometry of the test section. The vertical position of the wing was chosen such that the test setup represented a validation case used to validate the engineering method to estimate blade loading of propellers subjected to nonuniform inflow by van Arnhem et al.[53]. The wing was located at z/R = 0.5, ie. the wake of the wing impinged the propeller at the lower half of disk, at half the distance between the propeller axis and the propeller blade tip. This type of nonuniform inflow is characterised by a local, out-of-plane disturbance and a defect in total pressure. Due to time constraints during the test campaign and geometrical constraints of the test section it was not possible to test other cases of nonuniform inflow. In figure B.2, a complete overview of the test section including wing and propeller is shown.

Additionally to the nonuniform inflow case, an isolated propeller was also tested to provide a reference for both the aerodynamic and aeroacoustic measurements. This isolated case was tested prior to installing the wing.

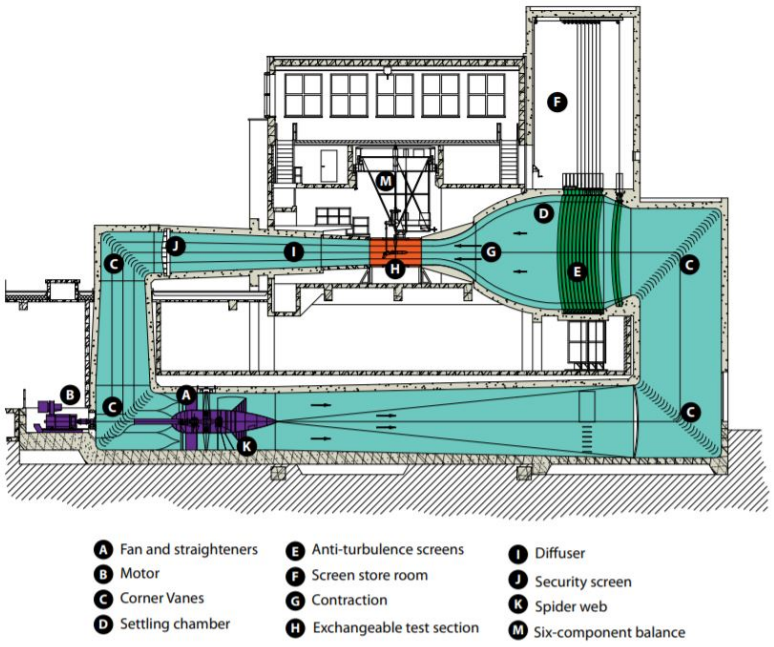

Figure B.1: Low-Turbulence Wind-Tunnel (LTT) facility lay-out[52]

Figure B.2: Front view of the test setup with the wing installed upstream of the propeller in the Low-Turbulence Tunnel at Delft University of Technology

B.3. Models

B.3.1. Propeller

The propeller which was used during the test is the 3-bladed XPROP-propeller, a propeller with a diameter of 0.4064 m. The three blades of the propeller had a pitch angle (angle between the local chord line and the propeller plane) of 30 degrees at 70% of the blade radius. No measures to force transition on the blades were applied during the experiment. A technical drawing of the propeller geometry is provided in figure B.3. Additionally, the radial distribution of chord and pitch are shown in figure 7.2. The blades of this propeller are equal to the baseline propeller blades used in the optimization study, so the shape of blade cross-sections at each radial station along the radius are depicted in appendix A. The propeller was positioned such that the propeller axis coincided with the middle of the test section.

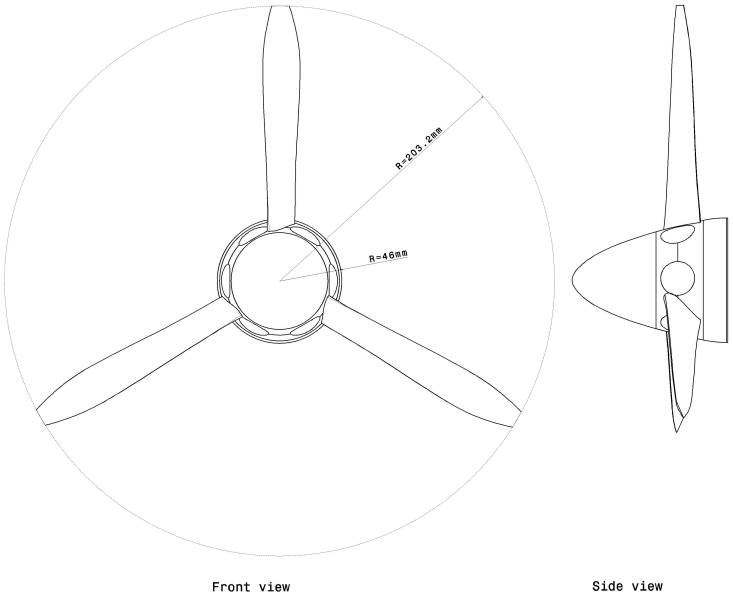

Figure B.3: Technical drawing of the 3-bladed XPROP

The propeller was powered by a 3 kW induction motor housed inside a nacelle with a diameter of 0.092 m. Both for the isolated case and the nonuniform inflow case the propeller was supported by a sting-mounted configuration, as shown in figure B.4. In figure B.5, a blade-off configuration is shown, which was used to determine the performance of the propeller blades. Thereby, the drag component induced by the propeller slipstream on the nacelle is neglected. Additionally, as shown in figure B.5, zigzag strips were attached to the sting to trigger boundary layer transition. The strips delayed boundary layer separation at the sting, which prevented vortex shedding along the sting. As a result, there was a steady loading component along the sting. The sting itself was connected directly to an external balance (discussed in section B.4).

B.3.2. Wing

The setup including wing is shown in figure B.2. The wing which was used during the test had a chord length of 0.107 m and a symmetric NACA airfoil (NACA0018) profile which is constant along the span. There was no taper and no sweep applied to the wing. Laminar boundary layer separation of the wing proved to be a significant noise contributor. Therefore, boundary layer transition was forced by transition strips applied at approximately X/c = 0.3 at the lower and upper side of the wing. Therefore, separation of the boundary layer could be avoided and wing noise emissions were diminished. A consequence of this measure was an increase in width of the wake downstream of the wing.

Figure B.4: Photograph of propeller connected to a sting-mounted setup, representing the isolated propeller case

Figure B.5: Photograph showing blade-off configuration including sting and nacelle. The zigzag strips are shown on the sting.

In streamwise direction, the wing was positioned 0.426 m upstream of the propeller plane. This meant the propeller plane was approximately four wing chord lengths downstream of the wing trailing edge. As discussed in section B.2, the wing was positioned at a vertical distance of z/R = 0.5 with respect to the propeller. This corresponds to a distance of 0.564 m with respect to the bottom wall of the test section. It should be noted that there was a minor vertical bend in the wing, which lead to a height difference of 3 mm between the middle of the wing and the wall of the test section. Additionally, due to bending and twisting of the wing there is a possibility that the wake profile of the wing was influenced by an angle of attack change of ± 0.5 °.

B.4. Measurement Techniques

In table B.1, an overview of the measurement aims and the corresponding measurement techniques is provided. These measurement techniques were used in the test campaign and these will be treated in this section.

Measurement aim	**Measurement technique**
Integrated loading	External balance
Propeller loading	Internal loadcell
Noise emissions	Microphone array's
Inflow-field information	Wake rake

Table B.1: Overview of measurement aim and corresponding measurement techniques used in the experiment

B.4.1. Integrated Loading

During the test campaign an external balance was used to measure the integral forces and moments on the entire model. Tare measurements were taken before and after each measurement set. Both measurements with and without propeller blades were taken, to assess the loading of the propeller blades. For this procedure, a possible upstream effect of the sting and nacelle on the propeller blades was neglected. In order to account for the uncertainty of the balance measurements, repeated measurements were taken at equal operating conditions.

B.4.2. Propeller Loading

For the aerodynamic performance of the propeller including hub, an ATI mini45 titanium-load cell was used. In comparison to the external balance, this measurement technique can be considered as an internal balance. The load cell was located directly in front of the motor, behind the hub of the propeller. Therefore, all the forces measured by the load cell are the result of the propeller blades and the propeller hub. A torque and a thrust force can be measured, which allows for an assessment of the thrust and power coefficient of the propeller. As a result, a propulser efficiency was extracted from the load cell. However, a drawback of the load cell was that there was a dependency on the temperature during the experiment. Since the motor caused a temperature difference during the experiment, some of the data was not reliable.

B.4.3. Noise Emissions

A total of nine high performance low voltage electret condenser microphones were used to measure the acoustic pressure induced during the experiments, of which five of the LinearX M51 type and four of the LinearX M53 type. These microphones were embedded in an array parallel to the propeller axis in the lower wall of the test section, which is 0.625 m from the propeller axis. The microphones installed in a small cavity and the flow in the wind-tunnel test section were divided by means of a Kevlar sheet, since this porous material ensures acoustic transparency, while the flow remains attached to the wall. The M51 and M53 microphones are positioned alternately in the microphone array. These microphones cover a directivity range of $-1.7^\circ < \theta < 28.5^\circ$, not including refraction effects due the shear layer. These microphones were calibrated by means of a GRAS 42AA piston phone at a voltage level of 9 volt.

The microphone array was attached to a turntable in the bottom of the test section to obtain data at a larger range in directivity angles and a larger range in observer distance from the propeller axis, as shown in figure B.6. This turntable was turned 48° in total with a resolution of 6°. A smaller resolution was not possible, due to the rapid increase of motor temperature. Additionally, microphone data was acquired concurrently with the propeller encoder's once-per-revolution trigger to ensure tonal noise data could be extracted.

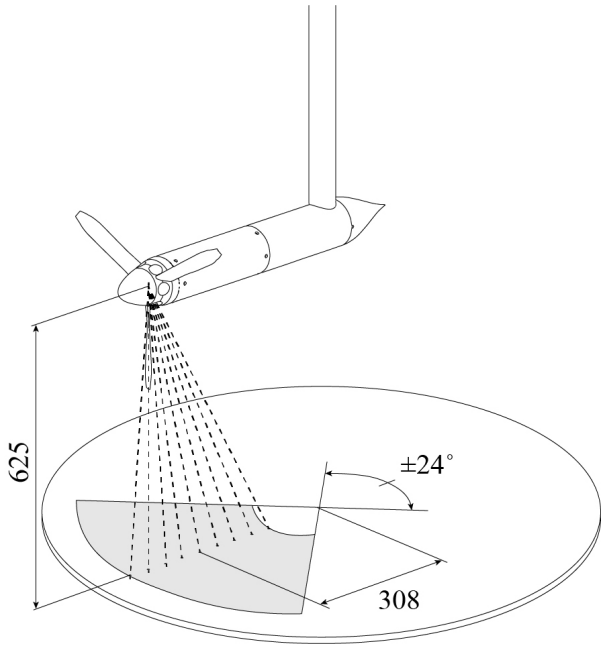

Figure B.6: Microphone locations used for noise measurements

B.4.4. Inflow-Field Information

In order to quantify the non-uniform inflow field of the propeller created by the upstream wing, a traversable wake rake was used. A wake rake was used rather than a single total pressure tube to identify possible irregularities in the wing profile. The wake rake featured a number of 17 total pressure tubes and two static pressure tubes and was aligned in streamwise direction, parallel to the span of the wing. Therefore, the wake rake is traversed vertically for a resulting wake profile. A spacial resolution of 2 mm is used for a total vertical traversed distance of 64 mm, since this captured the entire wake profile of the wing.

Due to geometrical constraints of the test section, the wake rake was installed 21 mm downstream of the propeller plane. The total pressures at all probes were simultaneously recorded by using an electronic pressure scanner. Additionally, a reference total pressure in the freestream of the test section was measured at these timestamps. The wake rake was only installed at the end of the test campaign to prevent an aeroacoustic and aerodynamic effect on other measurements. It was not feasible to perform a prop on measurement of propeller inflow field including wing due to time and geometry constraints.

B.5. Test Conditions

During the entire test campaign the 3-bladed propeller was used to acquire data at a freestream velocity of 30m/s. At this freestream velocity a large propeller operating range could be guaranteed, while also a suitable operational point for noise measurements could be selected in this operation range. A higher freestream velocity was not desirable, since a smaller operating range could be achieved due to a power output constraint by the electric motor. To obtain an insight in aerodynamic performance of the propeller, measurements with the external balance and load cell were taken at advance ratios between J = 0.8 and J = 1.4. At these advance ratios, the range in Reynolds number was 110,000-175,000, based on the effective velocity and the chord at r/R = 0.7. The thrust coefficient T_C, based on freestream velocity, ranged between 0.01 and 0.18. For both the uniform and nonuniform inflow case, tare measurements were taken with the propeller blades removed from the hub, such that the blade-on data could be compared to blade-off data.

For the acoustic measurements, a fixed operational point of J = 0.9 was chosen. This operational point provided a compromise between a high signal-to-noise ratio and the desired operational point considering aerodynamic efficiency. Due to the background noise originating from the wind-tunnel motor and fan, a small advance ratio and thus a higher rotational speed was necessary to obtain a high signal to noise ratio. At this operational point, a tonal noise originating from the propeller could clearly be identified. For the aeroacoustic measurements using the microphones embedded in the turntable and the microphone array embedded in the side of the test-section, experimental data was gathered for both the nonuniform and the uniform inflow case.